國 立 交 通 大 學

光 電 工 程 研 究 所

博 士 論 文

寬能隙材料半導體微共振腔之研究

Study of wide-bandgap semiconductor microcavities

研 究 生: 陳俊榮　　　　　Student:　Jun-Rong Chen

　　　　　　盧廷昌 教授　　　　　　　Prof. Tien-Chang Lu
指導教授:　　　　　　　　　Advisor:
　　　　　　郭浩中 教授　　　　　　　Prof. Hao-Chung Kuo

中 華 民 國 九 十 九 年 八 月

寬能隙材料半導體微共振腔之研究

Study of wide-bandgap semiconductor microcavities

研究生:陳俊榮   Student: Jun-Rong Chen

指導教授:盧廷昌 教授   Advisor: Prof. Tien-Chang Lu

指導教授:郭浩中 教授   Advisor: Prof. Hao-Chung Kuo

國 立 交 通 大 學

光 電 工 程 研 究 所

博 士 論 文

A dissertation

Submitted to Institute of Electro-Optical Engineering

National Chiao Tung University

in Partial Fulfillment of the Requirements

for the Degree of

Doctor of Philosophy

in

Department of Photonics & Electro-Optical Engineering

June 2009

Hsinchu, Taiwan, Republic of China

中 華 民 國 九 十 九 年 八 月

寬能隙材料半導體微共振腔之研究

研究生：陳俊榮　　　　　　　　　　　　指導教授：盧廷昌教授
　　　　　　　　　　　　　　　　　　　指導教授：郭浩中教授

國立交通大學光電工程研究所

摘要

　　由於寬能隙半導體微共振腔在研究光與物質交互作用上十分具有潛力，因此近年來吸引許多研究群的研究與討論。此種半導體微共振腔可用以侷限光子與激子在微小空間中，進而產生一種同時具有光和物質特性的準粒子，一般稱之為共振腔極化子。此種準粒子具有玻色子的特性，包含了極小的有效質量與不需滿足庖立不相容原理的特性。這些特色導致了共振腔極化子可能被用於固態系統中達到室溫下的玻色-愛因斯坦凝聚。共振腔極化子被期望能夠達成一種極低臨界能量的新型態極化子雷射，這是一種不需要達到居量反轉即可產生雷射光的新元件。於此篇論文中，我們主要利用氧化鋅與氮化銦鎵材料製作微共振腔元件，並研究其極化子雷射與電激發極化子發光二極體的特性。

　　我們首先利用氧化鋅微共振腔元件成功在室溫下觀察到極化子雷射的現象，其達到雷射所需的臨界激發能量非常低。此外，我們更進一步觀察共振腔極化子釋放能量與凝聚的過程，在共振腔極化子釋放能量的過程中理論上所預期可能發生的現象，包含共振腔極化子瓶頸效應與玻色子的受激放射現象，這些效應皆在氧化鋅微共振腔的光學實驗中被觀測到。除此之外，我們亦實現了室溫下電激發氮化銦鎵極化子發光二極體，利用兩種不同的實驗技術，包含改變溫度的電激發光量測與改變收光角度的電激發光技術，我們同時觀察到共振腔極化子色散曲線的交錯現象，亦即證明了在室溫電激發的條件下，氮化鎵共振腔發光二極體確實存在光與物質交互作用的強耦合機制。這些研究成果再次證明了寬能隙半導體微共振腔是適合用來製作新一代共振腔極化子發光元件的重要材料。

Study of wide-bandgap semiconductor microcavities

Student: Jun-Rong Chen   Advisor: Prof. Tien-Chang Lu

Advisor: Prof. Hao-Chung Kuo

Department of Photonics & Institute of Electro-Optical Engineering

National Chiao Tung University

Abstract

Wide-bandgap semiconductor microcavities have attracted much attention in the research field of strong light-matter interaction in recent years owing to their potential to enhance and control the interaction between excitons and photons, which leads to cavity polaritons. This half matter-half light quasi-particle is characterized by the nature of Bose particles, including a very small in-plane effective mass and the lack of Pauli exclusion principle, resulting in the possible realization of room-temperature Bose-Einstein condensation in solids. Cavity polariton is expected to open the way for the development of a new generation of thresholdless polariton laser without the requirement of population inversion. In this thesis, we use ZnO-based and InGaN-based hybrid microcavities for the study of polariton lasing and electrically pumped polariton light-emitting diodes.

We demonstrated a room-temperature polariton lasing with an extremely low threshold pumping density from the ZnO microcavity. The polariton relaxation mechanisms including polariton relaxation bottleneck effect and bosonic final state stimulation effect are experimentally demonstrated in this study as well. Furthermore, we present an electrically pumped InGaN-based polariton LED in strong coupling regime. Two different approaches including the temperature-dependent and angle-resolved electroluminescence spectra demonstrate an obvious polariton

characteristic of anticrossing. These research results show that the wide-bandgap semiconductor microcavities are mostly adapted for the realization of a new generation of polariton emitters.
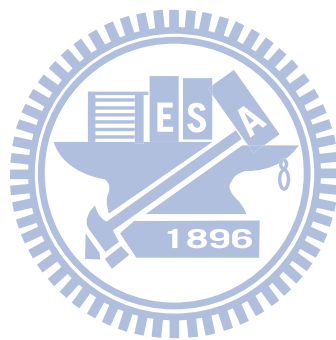
Acknowledgement

你自己囉。

　　最後我要感謝永遠在背後支持我的家人，求學生涯的忙錄卻往往犧牲與你們相聚的時間，你們背後的支持永遠讓我最累的時候可以得到最大的溫暖，謝謝你們。

Content

viii

List of Figures

xi

List of Tables

Chapter 1 introduction

Light-matter interaction is an interesting physical phenomenon and the corresponding mechanisms, such as absorption and emission, are the fundamental and macroscopic interaction between light and matter. Effects originating from light-matter coupling have stimulated the development of optics for the last three centuries and the significant breakthrough in this research field is the successful demonstration of laser. Furthermore, the development of quantum mechanics in the early decades of the twentieth century pushes the investigation of light-matter interaction into the microscopic limit. Nowadays, quantum optics has become an important tool for interpreting modern optical experiments about microscopic light-matter interactions.

Rapid progress of crystal-growth technology creates possibilities for fabrication and design of microstructures that have unusual and extremely interesting optical properties since the successful development of molecular beam epitaxy (MBE) and metal organic chemical vapor deposition (MOCVD). These technologies make it possible for scientists to obtain experimental demonstrations about the prediction of quantum mechanics and quantum optics. In addition, based on the epitaxial techniques the investigation of light-matter interaction serves as building blocks for many semiconductor optoelectronic devices such as light-emitting diodes (LEDs) and semiconductor lasers, which have been widely used in our daily life.

To study the interaction of light and matter, a simple way is to create a high-finesse optical cavity, which can be used to confine photons, and then put atoms in this cavity. The most concrete configuration is a laser system such as conventional solid-state laser and gas laser. Nevertheless, when the cavity configuration is reduced to be close to, or below the dimension of the wavelength of light, it will be generally termed as "microcavity" [1].

1.1 Semiconductor microcavities

Advances in epitaxial growth technology can grow sharp semiconductor heterostructures and create different kinds of optical semiconductor microcavities by using nano-fabrication technology. The resonant optical modes within a cavity have characteristic lineshapes and wavelength spacings. Since the wavelength spacings are nearly inversely proportional to the cavity length, a microcavity can have large wavelength spacings and few quantized cavity modes. A common example of semiconductor microcavity is a vertical-cavity surface-emitting laser (VCSEL) consisting of an active layer embedded between two highly reflective distributed Bragg reflectors (DBRs) [2]. In general, a VCSEL has a cavity length with an integral number of half-wavelengths. Under this circumstance, it is possible for emission spectrum from active layer to couple with only one cavity mode, creating a temperature-insensitive semiconductor laser. Fig. 1.1 shows the difference between conventional edge-emitting lasers and VCSELs.
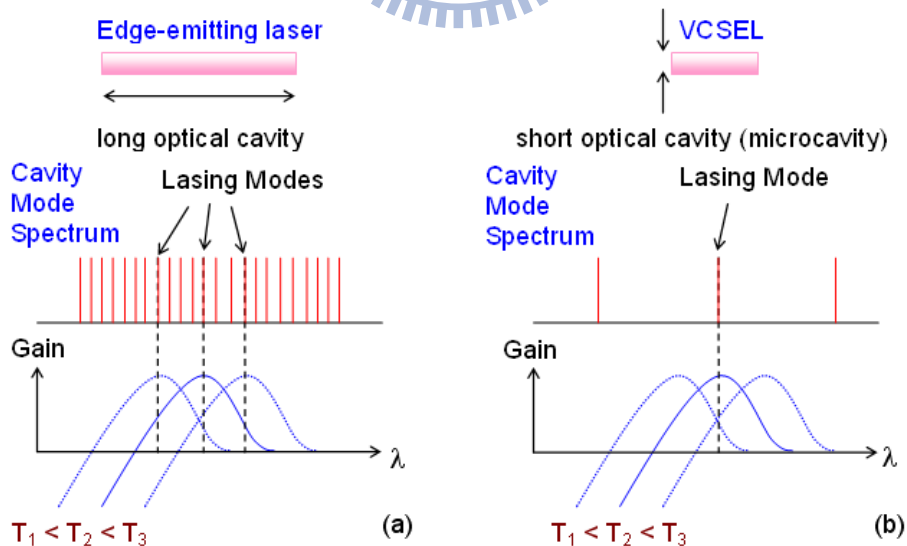
Fig. 1.1 (a) Lasing mode of an edge-emitting laser changes with temperature evidently due to the alignment with the peak of gain spectrum. (b) Lasing mode of a VCSEL does not change with temperature distinctly due to the larger spacing between cavity modes.

A VCSEL-like optical microcavity has an active layer embedded between two highly reflective reflectors. It is a typical Fabry–Perot microcavity. In addition to the method of confining photons using two reflectors, the whispering gallery modes of microspheres or microdisks have a different mechanism to confine photons. Whispering gallery resonators are typically dielectric spherical structures in which waves are confined by continuous total internal reflection [3]. Furthermore, microcavities based on photonic crystals can provide extremely small mode volumes and confine photons by photonic bandgap [4]. These different kinds of optical microcavities exhibit unusual and interesting optical properties and have been widely studied in recent years.

1.1.1 Microcavity quality factor and photon lifetime

An ideal optical microcavity would confine light indefinitely and would have resonant frequencies at precise values. Deviation from this ideal condition is described by the cavity quality factor Q, which could identify the performance of a micorcavity. The definition of cavity quality factor can be expressed as $\lambda/\Delta\lambda$, where λ is the emission wavelength from cavity mode and $\Delta\lambda$ is the linewidth (FWHM) of cavity mode. A simple way to experimentally probe the Q value is to perform the measurement of reflectivity spectrum at normal incidence. A sharp dip could be observed in the reflectivity spectrum if the cavity has precise design and high quality factor. Fig. 1.2 presents different optical microcavities classified by different confinement methods used. The corresponding cavity Q values are shown as well.

Another interpretation of a cavity Q value represents a measure of how many oscillations taking place inside the cavity before the excited photon energy dissipates out of the cavity. It means that the photon energy for narrow linewidth will be trapped in the cavity for longer period of time if we have a high-Q cavity. Based on this definition, we can express the cavity Q factor as

$$Q = \frac{2\pi}{T} \frac{W}{-dW/dt} = \omega_0 \frac{W}{-dW/dt} , \qquad (1.1)$$

where W is the energy stored in the system at resonance, T is the resonance period, and ω_0 is the resonance frequency. Therefore, the energy evolution as function of time can be expressed as

$$W(t) = W(0)e^{-\omega_0 t/Q} . \qquad (1.2)$$

We can also have Q related to the photon lifetime τ_p

$$\tau_p = \frac{Q}{\omega_0} . \qquad (1.3)$$

This means that the exponentially decaying photon number has a lifetime given by τ_p.
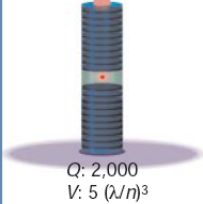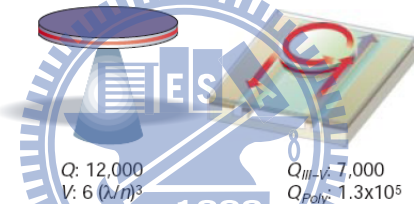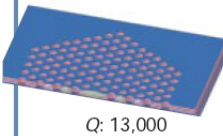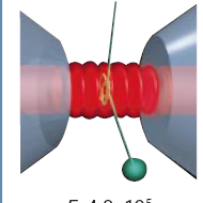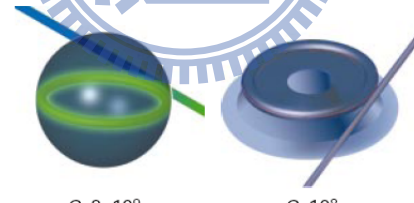
Fig. 1.2 Optical Microcavities are organized by column according to the confinement method used and by row according to high Q and ultrahigh Q. (After [1])

Another important property for embedding an emitter inside a microcavity is the Purcell effect. It indicates that the rate of spontaneous emission can be modified by placing the light source in a resonant cavity [5]. The enhancement is given by the Purcell factor

4

$$F_P = \frac{3}{4\pi^2} \left(\frac{\lambda_C}{n} \right)^3 \frac{Q}{V_{eff}}, \tag{1.4}$$

where n is the refractive index of the cavity, V_{eff} is the effective volume of the cavity mode, and λ_C is the cavity mode emission wavelength. The crucial ration Q/V_{eff} controls the emission rate, dependent on different spectral and spatial overlaps.

1.1.2 Planar microcavities for wide-bandgp materials

In this thesis, we will focus on the investigation of planar semiconductor microcavities due to the easy fabrication and measurements. Nevertheless, for wide-bandgap semiconductor materials, the fabrication of high-quality planar microcavities is very difficult due to the lack of lattice-matched substrate and lattice-matched DBRs. Therefore, the possible design of wide-bandgap semiconductor microcavities can be classified into three major types, as shown in Fig. 1.3. The first one is monolithically grown vertical resonant cavity consisting of epitaxially grown top and bottom DBRs [Fig. 1.3(a)]. The advantage of the fully epitaxial microcavity is the controllable cavity thickness which is beneficial to fabricate microcavity structure. However, a high-Q cavity requires extremely high-reflectivity DBRs. The fully epitaxial wide-bandgap microcavity is very difficult to achieve this requirement due to the difficulty in growth of high-reflectivity nitride-based DBRs, which are usually employed as the reflectors for active layers constructed by wide-bandgap materials.

The second one is vertical resonant cavity consisting of dielectric top and bottom DBRs [Fig. 1.3(b)]. The double dielectric DBR microcavities can exhibit high cavity Q factors because of the high-reflectivity DBR, which are relatively easy to fabricate. The large refractive index contrast in dielectric materials can make high-reflectivity and large-stopband DBR with less number of pairs. The drawback of the double dielectric

DBR microcavities is the difficulty of controlling the cavity thickness precisely and the complicated fabrication process due to the employment of laser lift-off technique [6]. In addition, the thickness of the cavity should keep as thick as possible to avoid the damage of the active layer during the laser lift-off process. Such thick cavity length could increase the cavity mode volume and reduce the microcavity effect.
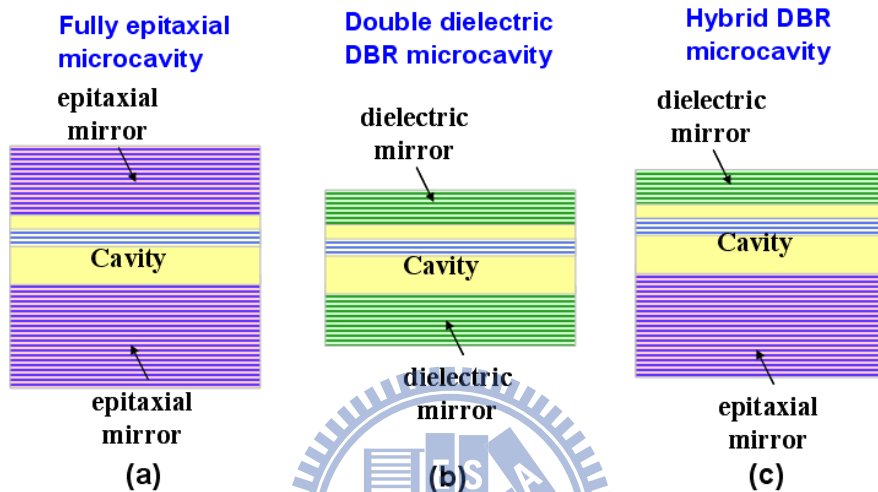
Fig. 1.3 Three typical kinds of wide-bandgap semiconductor microcavity structures. (a) Fully epitaxial microcavities. (b) Double dielectric DBR microcavities. (c) Hybrid DBR microcavities.

The third one is the microcavity structure combining an epitaxially grown DBR and a dielectric type DBR which compromises the advantages and disadvantages of the above two microcavity structures [Fig. 1.3(c)]. The hybrid DBR microcavity can eliminate the complex process and keep the feasibility of coplanar contacts with dielectric DBR mesas for the future electrically pumped microcavity applications. The major requirement for the fabrication of hybrid DBR microcavity for wide-bandgap materials is to grow high-reflectivity and high-quality nitride-based DBRs. The relevant study about the issue of growing nitride DBRs will be discussed in Chapter 3.

1.1.3 Strong and weak coupling regimes

When we consider an excited atom in an ideal mocricavity, which means a microcavity without any optical loss, and the dipole transition frequency is resonant with the cavity mode, the excited atom (dipole) and cavity mode will couple, leading to a quantum of energy shifting back and forth between the atom and the cavity mode. This fundamental dynamic of the atom-field system is reversible as long as the system is isolated and the process of the energy exchange between the atom and cavity mode is called Rabi oscillations. In general, we term this strong light-matter interaction a strong-coupling regime. Nevertheless, in reality the cavity will have a finite photon lifetime (finite cavity Q value) that will prevent the reversible process by allowing the energy to leak irreversibly into the continuum. Specifically, the atomic transition will couple to continuum radiation modes and thereby experience spontaneous decay of its population as well as polarization dephasing. This irreversible process means the system is in a weak-coupling regime. In spite of the reality of energy dissipation, strongly coupled systems can be observed even if the Rabi dynamic can exist only briefly. Strong coupling occurs when the atom-field coupling strength is faster than any underlying dissipative rate. Under conditions of strong coupling, weak optical probing near the microcavity resonant frequency reveals two spectral transmission peaks giving the energies of new eigen states, which are now entangled states of the atom and cavity field. This is one of the experimental techniques to probe the strong coupling regime [7]. The typical optoelectronic devices with microcavity structures operating under weak coupling regime are resonant-cavity light-emitting diodes (RCLEDs) and VCSELs which have been developed for a long time and commercialized in many applications. As for the microcavity devices operating under strong coupling regime, they are an important hot topic in recent years and will be discussed in the following sections.

1.1.4 Semiconductor microcavity polaritons

Considering the situation when we have a semiconductor microcavity structure consisting of an active layer embedded between two high-reflectivity DBRs, this structure will be very similar to the configuration of atom-field interaction, as mentioned in section 1.1.3. Therefore, by exciting the active layer using laser sources or electrical injection, the free electron-hole pairs will be created. Furthermore, a quasi-particle, termed as exciton, is created if an excited electron-hole pair bound by the Coulomb interaction. This exciton has a similar function as the excited atom in a microcavity. When the exciton strongly interacts with the confined optical field of the semiconductor microcavity, it is possible for this system to be in the strong-coupling regime.
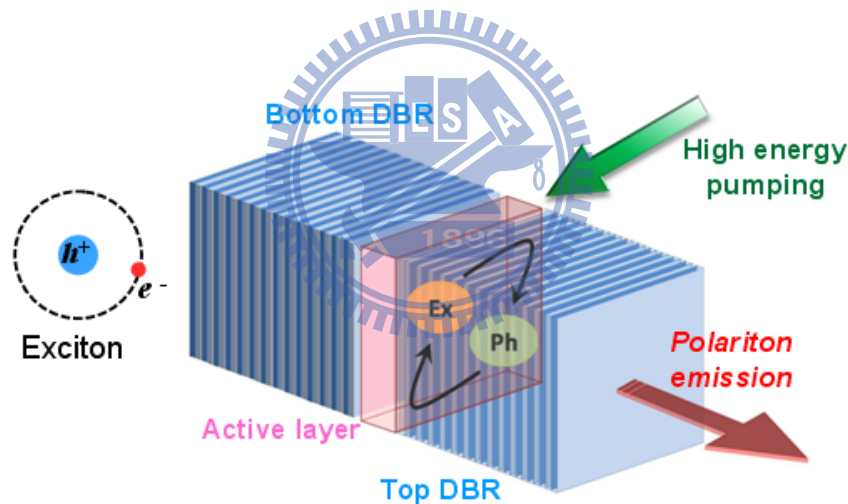
Fig. 1.4 Schematic sketch of the semiconductor microcavity consisting of an active layer embedded between two high-reflectivity DBRs.

Fig. 1.4 shows the schematic sketch of the microcavity configuration. If the rate of energy exchange between the cavity field and the excitons becomes much faster than the decay and decoherence rates of both the cavity photons and the excitons, an excitation in the system is stored in the combined system of photon and exciton. Thus the excitations of the system are no longer exciton or photon, but a new type of quasi-particles called the microcavity polaritons.

1.2 Dispersion of cavity polaritons

It is well-known that the optical properties of semiconductor materials are strongly dependent on their energy band structures. The energy band dispersion curves (*E-k* diagram) will dominate the semiconductor effective mass and density of states that determines the carrier population with optical pumping or electrical injection. Therefore, the controllable optoelectronic properties such as polarization and threshold condition can be demonstrated by means of band structure engineering. A typical example of band structure engineering is strained quantum wells employed in semiconductor lasers [8]. The modified valence band dispersion by strain in quantum wells decreases the density of states near the valence band edge. In addition, the strain effect induces the valence band splitting leading to the higher polarization degree in spontaneous emission.

Similarly, the dispersion of cavity polaritons also plays an important role in the optical properties. We will further describe the possible conditions causing different polariton dispersion curves in the following sections.

1.2.1 Dispersion curves of cavity photon and exciton

The planar microcavity confines the photon field in the direction of epitaxial growth but not in plane. The photon energy dispersion can be expressed as

$$E_{cav} = \frac{\hbar c}{n_{cav}} \sqrt{k_\perp^2 + k_{//}^2} \; , \tag{1.5}$$

where $k_{//}$ is the photon wave vector parallel to the microcavity plane, $k_\perp$ is the photon wave vector perpendicular to the microcavity plane and n_{cav} is the effective refractive index of cavity. For lowest order mode of cavity, $k_\perp = \pi/L_{cav}$, where L_{cav} is the effective cavity length. In the region $k_{//} \ll k_\perp$, we have

$$E_{cav} = \frac{\hbar c}{n_{cav}} \sqrt{\left(\frac{\pi}{L_{cav}}\right)^2 + k_{//}^2} \approx \frac{\hbar c}{n_{cav}} \frac{\pi}{L} + \frac{1}{2} \frac{\hbar c}{n_{cav}} \frac{L}{\pi} k_{//}^2 . \tag{1.6}$$

Since the in-plane dispersion takes this parabolic form for small $k_{//}$, the cavity photon acquires an effective mass of $n_{cav}\pi\hbar/(cL_{cav}) \sim 10^{-5}\ m_0$ [9].

Neglecting electron-hole exchange, the bare exciton dispersion can be expressed as

$$E_m^{Ex}(k) = E_m + \frac{\hbar^2 k^2}{2(m_e + m_h)} = E_g - \frac{Ry}{m^2} + \frac{\hbar^2 k^2}{2(m_e + m_h)} , \tag{1.7}$$

where m is the band index and

$$Ry = \frac{m_r e^4}{32\pi^2 \varepsilon^2 \varepsilon_0^2 \hbar^2} \tag{1.8}$$

is the effective Rydberg energy, E_g is the energy gap, and m_r is the reduced mass. For the 1s exciton state with $m = 1$, the dispersion of exciton shows a parabolic curve and the effective mass of exciton is about $10^{-1}\ m_0$.

1.2.2 Cavity polariton dispersion curves

Considering a two-level system composed of the lowest order mode of cavity and the ground state of exciton, The Hamiltonian of the cavity polaritons is given by the following 2×2 matrix:

$$\begin{bmatrix} E_{cav} & \Omega/2 \\ \Omega/2 & E_X \end{bmatrix}, \tag{1.9}$$

where Ω is the exciton-photon interaction energy. The energies of the polaritons, which are the eigen energies of the Hamiltonian, are deduced from the diagonalization procedure as

$$E_{LP,UP}(k_{//}) = \frac{1}{2}\left[E_{cav} + E_X \pm \sqrt{\Omega^2 + (E_{cav} - E_X)^2}\right]. \tag{1.10}$$

When the un-coupled exciton and photon are at resonance, $E_{cav} = E_X$, lower and upper

polariton energies have the minimum separation $E_{UP} - E_{LP} = \Omega$, which is often called

the Rabi splitting in analogy to the atomic cavity Rabi splitting. The dispersion curves

with higher and lower energies are termed as upper polariton branch (UPB) and lower

polariton branch (LPB), respectively. Fig. 1.5 shows a typical polariton dispersion

curves including UPB and LPB when the photon and exciton energies are the same at

the in-plane wave vector of zero. Under this condition, the exactly half-matter half-light

system is formed at $k_{//} = 0$. If the energy difference between photon and exciton is

increased, we will only probe the polariton branch with higher fraction of photon based

on the condition shown in Fig. 1.5.
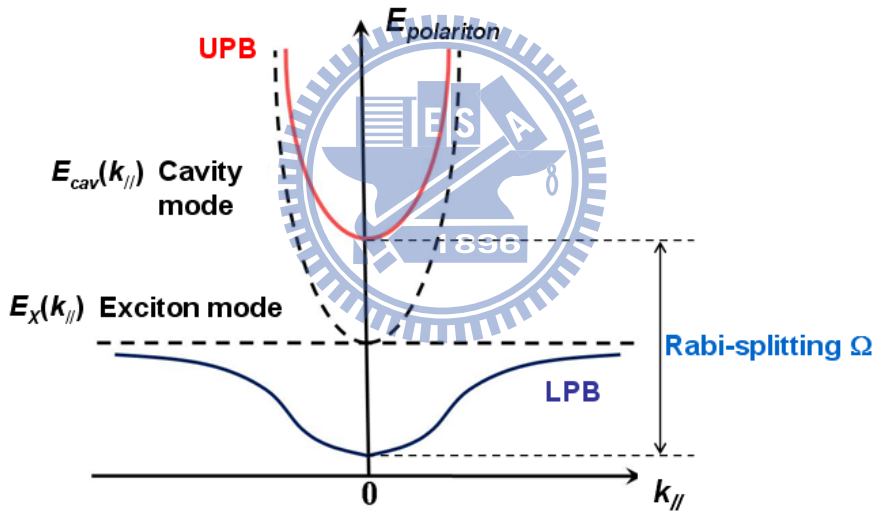
Fig. 1.5 Typical polariton dispersion curves including UPB and LPB.

1.2.3 Effective mass and density of states

It has been mentioned that the cavity photon has an effective mass $\sim 10^{-5} \, m_0$ and

the exciton has an effective mass $\sim 10^{-1} \, m_0$. Since the polaritons are mixed states of

excitons and photons, the effective mass of polariton can be referred to as a reduced

mass between exciton and photon, and is dependent on their fractions. The exciton and

photon fraction in lower polariton are given by the amplitude squared of $X_{k_{//}}$ and $C_{k_{//}}$

which are termed as the Hopfield coefficients [10], and satisfy

$$\left|X_{k/\!/}\right|^2 + \left|C_{k/\!/}\right|^2 = 1.$$ (1.11)

Let $\Delta E(k_{/\!/}) = E_X(k_{/\!/}) - E_{cav}(k_{/\!/})$, where $X_{k/\!/}$ and $C_{k/\!/}$ are given by

$$\left|X_{k/\!/}\right|^2 = \frac{1}{2}\left(1 + \frac{\Delta E(k_{/\!/})}{\sqrt{\Delta E(k_{/\!/})^2 + \Omega^2}}\right),$$ (1.12)

$$\left|C_{k/\!/}\right|^2 = \frac{1}{2}\left(1 - \frac{\Delta E(k_{/\!/})}{\sqrt{\Delta E(k_{/\!/})^2 + \Omega^2}}\right).$$ (1.13)

At $\Delta E(k_{/\!/}) = 0$, $|X_{k/\!/}|^2 = |C_{k/\!/}|^2 = 1/2$, lower and upper polaritons are exactly half photon half exciton.

Specifically, the polariton effective mass is the weighted harmonic mean of the mass of its exciton and photon components:

$$\frac{1}{m_{LPB}} = \frac{\left|X_{k/\!/}\right|^2}{m_X} + \frac{\left|C_{k/\!/}\right|^2}{m_{cav}},$$ (1.14)

$$\frac{1}{m_{LPB}} = \frac{\left|X_{k/\!/}\right|^2}{m_X} + \frac{\left|C_{k/\!/}\right|^2}{m_{cav}},$$ (1.15)

where $|X_{k/\!/}|^2$ and $|C_{k/\!/}|^2$ are the exciton and photon fractions. m_X is effective exciton mass of its center of mass motion, and m_{cav} is the effective cavity photon mass. Since m_{cav} is much smaller than m_X,

$$m_{LPB}(k_{/\!/} \sim 0) \approx \frac{m_{cav}}{\left|C_{k/\!/}\right|^2} \sim 10^{-4} m_X,$$ (1.16)

$$m_{UPB}(k_{/\!/} \sim 0) \approx \frac{m_{cav}}{\left|X_{k/\!/}\right|^2}.$$ (1.17)

The very small effective mass of lower polariton shows many different properties as

compared with micorcavities operating under weak-coupling regime. At high $k_{//}$ states, $\Delta E(k_{//}) \gg \Omega$, dispersions of the lower and upper polaritons converge to the exciton and photon dispersions, respectively. Hence, it is noteworthy that the effective mass of lower polariton changes by four order of magnitude from $k_{//} \sim 0$ to high $k_{//}$ states. This sharp difference in effective mass has directly corresponding changes in density of states of lower polaritons. This feature plays an important role in the energy relaxation dynamics of polaritons, which will be discussed in chapter 6.

1.2.4 Exciton-photon detuning

The typical polariton dispersion curves shown in Fig. 1.5 is the condition of the same photon and exciton energies at $k_{//} = 0$. We could define the energy difference δ between photon and exciton energies at zero in-plane wave vector. This energy difference is generally termed as detuning δ. Typically, when the photon energy is larger than exciton energy at $k_{//} = 0$, it is called positive detuning ($\delta = E_{cav} - E_X$). On the contrary, when the photon energy is smaller than exciton energy at $k_{//} = 0$, it is called negative detuning. In addition, if the photon energy is exactly equal to the exciton energy as shown in Fig. 1.5, we call this condition as zero detuning. Fig. 1.6 presents the in-plane polariton dispersion curves of two exciton-polariton modes in semiconductor microcavity for different detunings between exciton and photon modes: (a) positive detuning, (b) zero detuning, and (c) negative detuning. The horizontal dashed line shows un-coupled exciton mode and the curve dashed line shows un-coupled photon mode. The corresponding Hopfield coefficients are presented as well. In Fig. 1.6, it can be found that the polariton dispersion curves are significantly different based on varied exciton-photon detunings. In the three cases, the negative detuning shows the most obvious variation as compared with the un-coupled photon and exciton modes. Besides, an evident anticrossing can be observed in the condition of negative

detuning that will be one of the important signatures of strong coupling when we try to

probe the characteristics of microcavity polaritons.
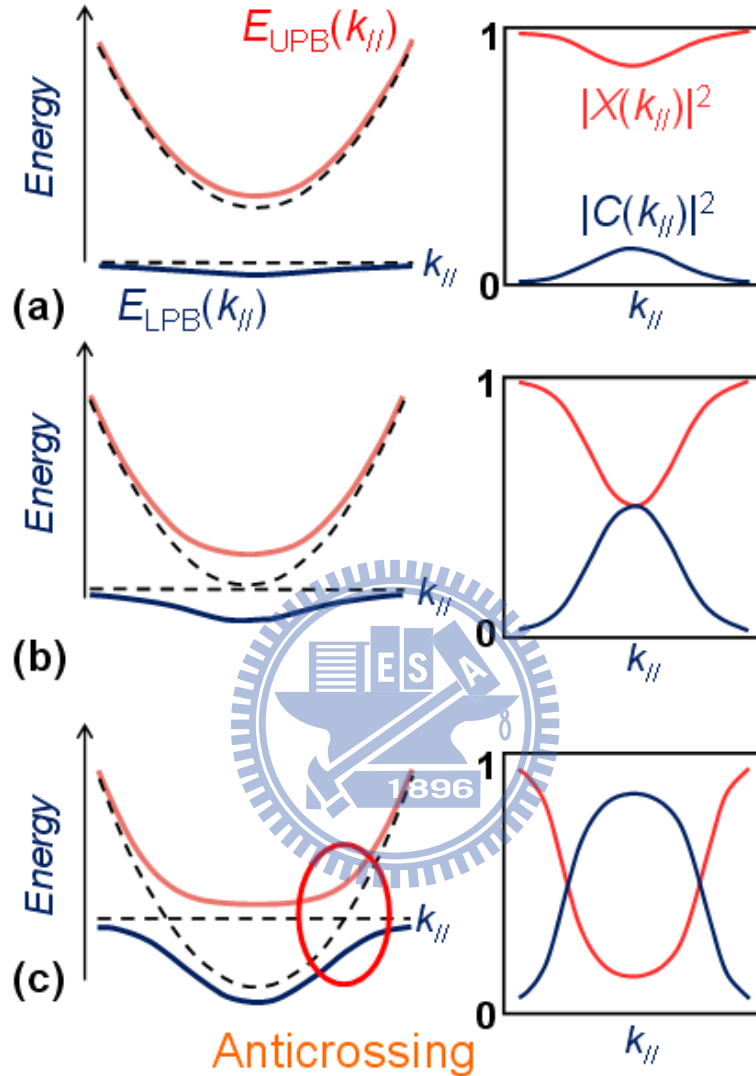
Fig. 1.6 In-plane polariton dispersion curves of two exciton-polariton modes in semiconductor microcavity for different detunings between exciton and photon modes: (a) positive detuning, (b) zero detuning, and (c) negative detuning. The horizontal dashed line shows un-coupled exciton mode and the curve dashed line shows un-coupled photon mode. The corresponding Hopfield coefficients are presented as well.

1.2.5 Experimental probe of cavity polariton dispersion

In reality, the finite lifetime of the cavity photon and exciton should be taken into

account in the strong coupling system. As a linear superposition of an exciton and a photon, the lifetime of the polaritons is directly determined by

$$\gamma_{LPB} = \left|X_{k//}\right|^2 \gamma_X + \left|C_{k//}\right|^2 \gamma_{cav}, \tag{1.18}$$

$$\gamma_{UPB} = \left|C_{k//}\right|^2 \gamma_X + \left|X_{k//}\right|^2 \gamma_{cav}, \tag{1.19}$$

where γ_{cav} is the out-coupling rate of a cavity photon due to imperfect mirrors, and γ_X is the non-radative decay rate of exciton. In typical semiconductor microcavities, we have $\gamma_{cav} = 1 \sim 10$ ps and $\gamma_X \sim 1$ ns. Therefore, the polariton lifetime is mainly dominated by the cavity photon lifetime:

$$\gamma_{LPB} \approx \left|C_{k//}\right|^2 \gamma_{cav}. \tag{1.20}$$

Polariton decays in the form of emitting a photon with the same $k_{//}$ and totoal energy $\hbar\omega = E_{LPB,UPB}$. The one-to-one correspondence between the internal polariton mode and the external out-coupled photon mode provides great convenience to experimental access to the strong coupling system. The external emitted photons carry direct information of the internal polaritons, such as the energy dispersion, population per mode, and statistics of the polaritons. Consequently, we could probe the internal properties of polaritons by collecting the emitted photons. From eq. (1.5) and consider the lowest order mode of cavity

$$E_{cav}(k_{//}) = \frac{\hbar c}{n_{cav}} \left[\left(\frac{\pi}{L_{cav}}\right)^2 + k_{//}^2 \right]^{1/2} = \frac{\hbar c}{n_{cav}} \frac{\pi}{L_{cav}} \left[1 + \left(\frac{L_{cav}}{\pi}\right)^2 k_{//}^2 \right]^{1/2}. \tag{1.21}$$

Let $E_0 = \hbar c \pi/(n_{cav}L_{cav})$

$$E_{cav}(k_{//}) = E_0 \left[1 + \frac{\hbar^2 c^2}{n_{cav}^2 E_0^2} k_{//}^2 \right]^{1/2}, \tag{1.22}$$

where E_0 represents the photon energy for $k_{//} = 0$. Each in-plane photom mode couples

15

only with an exciton state with the same $k_{//}$, which is related to the external angle of incidence θ via $k_{//} = (E_{cav}/\hbar c)\sin\theta$ and hence a particular $k_{//}$ can be selected by varying θ that can be expressed as

$$E_{cav}(\theta) = E_0 \left[1 - \left(\frac{\sin\theta}{n_{cav}} \right)^2 \right]^{-1/2}.$$ (1.23)

The polariton dispersion and associated phenomena can thus be studied in angular-dependent experiments.
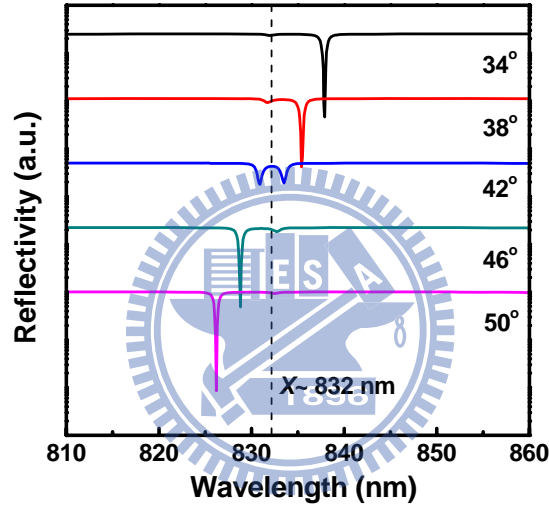
Fig. 1.7 Typical angle-resolved reflectivity spectra. It can be found that the cavity mode wavelength shifts toward shorter wavelength (higher energy) with increasing angle, and the cavity mode crosses the exciton mode when the angle is about 42°.

From the viewpoint of experiments, the negative exciton-photon detuning is a good choice because of the obvious characteristic of anticrossing. A common experimental technique is to perform the angle-resolved photoluminescence (PL) or reflectivity spectra. By increasing the detection angle, the cavity photon energy increases as well, and it may cross the exciton energy due to the condition of negative detuning. If the microcavity system is in strong coupling regime, the polariton anticrossing will be observed by the angle-resolved measurements. Fig. 1.7 shows typical angle-resolved

reflectivity spectra. It can be found that the cavity mode wavelength shifts toward shorter wavelength (higher energy) with increasing angle, and the cavity mode crosses the exciton mode when the angle is about 42°. Therefore, the angle-resolved measurements may exhibit the signature of anticrossing by tuning the cavity mode energy.

In addition to the method of tuning the cavity mode energy by angle-resolved measurement, the temperature-dependent measurements can change the exciton mode due to the temperature dependence of energy bandgap. Nevertheless, the cavity photon mode will be slightly influenced as the temperature changes. With increasing temperature, the cavity photon energy decreases due to the temperature dependence of the refractive index. In the meantime, the exciton energy decreases due to the reduction of bandgap energy. The amount of the redshift of both energies is different, since the exciton energy is much more strongly affected by the temperature change than the cavity mode energy. Therefore, the detuning between exciton and cavity modes changes with temperature. If the change of exciton energy can cross the cavity mode energy by varying temperature, the anitcrossing may be observed. Consequently, the temperature-dependent measurement is an important technique for mainly tuning the exciton energy.

1.3 Historical review of microcavity polaritons

The development of semiconductor microcavity is reviewed in this section from the pioneering work of Weisbuch *et al.* in 1992 [11]. The realization of Bose-Einstein condensation (BEC) in semiconductor microcavities will be discussed. In addition, it is systemically reviewed for the semiconductor microcavities consisting of various materials, such as III-V and II-VI compounds, and organic materials. Finally, we will focus on the discussion about the wide-bandgap semiconductor microcavities due to

their potential in the realization of room-temperature (RT) polariton devices.

1.3.1 Bose-Einstein condensation

Historically, studies of semiconductor microcavities have been started by the first observations of exciton-polaritons in GaAs-based resonators at low temperature from the work of Weisbuch *et al.* [11]. By probing different points on the wafer, the cavity mode energy can be changed due to the non-uniformity in cavity thickness. Fig. 1.8(a) shows 5-K reflectivity spectra from a GaAs-based microcavity structure. Various detuning conditions between cavity and exciton modes are obtained by choosing various points on the wafer. Fig. 1.8(b) shows the reflectivity peak positions as a function of cavity detuning. A clear anticrossing is observed.
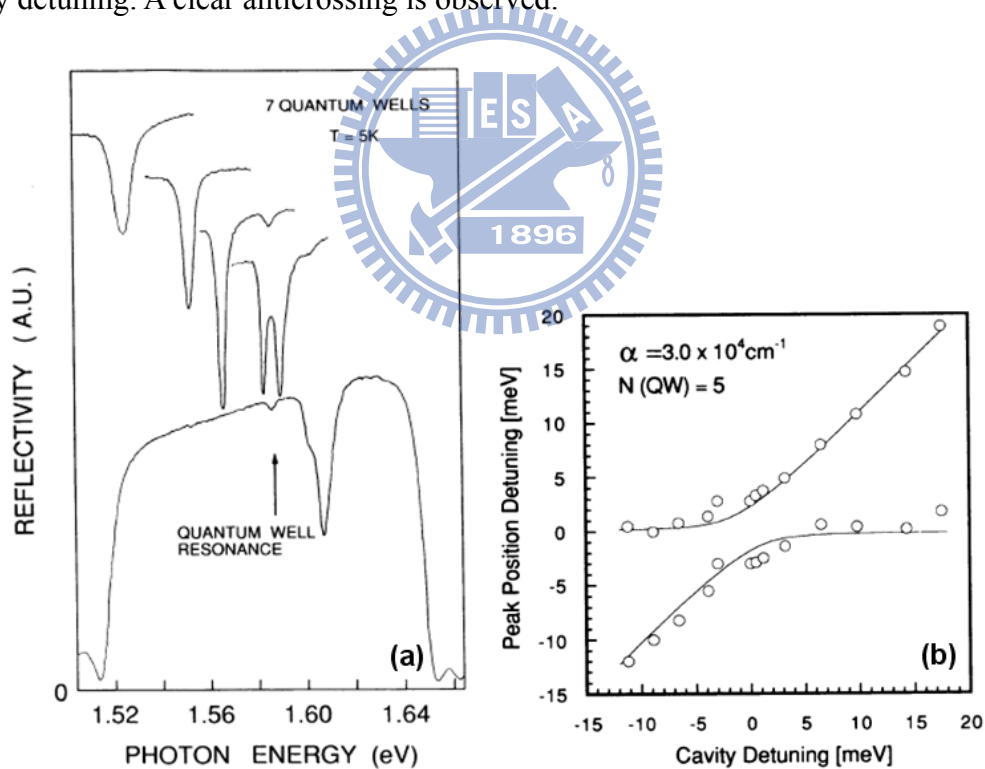
Fig. 1.8 (a) 5-K reflectivity spectra from a GaAs-based microcavity structure. Various detuning conditions between cavity and exciton modes are obtained by choosing various points on the wafer. (b) Reflectivity peak positions as a function of cavity detuning. A clear anticrossing is observed. (After [11])

After the first demonstration of strong coupling in semiconductor microcavity,

many researchers turn their attention to the study of BEC in solid-state system. Since both excitons and photons are bosons, so are the polaritons. As exciton-polaritons are bosons, they can occupy the same quantum state and therefore can undergo BEC. Atomic BEC systems have been proposed for a long time and the conclusive evidence for BEC system came first from dilute atomic gases in 1995 [12]. Nevertheless, the critical temperature of phase transitions in atomic system requires extremely low temperature (1 nK ~ 1 μK) due to the relatively large mass of atoms. As for the microcavity polariton system, near the center of the Brillouin zone the LPB has a small effective mass, which is about nine orders of magnitude smaller than the atomic mass of diluted atom gases. Therefore, it is possible to realize the BEC at temperatures even above RT in a microcavity polariton system.
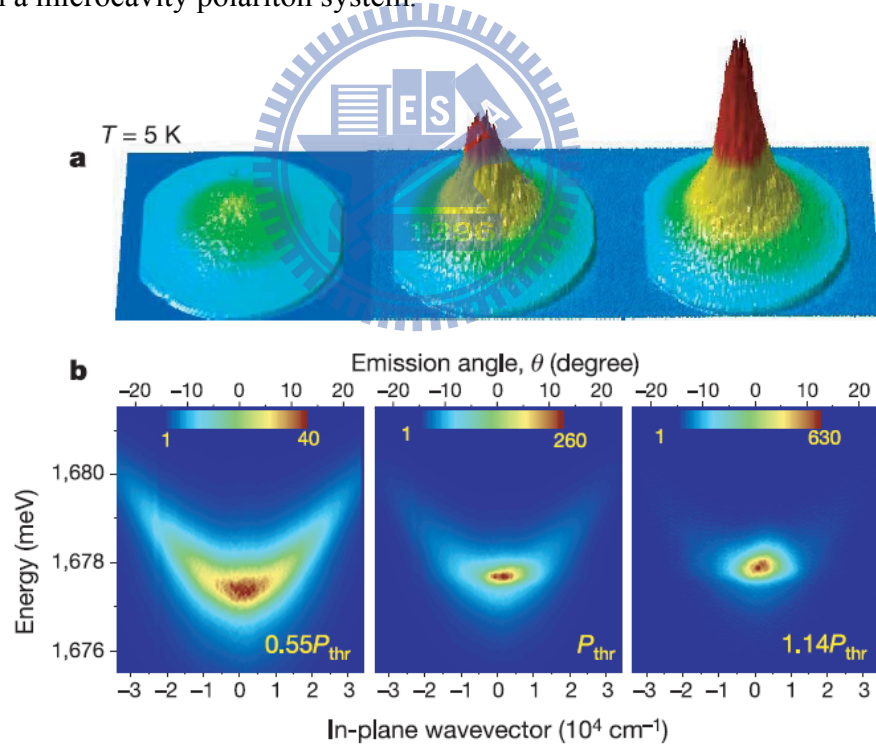
Fig. 1.9 (a) Far-field emission measured at 5 K for three excitation intensities. (b) Polariton population with increasing pumping power. (After [13])

BEC of exciton-polaritons was for the first time observed by Kasprzak *et al.* in a CdTe-based microcavity at 19 K [13]. Fig. 1.9(a) shows the far-field emission measured

at 5 K for three excitation intensities. Below threshold, the emission exhibits a smooth distribution around $k_{//} = 0$. When the excitation intensity is increased, the emission from the zero momentum state becomes predominant at threshold and a sharp peak forms at $k_{//} = 0$ above threshold. Fig. 1.9(b) shows the energy and angle-resolved emission intensities. The width of the momentum distribution shrinks with increasing excitation intensity, and above threshold, the emission mainly comes from the lowest energy state at $k_{//} = 0$. The phase-transition character of the phenomenon is clearly observed that demonstrates the condensation of exciton-polaritons in a semiconductor microcavity.

1.3.2 Inorganic and organic semiconductor microcavities

Since the first demonstration of strong coupling in GaAs-based microcavities, many research groups are devoted to the study of various optical properties in GaAs microcavities due to the well-developed epitaxial technique and lattice-matched DBRs. Deng *et al.* realized a phase transition from a classical thermal mixed state to a quantum-mechanical pure state of exciton polaritons in a GaAs microcavity in 2002 [14]. Supporting evidence is obtained from the observation of a nonlinear threshold behavior in the pump-intensity dependence of the emission, a polariton-like dispersion relation above threshold, and a decrease of the relaxation time into the lower polariton states. After that, they further demonstrated a polariton lasing in a GaAs microcavity at 4 K in 2003 [15]. The clear discrimination between photon and polariton lasing was observed in the same structures. Fig. 1.10 presents the number of LPBs and cavity photons per mode versus the injected carrier density for a polariton laser in scheme I (triangles) and a photon laser in scheme II (circles), respectively. The phase transitions in both schemes are clearly observed.
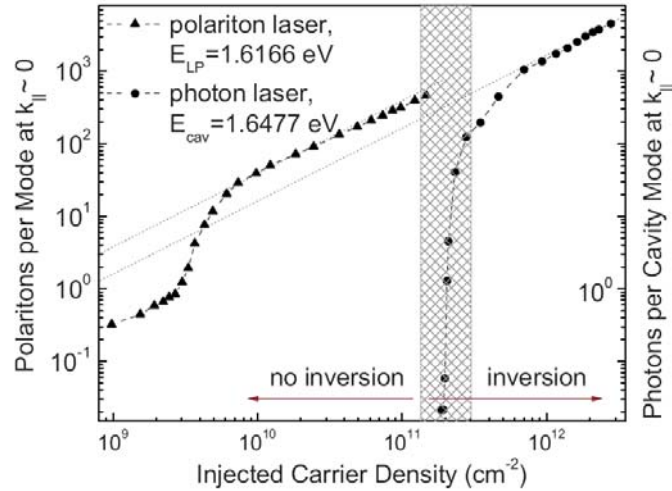
Fig. 1.10 Number of LPBs and cavity photons per mode versus the injected carrier density for a polariton laser in scheme I (triangles) and a photon laser in scheme II (circles), respectively. (After [15])

In 2008, Tsintzos *et al.* firstly demonstrated an electrically pumped GaAs polariton LED, which emits directly from polariton states at a temperature of 235 K [16]. Fig. 1.11(a) shows the GaAs polariton LED structure consisting of a $5\lambda/2$ cavity surrounded by two doped GaAs/AlAs DBRs. Fig. 1.11(b) plots the electric field and refractive index distribution along the structure. The authors measured the angle-resolved electroluminescence (EL) spectra based on two different detunings, and the evident anticrossing between exciton and cavity modes was observed, as shown in Fig. 1.12. In the next year, Tsintzos *et al.* reported an electrically pumped GaAs exciton-polariton LED at RT [17]. Temperature and angle-resolved EL measurements on a polariton LED clearly show the persistence of Rabi splitting and anticrossing behavior at a temperature as high as 315 K. They can push the cutoff temperature for the strong coupling regime beyond RT by increasing the number of quantum wells in the structure. Consequently, these results exhibit the potential properties in GaAs-based microcavities for the application of polariton-based devices.
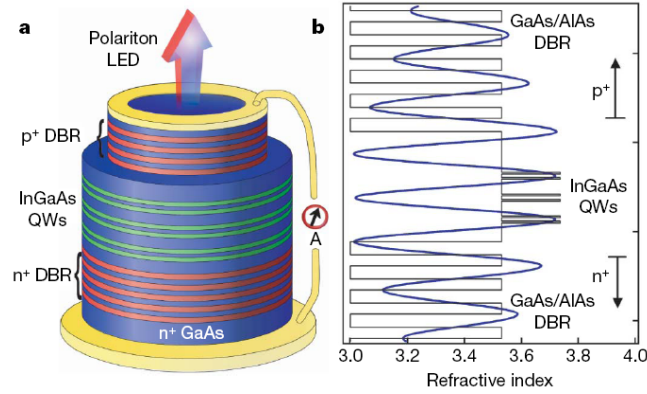
Fig. 1.11 (a) GaAs polariton LED structure consists of a 5λ/2 cavity surrounded by two doped GaAs/AlAs DBRs. (b) Electric field and refractive index distribution along the structure. (After [16])
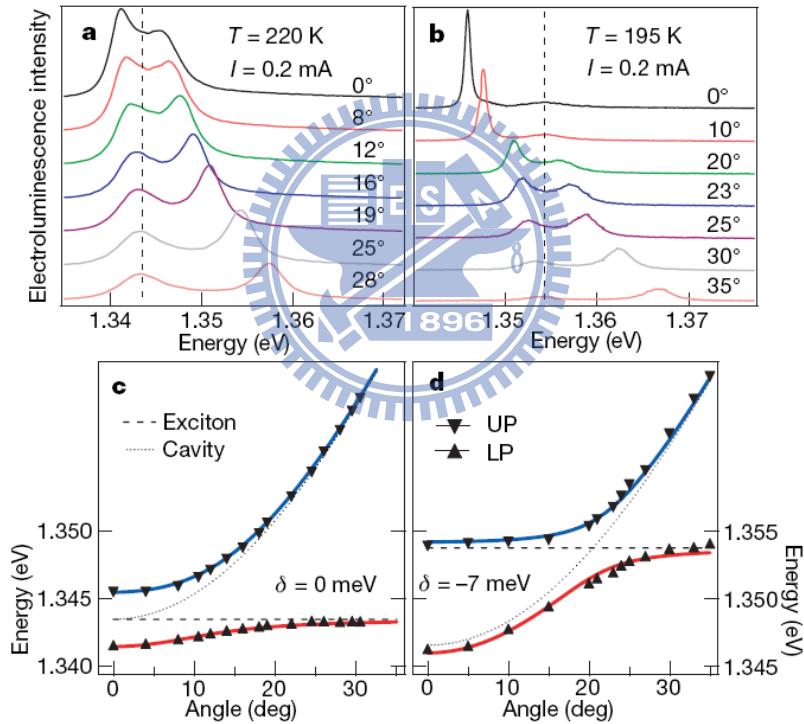
Fig. 1.12 (a) (b) Electrically pumped spectra as a function of collection angle for zero and negative detuning conditions. (b) Polariton energy dispersions. Excellent fits are obtained using a coupled harmonic oscillator model for different detunings. (After [16])

Although the promising results have been demonstrated in GaAs-based microcavities, the disadvantage of GaAs material is the small exciton binding energy ~

10 meV because of the strong dielectric screening in solids and a small effective mass ratio of the hole to the electron [15]. Therefore, the organic semiconductors with huge exciton oscillator strength result in a large polariton splitting of around 100 meV. The strong-coupling regime at RT has already been demonstrated in organic microcavities [18], [19]. Nevertheless, the low crystal quality of such materials often leads to emission spectra that are superposed from the emission from localized and delocalized states.

1.3.3 Wide-bandgap semiconductor microcavities

In order to overcome the low exciton binding energy in GaAs materials and low crystal quality in organic materials, another attractive candidate is the wide-bandgap semiconductor materials. Polariton optoelectronic devices operating at high temperatures require wide-bandgap material systems which can provide larger exciton binding energy than GaAs and can assure the existence of excitons at that temperature. In this sense, nitride-based material systems have attracted much attention in this research field due to their large exciton binding energy of about 26 meV for GaN bulk layers [20] and about 40–50 meV for GaN-based quantum-well structures due to the quantum confinement effect [21]. However, the growth and fabrication of high-reflectivity nitride-based DBRs and high-Q cavities with high-quality GaN-based quantum wells are very difficult due to the large lattice mismatch between AlN and GaN, and the lack of suitable substrates [22]. In spite of the difficulty in fabrication of nitride-based microcavities, many research groups still demonstrated excellent research results in recent years. In 2007, Christopoulos *et al.* firstly presented the realization of a polariton lasing at RT in a bulk GaN microcavity [23]. Thereafter, they further reported the RT polariton lasing in a GaN/AlGaN multiple-quantum-well microcavity in 2008 [24]. A large Rabi splitting of about 56 meV was observed in this structure. The angular

and spectrally resolved PL measurements below and above threshold are shown in Figs. 1.13(a), and 1.13(b), respectively. A nonlinear emission can be clearly observed at the center of the LPB when the pumping power is above threshold at RT.
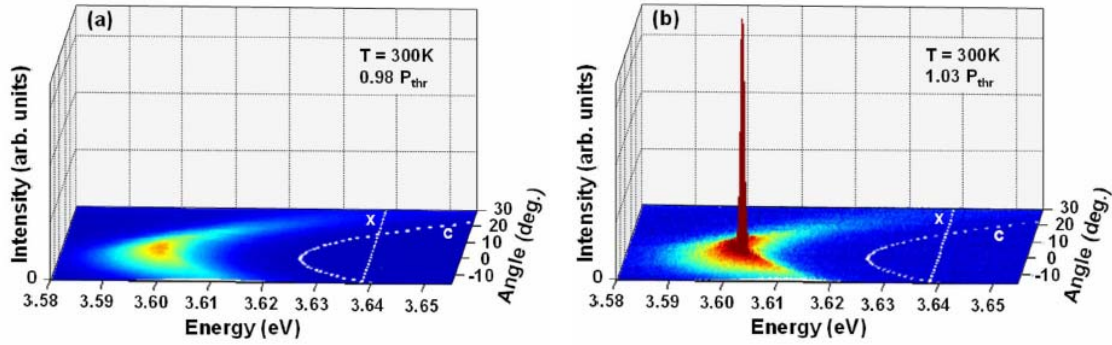
Fig. 1.13 Three-dimensional representation of the far-field emission with emission intensity displayed on the vertical axis (a) below and (b) above threshold. C and X are also reported. (After [24])

In addition to the nitride-based microcavities, ZnO is another promising wide-bandgap material because of its large oscillator strength [25], and exciton binding energy (~60 meV in the bulk layer) [26], [27]. Theoretical analysis has expected that a bulk ZnO microcavity is a potentially excellent candidate for the realization of RT polariton lasers [28], [29]. Consequently, several experimental results about ZnO microcavities have been reported in recent years. In 2008, Schmidt-Grund *et al.* demonstrated microcavity structures with ZnO as the cavity surrounded with ZrO_2/MgO DBRs [30]. The maximum Rabi splitting value of about 78 meV was estimated from the coupling of the excitons and the Bragg band-edge modes. Furthermore, Médard *et al.* reported hybrid ZnO microcavities with bottom 7.5-pair $Al_{0.2}Ga_{0.8}N$/AlN DBR grown on Si(111) substrates and 10 nm aluminum top mirrors in 2009 [31]. The maximum Rabi splitting of about 70 meV was obtained at 5 K. In addition, Shimada *et al.* demonstrated another kind of hybrid microcavities composed of 29-pair $Al_{0.5}Ga_{0.5}N$/GaN DBR at the bottom of the ZnO cavity layer and 8-pair SiO_2/Si_3N_4 DBR

as the top mirror [32]. The Rabi splitting was estimated to be ~50 meV at RT.

1.4 Outline of thesis

This thesis is an experimental study of the strong coupling regime in wide-bandgap semiconductor microcavities. We first introduce in chapter 2 the experimental instruments and physical models employed in this thesis. The experimental instruments include the metal organic chemical vapor deposition (MOCVD) system which is used for the growth of nitride-based DBRs and quantum wells. PL system and reflectance measurement are important approaches to probe the properties of polaritons. In addition, the physical models include the transfer matrix method which is commonly used for the calculation of reflectivity spectrum in a multiple layer structures. Besides, the physical model used to describe the exciton oscillator will be presented, and the quasiparitcle model is helpful for the estimation of exciton and photon fractions with different detunings.

Chapter 3 contains the introduction of nitride-based DBRs and the experimental results of high-reflectivity AlN/GaN or AlN/AlGaN DBRs ranging from blue-violet to ultraviolet. Furthermore, a theoretical study about the comparison of strong coupling regimes in bulk GaAs, GaN, and ZnO is provided in chapter 4. Various physical mechanisms leading to the differences among these three materials will be systematically discussed. In chapter 5, the experimental observation of strong coupling regime in hybrid ZnO microcavities is demonstrated. Chapter 6 shows a systematical investigation about the temperature- and detuning-dependent polariton relaxation. A clear bottleneck effect will be presented. Furthermore, the observation of RT polariton lasing in ZnO microcavity will be exhibited. On the other hand, we will demonstrate electrically pumped InGaN/GaN LED in strong coupling regime in chapter 7. Finally, chapter 8 gives a conclusion about the research results obtained in the thesis.

Chapter 2 Experimental instruments and physical models

Experimental instruments employed in this research contain MOCVD, PL, and reflectivity spectra measurements. MOCVD systems have been widely used in modern semiconductor industry, which provide a way to grow high-quality semiconductor films and sharp heterostructures. In addition, as mentioned in section 1.2.5, the measurements of angle-resolved PL and reflectivity spectra are critical methods for probing the polariton dispersions. This chapter will describe the setup of these optical systems in detail. Furthermore, the physical models containing transfer matrix method, exciton oscillators, and quasiparticle model will be shown in this chapter as well.

2.1 Metal organic chemical vapor deposition

MOCVD is currently the most widely used technology for nitride compound semiconductor thin film growth. Actually, most of the optoelectronic commercial device structures are fabricated using MOCVD. Its potentials have been proven by producing high quality epitaxial layers with excellent surface morphology and a precise control over layer thickness and uniformity. Several epitaxial crystal growth technologies for an impressive array of commercial devices are also carried out by MOCVD, such as lasers, LEDs, photocathodes, heterostructure bipolar transistors, photodetectors, and solar cells.

2.1.1 MOCVD equipment

MOCVD growth is facilitated by introducing group III precursors and NH_3 with carrier gases into a reactor under appropriate growth temperature and growth processes. In general, a typical MOCVD system consists of four major parts: growth reactor, gas delivery system, heating system, and exhaust system. The reactor system for carrying out CVD processes must provide several basic functions to all types of systems. Most

reactants and diluent gases were allowed to move to the reaction site and absorb activation energy while maintaining a specific system pressure and temperature.

The reaction chamber is more like the heart of human which connectes the vessel. All kinds of source gases are mixed and introduced into a heated zone where an appropriate substrate is placed, and then the basic pyrolysis reactions described above take place. There are two basic MOCVD reaction chamber geometries commonly used for epitaxial III-nitride growth [33]. One is vertical reactor chamber, the other is horizontal one, which are mainly fabricated by famous companies Veeco and Aixtron [34], [35]. For both designs, cold-wall systems are attached which contain a relatively small diameter inlet into some form of transition region and make use of an indirectly heated (filament or radio-frequency induction heated) silicon carbide-coated graphite susceptor.

The gas delivery system consists of all the valves, mass flow controllers, regulators, and equipment for transporting sources for further growth in the reactor chamber. Therefore, it is important to control the gas flows, mixtures, and gas distribution into the chamber as well as to keep gas plumbing clean and leakage-free.

The substrate is placed on a wafer carrier in reactor under a relative low pressure to outside environment. Therefore, one buffer zone is necessary which supplies a pressure-control space for loading samples, such as the load-lock chamber in Veeco system and glove box in Aixtron system. In addition, we need to ensure the safety of using MOCVD which is the most important issue because of various toxic gases used as sources. Process gases should be piped in leak-free plumbing with nitrogen or vacuum in the outer tube. Wasted gases should be processed with filters, combustion discharge, oxidation, wet chemical scrubber, or a combination of these methods. Automatic shutdown of source gases and a switch to inert purge gases should take place in the event of power failure when inadequate backup power is available.

27

2.1.2 *In-situ* reflectance monitor for III-nitride growth

An *in-situ* normal incidence reflectometry is usually attached in MOCVD machine which is capable of monitoring the growth processes in real time. The overall reflectivity can be used to determine the growth rate and growth status. During the growth, the interference conditions change, causing the sample reflectivity to oscillate with a frequency determined by the growth rate, the incident wavelength, and refractive index of the layers. Fig. 2.1 shows the in-situ measurement data during GaN growth. It is clear to see a normal GaN growth process has a two-step process which is a low temperature buffer followed by high temperature GaN growth. Pre-baking substrate is the first step. Chamber temperature ramps up to 1100 ºC and the substrate is heated around 10 minutes under hydrogen ambient. The substrate is clean and has a good surface quality after this process. NH_3 could be introduced which leads to a nitridation of the substrate surface for the addition growth application such as N-polar GaN growth [36]. Then, the growth of low temperature GaN is followed. After the pre-baking, the temperature ramps down to 550 ºC. A GaN or AlN nucleation layer is deposited on the substrate for a couple of minutes. The purpose of nucleation layer is to reduce the residual stress from lattice mismatch between GaN and sapphire and avoid producing many intrinsic defects. Nucleation layer thickness is an important factor affecting GaN layer quality. The thickness is generally ranging between 20 ~ 40 nm.

Thermal activation of the nucleation layer is the third step. The crystal quality of the nucleation layer is poor due to low temperature growth. The nucleation layer is recrystallized while ramping the temperature to 1050 ºC under NH_3 ambient. These two processes result in strain relief caused by lattice mismatch from the substrate and high density of nucleation which facilitate to further GaN growth.
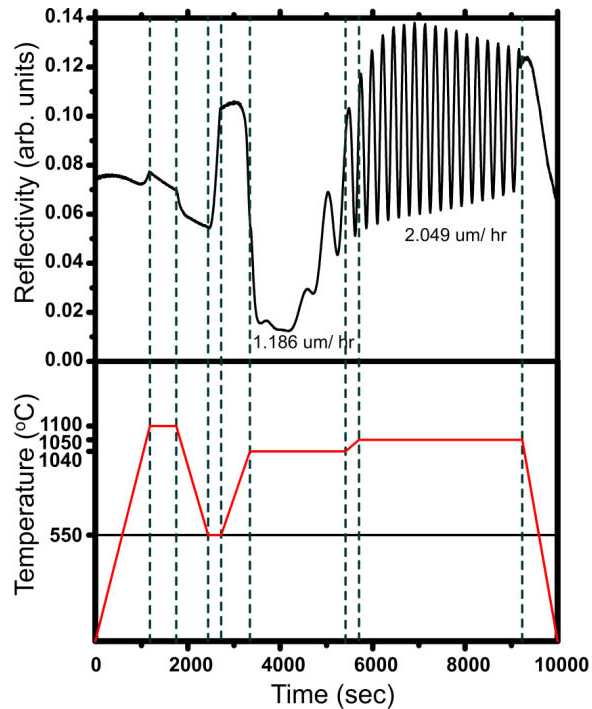
Fig. 2.1 *In-situ* reflectance measurement during MOCVD growth of bulk GaN on sapphire substrate.

Firth step is the rough GaN growth. Before the main GaN layer growth, a rough GaN with low growth rate is grown at 1040 ℃. The growth rate is lower than that of main GaN growth. This process improves the main GaN crystal quality. Finally, the main GaN layer is also grown at around 1050 ℃. The typical growth rate in MOCVD growth is about 2 μm/ hour which could be adjusted mainly by TMGa flow rate, growth temperature and V/III molar ratio.

2.2 Photoluminescence and reflectance measurement

Photoluminescence (PL) spectroscopy is an optical measurement method to examine the quality and optical characteristics of material, which is an un-contact and nondestructive technology. PL is the emission of light from a material under optical excitation. To excite the material to induce the emission, the energy of the excited light source should be higher than the band gap energy of the material. When the excited

light is absorbed by material, electrons in the valence band would get the energy to jump into the conduction band then produce a hole in the valence band. When an excited electron in an excited state returns to the initial state to comply with the energy conservation law, it will emit a photon whose energy is equal to the energy difference between the excited state and the initial state. In this section, the extended topics related to PL will be introduced which include temperature-dependent PL, micro-PL (μ-PL) and angle-resolved PL. In addition, the measurement of reflectivity and angle-resolved reflectivity spectra will also be introduced. The detailed description of optical systems will be reported in this section.

2.2.1 Temperature- and power-dependent photoluminescence

In general, the PL spectra measured at RT show relatively broad linewidths due to the homogeneous broadening induced by lattice vibration, which is referred to as phonons. Besides, the PL emission spectrum may include different optical transitions that cannot be discriminated at RT because of the broad linewidth. Therefore, the measurement of low-temperature PL spectrum is an important technique to probe the individual optical transition from different mechanisms. For some semiconductor materials with low exciton binding energy, the low-temperature PL measurement is a way to analyze the optical properties of excitons. As for the semiconductor microcavities, since the exciton energy will change with temperature due to temperature-dependent bandgap energy, it may cross the cavity photon mode, and then the anticrossing could be observed. Consequently, the measurement of temperature-dependent PL is another approach to probe the strong coupling regime.

The power-dependent PL measurement can be used to study the difference of emission spectra under low and high excitation energies. The shift of emission wavelength with increasing pumping power includes the information about density of

states and energy band profile. A typical example is the nitride-based quantum-well structures. Generally, it is observed that the PL emission wavelength shows a blue shift with increasing pumping power, which is induced by the Coulomb screening of the quantum confined Stark effect [37]. As for the power-dependent PL used in the study of semiconductor microcavities, since the exciton-polaritons are mixed cavity photons and excitons, the increased pumping power will create more excitons, which may cause the excitons to beyond the Mott density and then become free electron-hole pairs. Hence, we can use the power-dependent PL to observe the evolution of Rabi splitting. In addition, one of the mechanisms of polariton relaxation is the exciton-exciton scattering. We can observe the distribution of polariton emission from the power-dependent PL that is a critical technique to study the polariton bottleneck effect.

2.2.2 Micro photoluminescence

Due to the progress of epitaxy technology and the understanding of quantum mechanics, low-dimension nanostructures such as nanorod, and quantum dots have attracted much attention. Therefore, the measuring tool to probe such nanostructure is necessary. In general, the focused laser spot size of PL system is about 100 μm, which is not small enough to probe the properties of individual nanostructure such as nanorod or quantum dots. Therefore, the μ-PL system has been developed. This system uses optical objective to replace optical lens to focus laser light, with the minimum laser spot of ~3 μm. By using this system we can observe the optical properties of nanostructure, obtain higher excitation power density and scan the emission pattern of sample.

The μ-PL system is an important technique to probe the local cavity quality, especially for wide-bandgap microcavities. Because of the difficulty in growth of high-quality wide-bandgap microcavities, the microscopic fluctuation in thickness, interface roughness, and crystal imperfection will cause the inhomogeneous broadening

of the cavity mode when we use the incident laser beam with a larger spot size. Therefore, the μ-PL system can reduce the effect of inhomogeneous broadening and then probe the local cavity Q value [21].
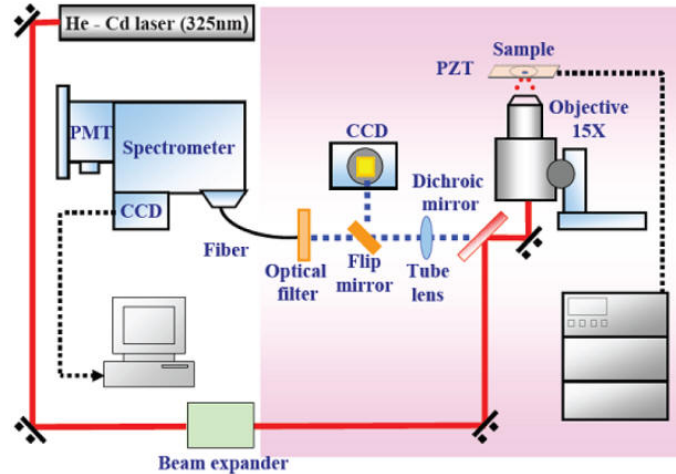
Fig. 2.2 Schematic sketch of a typical μ-PL system.

Fig. 2.2 shows the setup of μ-PL system. The sample is excited by a He-Cd laser operating at 325 nm with a power of 40 mW. First, the beam of laser light is expanded by beam expander, and then focused into a spot with 3 μm in diameter on sample by 15× objective. The emission light from sample surface was collected along the normal direction by a 400 μm core UV optical fiber and detected by a photo multiplier tube (PMT) or charge coupled display (CCD). Furthermore, μ-PL spectrum is dispersed by a 320 mm monochromator (Jobin–Yvon Triax 320). The wavelength resolution is about 1 nm by using a 300 grooves/mm grating and a slit of 0.1 mm. The position of sample can be controlled by piezo stage PZT to scan the luminescence image of sample.

2.2.3 Angle-resolved photoluminescence and reflectance

As mentioned in section 1.2.5, the one-to-one correspondence between the internal polariton mode and the external out-coupled photon mode provides great convenience to experimental access to the strong coupling system. Therefore, the angle-resolved PL

is a common optical system to measure the polariton dispersion curves [38]. Fig. 2.3 shows the schematic sketch of an angle-resolved PL system. The excitation source of the PL measurements is a 266 nm radiation from a frequency tripled Ti:sapphire laser. The PL emission light from the sample surface was collected using a UV optical fiber with 600 μm core mounted on a rotating stage with an angular resolution of ~1°, and detected by a liquid nitrogen cooled charge-coupled device attached to a 320 mm single monochromator with a spectral resolution of about 0.2 nm. The laser source can be changed to be a Nd:YAG or Nd:YVO$_4$ laser.
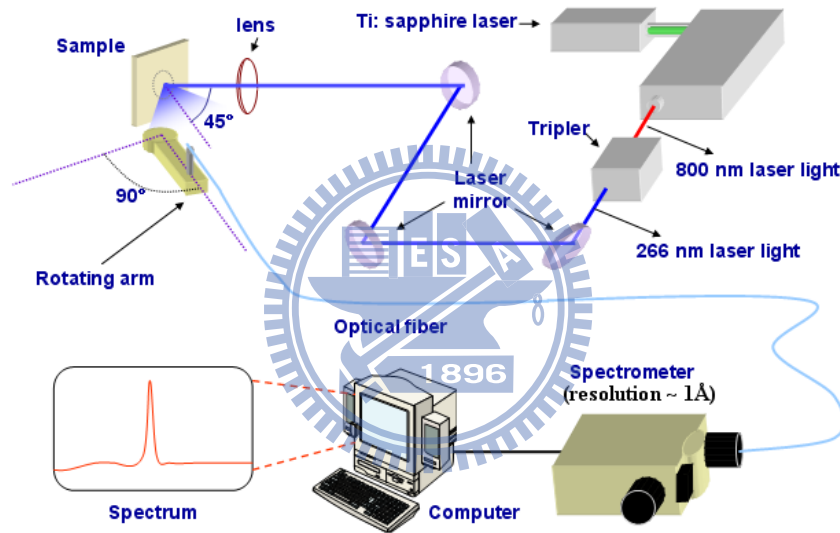
Fig. 2.3 Schematic sketch of an angle-resolved PL system

The measurement of reflectivity spectrum is widely used to probe the reflectivity of DBRs and microcavity structures. The measured parameters including the reflectivity and stopband width are important properties for a DBR and optical microcavity. The measurement of angle-resolved reflectivity spectra has similar function, which can be used to probe the anticrossing of cavity polaritons.

The angle-resolved reflectivity measurements were carried out by using a two arm goniometer and a xenon lamp was employed as a white light source combined with a 100 μm core optical fiber. The reflected light was then collected by a 600 μm core UV

optical fiber mounted on a rotating stage with an angular resolution of ~1° and detected

by a liquid nitrogen cooled CCD attached to a 320 mm single monochromator with a

spectral resolution of about 0.2 nm.
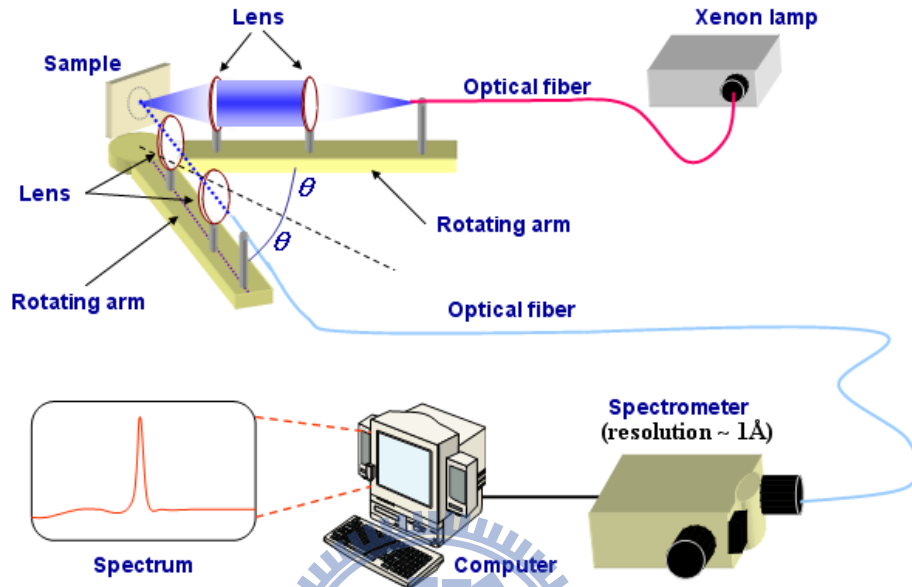
Fig. 2.4 Schematic sketch of an angle-resolved reflectivity system

2.3 Theoretical considerations in microcavity polaritons

The physical models used in this thesis will be described in detail in this section.

The active layer of a semiconductor microcavity is modeled by a Lorentz oscillator

dispersive dielectric function. Then, the quasiparticle model is employed to access the

homogeneous broadening of the eigenstates through the imaginary part of the energy

and the expansion coefficients of the eigenstates on the exciton-photon basis. Finally,

the transfer matrix method will be introduced to calculate the reflectivity spectra of

DBRs and microcavity structures.

2.3.1 Exciton oscillator

In our simulation, the resonant exciton is modeled by a Lorentz oscillator

dispersive dielectric function, which can be expressed as follows [39], [40], [41]:

$$\varepsilon_r(E) = \varepsilon_b + \frac{B}{E_0^2 - E^2 + i\Gamma E}, \tag{2.1}$$

where E_0 is the exciton transition energy. The physical parameter B is related to the exciton oscillator strength and Γ is the broadening parameter. To further take the inhomogeneous broadening into account, the dielectric function is modified as [42]

$$\varepsilon_r(E) = \varepsilon_b + \sum_i \frac{1}{\sqrt{2\pi}\Delta_i} \int \frac{\alpha_i E_{0i}^2 e^{-(x-E_{0i})^2/2\Delta_i^2}}{x^2 - E^2 - i\Gamma_i E} dx, \tag{2.2}$$

where ε_b is a background dielectric function due to all contributions far from the excitonic transitions. In the transparent region, a Sellemier law deduced from both ellipsometry and reflectivity measurements is considered [41]

$$\varepsilon_b = n^2(\lambda) = a + \frac{b\lambda^2}{\lambda^2 - c^2}. \tag{2.3}$$

The excitonic transitions are modelled by using Lorentz oscillators corresponding to the fundamental and excited excitonic states. The average transition energy is called E_{0i} and α_i is the polarizability. The latter is linked to the longitudinal transverse splitting ($\hbar\omega_{LT}$) through the following formula

$$\hbar\omega_{LT} = \frac{\alpha}{2\varepsilon_\infty} E_0. \tag{2.4}$$

To take into account an inhomogeneous broadening mostly due to strain fluctuations, a Gaussian distribution is used with a broadening parameter, Δ_i. At low temperature, a homogeneous broadening parameter, Γ_i, which represents the broadening arising from the scattering by impurities or exciton-exciton interactions is considered.

2.3.2 Quasiparticle model

When taking into account the finite lifetime of the cavity photon and exciton, the

imaginary part of the energy can be applied into the Hamiltonian. Considering a two-level system composed of the lowest order mode of cavity and the ground state of exciton, The Hamiltonian of the cavity polaritons with finite lifetime is given by the following 2×2 matrix:

$$
\begin{bmatrix}
E_{cav} - i\gamma_{cav} & \Omega/2 \\
\Omega/2 & E_X - i\gamma_X
\end{bmatrix},
$$
(2.5)

where γ_{cav} is the out-coupling rate (homogeneous broadening) of a cavity photon, and γ_X is the non-radative decay rate (homogeneous broadening) of exciton. The energies of the polaritons, which are the eigen energies of the Hamiltonian, are deduced from the diagonalization procedure as

$$
E_{LP,UP}(k_{//}) = \frac{1}{2}\Big[E_{cav} + E_X - i(\gamma_{cav} + \gamma_X) \\
\pm \sqrt{\Omega^2 + \left[(E_X - E_{cav}) + i(\gamma_{cav} - \gamma_X)\right]^2}\Big]
$$
(2.6)

Thus, the coupling strength must be larger than half of the difference in decay rates to exhibit anticrossing, i.e., to have polaritons as the new eigen modes. When $\Omega \gg (\gamma_{cav} - \gamma_X)$, the system is in the strong coupling regime. Furthermore, the eigen functions of the Hamiltonian represent the fraction of cavity and exciton modes at specific $k_{//}$, which will be used to discuss the effect of polariton bottleneck in chapter 6.

2.3.3 Transfer matrix method

In order to estimate the reflectivity and mirror stopband of a certain DBR mirror, numerical calculation of multilayered mirrors is necessary. Transfer matrix method is generally used to calculate the reflection spectra of multilayered mirrors with abrupt interfaces [43].
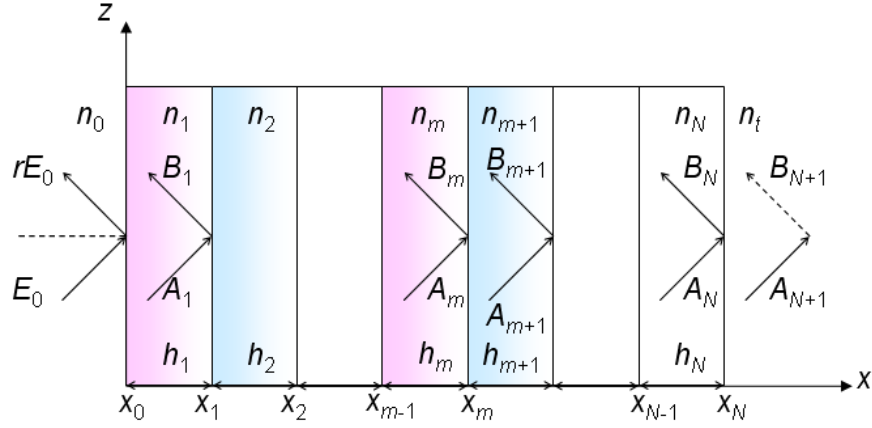
Fig. 2.5 A plane wave with TE polarization is incident on a multilayered medium.

As shown in Fig. 2.5, for a TE polarized incident wave

$$\vec{E}_i = \hat{y}E_0 e^{ik_{0x}x+ik_{0z}z} ,$$
(2.7)

and, for the reflected wave, the electric field can be expressed as

$$\vec{E}_r = \hat{y}rE_0 e^{-ik_{0x}x+ik_{0z}z} .$$
(2.8)

In the mth layer, $x_{m-1} \leq x \leq x_m$, the electric field and magnetic field are given by

$$\vec{E}_m = \hat{y}E_y^m ,$$

$$E_y^m = \left(A_m e^{ik_{mx}(x-x_m)} + B_m e^{-ik_{mx}(x-x_m)} \right) e^{ik_{mz}z} ,$$
(2.9)

$$H_z^m = \frac{k_{mx}}{\omega\mu_0} \left(A_m e^{ik_{mx}(x-x_m)} - B_m e^{-ik_{mx}(x-x_m)} \right) e^{ik_{mz}z} ,$$
(2.10)

where $k_{mz} = k_{0z}$ for all m,

$$k_{mx} = \frac{2\pi n_m}{\lambda} \cos\theta + i\alpha_m ,$$
(2.11)

where α_m is the scattering and absorption loss in the mth layer. Employing the boundary conditions at $x = x_m$, we have

$$\begin{bmatrix} A_m \\ B_m \end{bmatrix} = M_{m(m+1)} \begin{bmatrix} A_{m+1} \\ B_{m+1} \end{bmatrix},$$

(2.12)

where

$$M_{m(m+1)} = \frac{1}{2} \begin{bmatrix} (1 + P_{m(m+1)})e^{-ik_{(m+1)x}h_{m+1}} & (1 - P_{m(m+1)})e^{ik_{(m+1)x}h_{m+1}} \\ (1 - P_{m(m+1)})e^{-ik_{(m+1)x}h_{m+1}} & (1 + P_{m(m+1)})e^{ik_{(m+1)x}h_{m+1}} \end{bmatrix}.$$

(2.13)

We have defined $h_{m+1} = x_{m+1} - x_m$ and

$$P_{m(m+1)} = \frac{k_{(m+1)x}}{k_{mx}}.$$

(2.14)

The amplitudes of the incident and reflected waves are related to those amplitudes in the transmitted region $N+1$ by

$$\begin{bmatrix} E_0 \\ rE_0 \end{bmatrix} = M_{01} M_{12} M_{23} \cdots M_{N(N+1)} \begin{bmatrix} A_{N+1} \\ B_{N+1} \end{bmatrix}$$

$$= \begin{bmatrix} m_{11} & m_{12} \\ m_{21} & m_{22} \end{bmatrix} \begin{bmatrix} tE_0 \\ 0 \end{bmatrix},$$

(2.15)

where $B_{N+1} = 0$ since there is no incident wave in this region, as illustrated in Fig. 1.6. We can obtain the reflection coefficient of the multilayered medium by

$$r = \frac{m_{21}}{m_{11}}.$$

(2.16)

On the other hand, the transmission coefficient of the multilayered medium can be expressed by

$$t = \frac{1}{m_{11}}.$$

(2.17)

Therefore, the power reflectivity of the multilayered medium can be found by using

$$R = \left| r \right|^2 . \tag{2.18}$$

This theoretical calculation is useful for the investigation of multiple layer structures and microcavity.

$$R = \left| r \right|^2 .$$

Chapter 3 Nitride-based distributed Bragg reflectors

High-reflectivity nitride-based distributed Bragg reflectors (DBRs) are important for the development of GaN-based optical devices such as resonant-cavity light-emitting diodes (RCLEDs) [44] and vertical-cavity surface-emitting lasers (VCSELs) [45]. Recently, nitride-based microcavity structures have attracted much attention due to the investigation of fundamental phenomena including strong light-matter interaction, solid-state cavity quantum electrodynamics (CQED) [46], and dynamical Bose-Einstein condensates [23]. Therefore, the requirement of high-reflectivity nitride-based DBRs is necessary for these developments. In this chapter, we will first describe the difficulty in growth of nitride-based DBRs. Then, the experimental results based on AlN/GaN and AlN/AlGaN DBRs will be presented. Furthermore, the experimental reflectivity spectra are modeled by transfer matrix theory in order to compare the experimental and theoretical results.
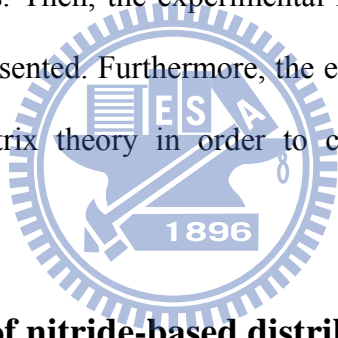
3.1 Difficulty in growth of nitride-based distributed Bragg reflector

The evolution of nitride-based materials and devices suffered many obstacles, such as the absence of lattice-matched substrates [47] and low activation ratio of p-type (Al)GaN [48]. Nevertheless, the most difficult challenge for wide-bandgap microcavities is the lattice-mismatched nitride-based DBRs since the microcavity structure consists of an active region embedded within two high-reflectivity DBRs. High-quality and high-reflectivity DBRs are necessary to achieve high cavity Q value for longer photon lifetime.

3.1.1 Lattice mismatch issue

The most difficult obstacle to the development of nitride-based DBRs is the large

lattice mismatch between the AlN and GaN. Contrary to the well-known AlAs/GaAs material system, the nitride-based compounds suffer from a large lattice mismatch of about 2.4% between AlN and GaN, as shown in Fig. 3.1, which causes a huge challenge for the growth of high-reflectivity nitride-based DBRs.
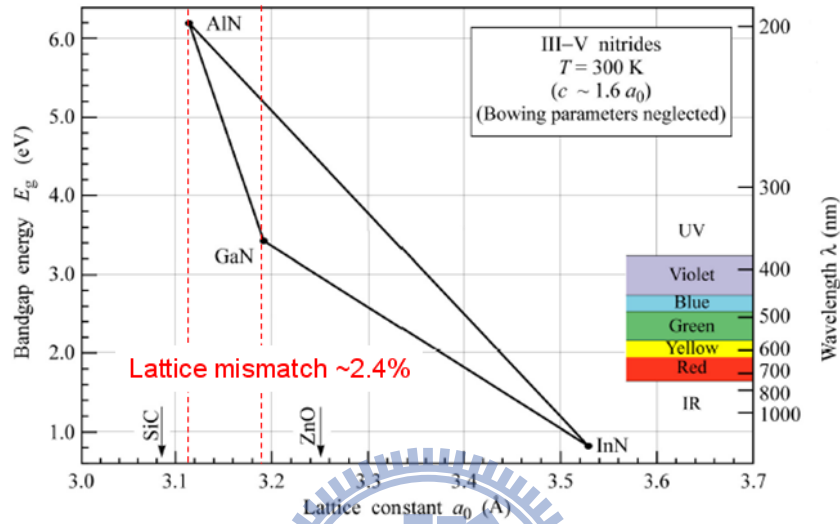
Fig. 3.1 The relation between bandgap energy (emission wavelength) and lattice constant for nitride-based alloy families. (After [49])

In general, there are three kinds of material systems used in nitride-based DBRs, including AlN/GaN, Al(Ga)N/(Al)GaN, and AlInN/GaN. The AlN/GaN DBRs offer the highest refractive index contrast among the III-nitride compounds and provide highly reflective structures together with a large stopband width. However, the large lattice mismatch between the AlN and GaN is up to 2.4%, which generally results in a tensile strain and the formation of cracks. These cracks tend to grow into V-shaped grooves and seriously affect the reflectivity of the DBR due to scattering, diffraction, and absorption. To prevent the formation of cracks, the $Al_xGa_{1-x}N/Al_yGa_{1-y}N$ system is usually used to reduce the strain in the whole DBR structure. Nevertheless, the refractive index contrast decreases with increasing Al composition in GaN or Ga composition in AlN, which leads to a reduced stopband width and the requirement of increased number of pairs to achieve high reflectivity. An alternative approach was proposed by Carlin and Ilegems

[50]. They demonstrated high-reflectivity AlInN/GaN DBRs which are nearly lattice matched to GaN. The 20-pair DBRs exhibited a peak reflectivity over 90% and a 35 nm stopband width at 515 nm. Although this kind of DBR has been reported, the growth of high-quality AlInN film is still difficult due to the composition inhomogeneity and phase separation in AlInN, which results from large mismatch of covalent bond length and growth temperature between InN and AlN [51]. The other approach to overcome the strain issue is to use the AlN/GaN superlattice [52].

3.1.2 Recent program in nitride-based DBRs

In spite of the difficulty in growing nitride-based DBRs, many research groups are still devoted to this topic. Several research results about AlGaN/GaN DBR structures have been reported in early 2000 [53], [54], [55]. However, it usually requires the growth of relatively thick DBRs in order to achieve the high peak reflectivity. Moreover, high-reflectivity ultraviolet DBRs based on AlGaN/AlGaN or AlGaN/AlN structures are reported recently [56], [57], [58], [59], [60]. Mitrofanov *et al.* demonstrated high-reflectivity crack-free 25-pair $Al_{0.18}Ga_{0.82}N/Al_{0.8}Ga_{0.2}N$ DBRs for the spectral region of about 350 nm grown by molecular-beam epitaxy (MBE). The maximum reflectivity is higher than 99% and the stopband width is about 26 nm [58]. As for the lattice-matched AlInN/AlGaN or AlInN/GaN DBRs, crack-free fully epitaxial nitride microcavity using AlInN/GaN DBRs with reflectivities close to 99% was reported by Carlin *et al.* in 2005 [61]. Their group also demonstrated crack-free lattice-matched ultraviolet AlInN/AlGaN DBRs, which exhibit a reflectivity higher than 99% at a wavelength as short as 340 nm and a stop-band width of 20 nm in 2006 [62]. Regarding the development of the AlN/GaN DBR structures, Ng *et al.* reported a 20.5-pair AlN/GaN DBR grown on sapphire substrate by MBE system in 1999 [63]. The peak reflectivity up to 95% was observed at a wavelength of 392.5 nm. In the next year, they

pushed the peak reflectivity up to 99% based on a 25.5-pair AlN/GaN DBR together with a stopband width of 45 nm [64]. Mastro *et al.* demonstrated 9-pair AlN/GaN DBRs on Si(111) substrates by MOCVD system [65]. The high index contrast at the AlN/Si interface enhanced the DBR reflectivity up to 96%. The related progress in the growth of highly reflective nitride-based DBR can be found in the review paper of Butté *et al.* [66].

3.2 Blue-violet AlN/GaN DBRs

In order to obtain high-reflectivity and large-stopband nitride-based DBRs, our approach is to focus on the study of growing high-quality AlN/GaN DBRs by MOCVD. In this section, we report the growth over 2 inch c-sapphire substrates of high-reflectivity AlN/GaN DBRs designed for the blue-violet spectral region. There are six DBR samples with different quarter-wavelength thicknesses for different spectral regions. The measured maximum peak reflectivity is about 97% and the stopband width is about 36 nm in the blue spectral region. The experimental reflectivity spectra are modeled by transfer matrix theory in order to compare the experimental and theoretical results. Furthermore, the effect of GaN absorption on reflectivity spectra and stopband width is investigated as well.

3.2.1 Growth of AlN/GaN DBRs

The AlN/GaN DBRs were grown on 2 inch c-sapphire substrates in a low-pressure high-speed rotating-disk MOCVD system (Veeco D75). During the growth, trimethylgallium (TMGa) and trimethylaluminum (TMAl) were used as group III source materials and ammonia (NH_3) as the group V source material. After thermal cleaning of the substrate in hydrogen ambient for 5 min at 1100 °C, a 30-nm-thick GaN nucleation layer was grown at 550 °C. The growth temperature was raised up to 1040

°C for the growth of 3 μm GaN buffer layer. The flow rate of TMGa was 89.5 μmol/min and the flow rate of NH$_3$ was 3.6 l/min. The growth rate of the 3 μm GaN buffer layer was kept ~ 2 μm/h. Then, the AlN/GaN DBRs were grown at 1000 °C under the fixed chamber pressure of 100 Torr. During the growth of GaN and AlN layers for the DBR structures, the flow rates of TMAl, TMGa, and NH$_3$ were 74.9 μmol/min, 71.6 μmol/min, and 1.2 l/min, respectively. Six 20-pair AlN/GaN DBR samples with different quarter-wavelength thicknesses were prepared and labeled DBRs I–VI. During the growth, we used *in-situ* monitoring reflectivity signals. By choosing the monitor wavelength to be the specific stopband center wavelength, the thickness of each quarter-wavelength GaN and AlN can be precisely controlled by following the reflectance signals during the MOCVD growth [22]. The surface morphology of the DBRs was studied by optical microscopy. The thicknesses of the total DBR structures were investigated by scanning electron microscopy (SEM). The reflectivity spectra of the AlN/GaN DBRs were measured by the n & k ultraviolet-visible spectrometer with normal incidence at RT. The PL emission spectra of the DBRs were measured at RT in order to study the crystal quality of GaN layers. The excitation light of PL is a 325-nm line of He–Cd laser and the PL emission is dispersed by a 0.32 m monochromator and detected with a photomultiplier with standard lock-in technique.

The designed center wavelengths of the DBRs I–VI are about 440, 417, 408, 392, 373, and 364 nm, respectively. Although it is well-known that the designed center wavelength of DBR VI will suffer the absorption of GaN layers, we will investigate the influence of GaN absorption on reflectivity and stopband width of the AlN/GaN DBRs. The total *in-situ* reflectance signal at 440 nm for the growth of DBR I is shown in Fig. 3.2. The reflectance signal of the general two-step process for the growth of GaN on sapphire is shown in Fig. 3.2 as well. After the growth of bulk GaN layer, it is obvious that the relative reflectivity is gradually saturated with increasing number of DBR pairs.

Therefore, the thicknesses of quarter-wavelength DBR layers can be controlled precisely by monitoring the real time reflectance signal and the growth rate can be estimated simultaneously. The growth rates of the AlN and GaN layers are about 0.6 and 2.3 Å/s, respectively.
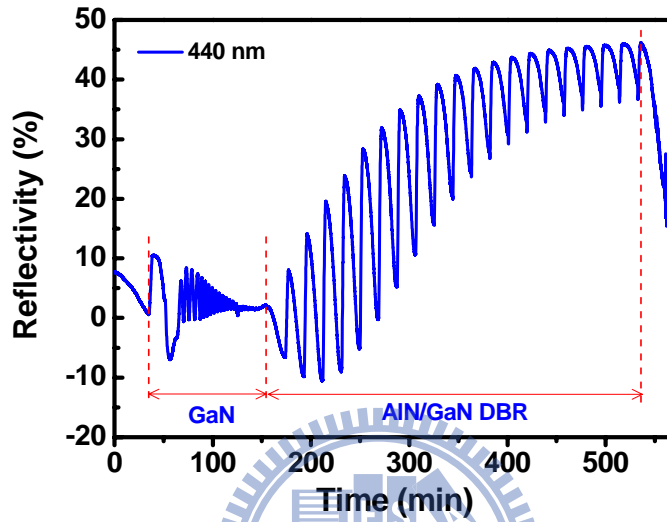
Fig. 3.2 Total *in-situ* reflectance signal at 440 nm for the growth of DBR I.

The cross-section SEM images of DBRs I–VI are shown in Fig. 3.3. The AlN/GaN interfaces are well defined and flat in all DBR samples. According to the SEM images, the total thicknesses of DBRs I–VI were measured to be about 2.058, 1.930, 1.876, 1.788, 1.678 and 1.624 μm, respectively. Therefore, the average bilayer thicknesses of 102.9 nm (DBR I), 96.5 nm (DBR II), 93.8 nm (DBR III), 89.4 nm (DBR IV), 83.9 nm (DBR V), and 81.2 nm (DBR VI) were estimated based on the SEM measurements. Since the bilayer thickness is about 80~100 nm, the cross-sectional SEM images can provide sufficient resolution for the estimation of bilayer thicknesses [56], [59], [61], [64]. Furthermore, by a combination of double crystal x-ray diffraction (XRD), growth rate calibrations, and SEM measurements, we can estimate the layer thicknesses of AlN and GaN, respectively. Table 3.1 shows the estimated layer thicknesses of GaN and AlN,

respectively, for DBRs I–VI.
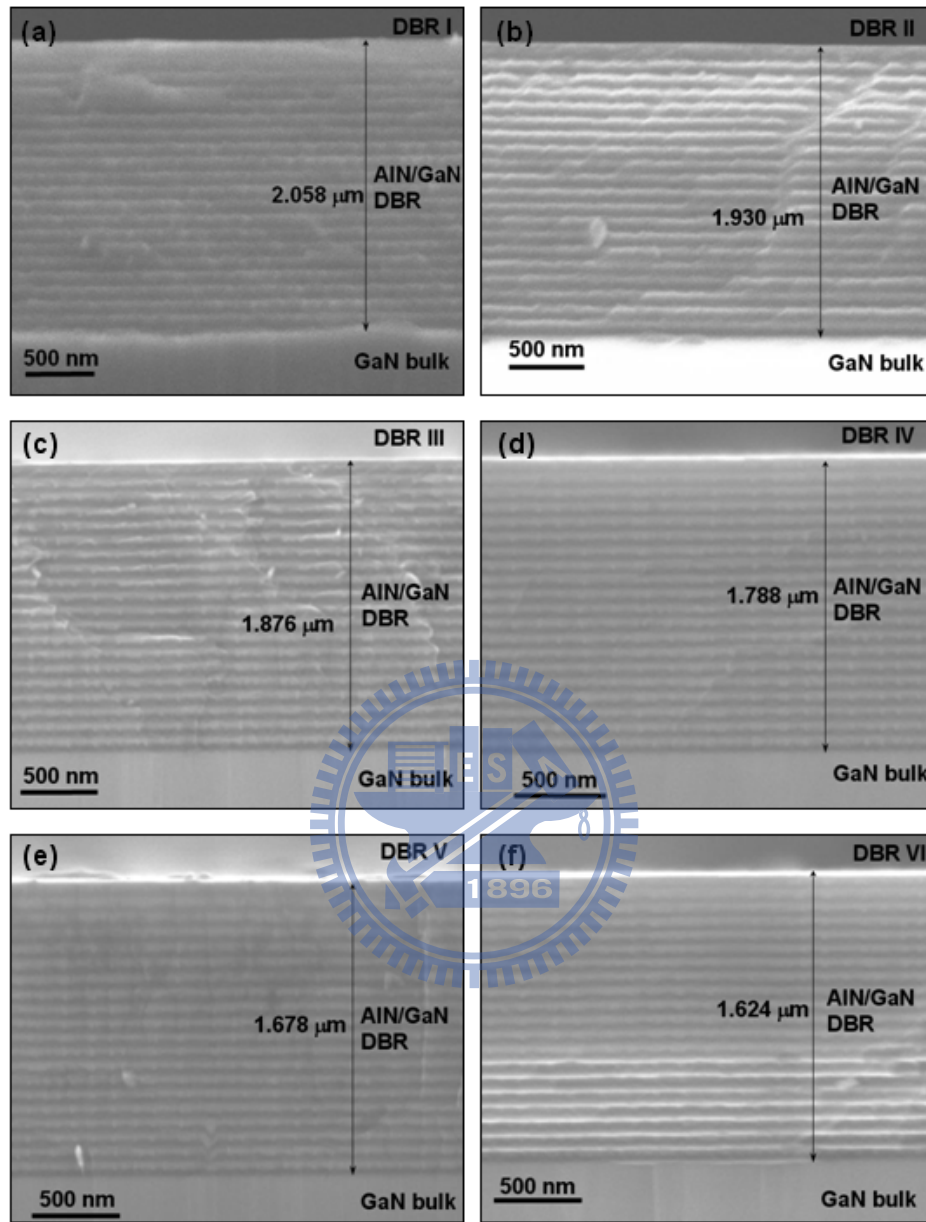
Fig. 3.3 Cross-section SEM images of (a) DBR I, (b) DBR II, (c) DBR III, (d) DBR IV, (e) DBR V, and (f) DBR VI.

Table 3.1. Estimated layer thicknesses of quarter-wavelength GaN and AlN for DBRs I–VI, respectively.

Sample	DBR I	DBR II	DBR III	DBR IV	DBR V	DBR VI
Bilayer thickness (nm)	102.9	96.5	93.8	89.4	83.9	81.2
GaN thickness (nm)	47.7	44.5	43.1	40.8	37.9	36.5
AlN thickness (nm)	55.2	52.0	50.7	48.6	46.0	44.7

3.2.2 Analysis of reflectance spectra

Fig. 3.4 shows the surface images of DBRs I–VI by an optical microscopy in order to compare the macroscopic morphology of DBR samples with different quarter-wavelength thicknesses. In Fig. 3.4, no evidence of cracks was observed in all DBR samples. Nevertheless, the surface images of DBRs IV–VI show smoother macroscopic morphology than that of DBRs I–III. Specifically, the surface morphology becomes rougher with increasing total thickness in DBR layers, which may originate from the increased tensile strain. Since DBR I has large total thickness, the accumulation of tensile strain is more severe than DBR VI and may result in various types of defects when the accumulation of tensile strain is relaxed. Although the AlN/GaN interfaces are well defined in all DBR samples, as shown in Fig. 3.3, the interfaces of DBRs I and II show relatively rougher than that of DBRs V and VI. This situation is consistent with the observation from optical microscopy.

Fig. 3.5 shows the measured (solid line) and simulated (dashed line) reflectivity spectra of DBRs I–VI. In Fig. 3.5(a), experimental measurement shows that the peak reflectivity of DBR I at 440 nm is about 97.2% and the stopband width is 36.6 nm. To compare experimental and calculated reflectivity spectra, theoretical simulation based on transfer matrix theory was performed using the layer thicknesses listed in Table 3.1 for DBRs I–VI. The refractive index dispersion and the extinction coefficient of the GaN layer were taken from the measured data based on a bulk GaN grown on sapphire substrate. As for the parameters of the AlN layer, since the wavelength range considered here is far away from the bandgap of AlN, we only took the refractive index dispersion into account and ignored the extinction coefficient in our simulation. The corresponding parameters can be found in Refs. [67], [68]. The calculated reflectivity spectra of DBRs I–VI are also shown in Fig. 3.5. By comparing the measured and calculated results, the

characteristics of simulated reflectivity spectrum of DBR I including stopband width and the phase of the short- and long-wavelength oscillations are in good agreement with the measured spectrum, as shown in Fig. 3.5(a).
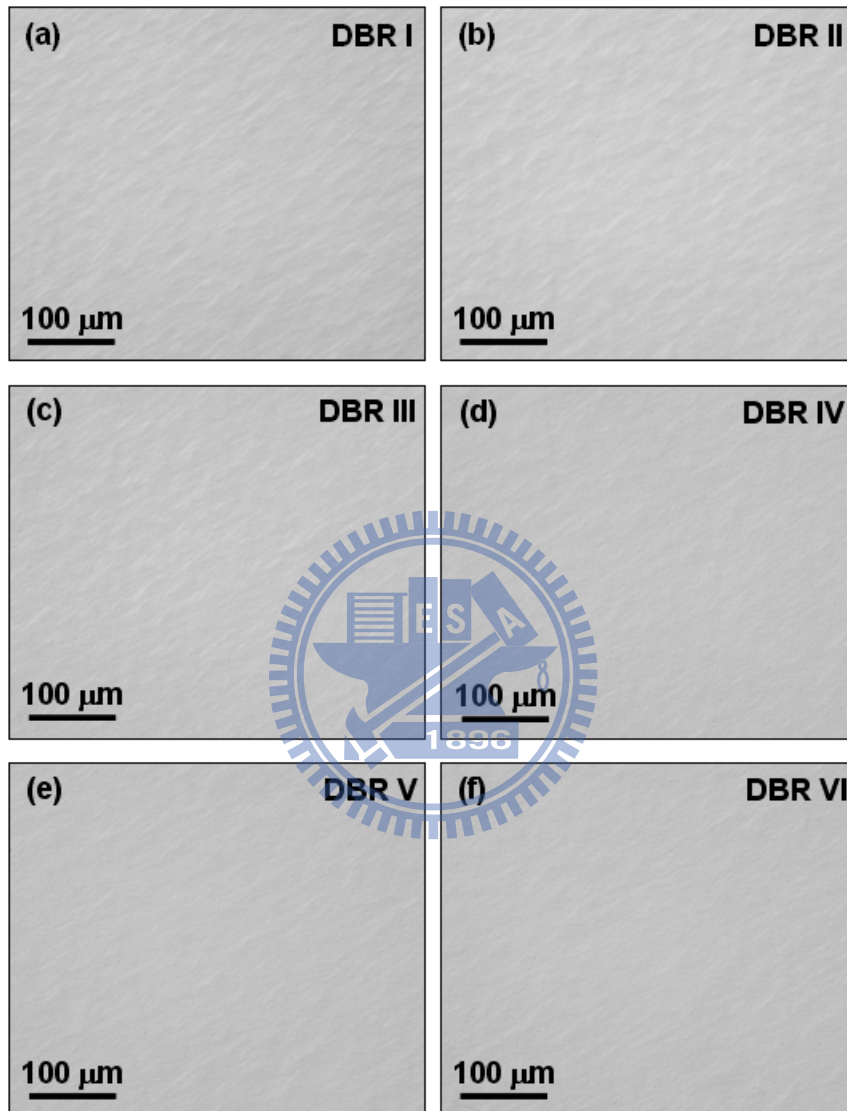
Fig. 3.4 Optical microscope images of (a) DBR I, (b) DBR II, (c) DBR III, (d) DBR IV, (e) DBR V, and (f) DBR VI.

The calculated peak reflectivity and stopband width are about 98.2% and 43.5 nm, respectively. These calculated values are larger than the measured results, which may come from the degradation of crystal quality in the samples and the structural imperfections such as the deviations from the designed layer thickness and interface

roughness between each epitaxial layer. Moreover, the mismatch between the measured and calculated reflectivity spectra in the short wavelength interference fringes is due to the absorption in the GaN layers because it is difficult to perfectly consider the scattering loss and absorption of the bilayers in our simulation. Additionally, the calculated reflectivity spectrum of DBR VI deviates obviously from the measured result, as shown in Fig. 3.5(f).
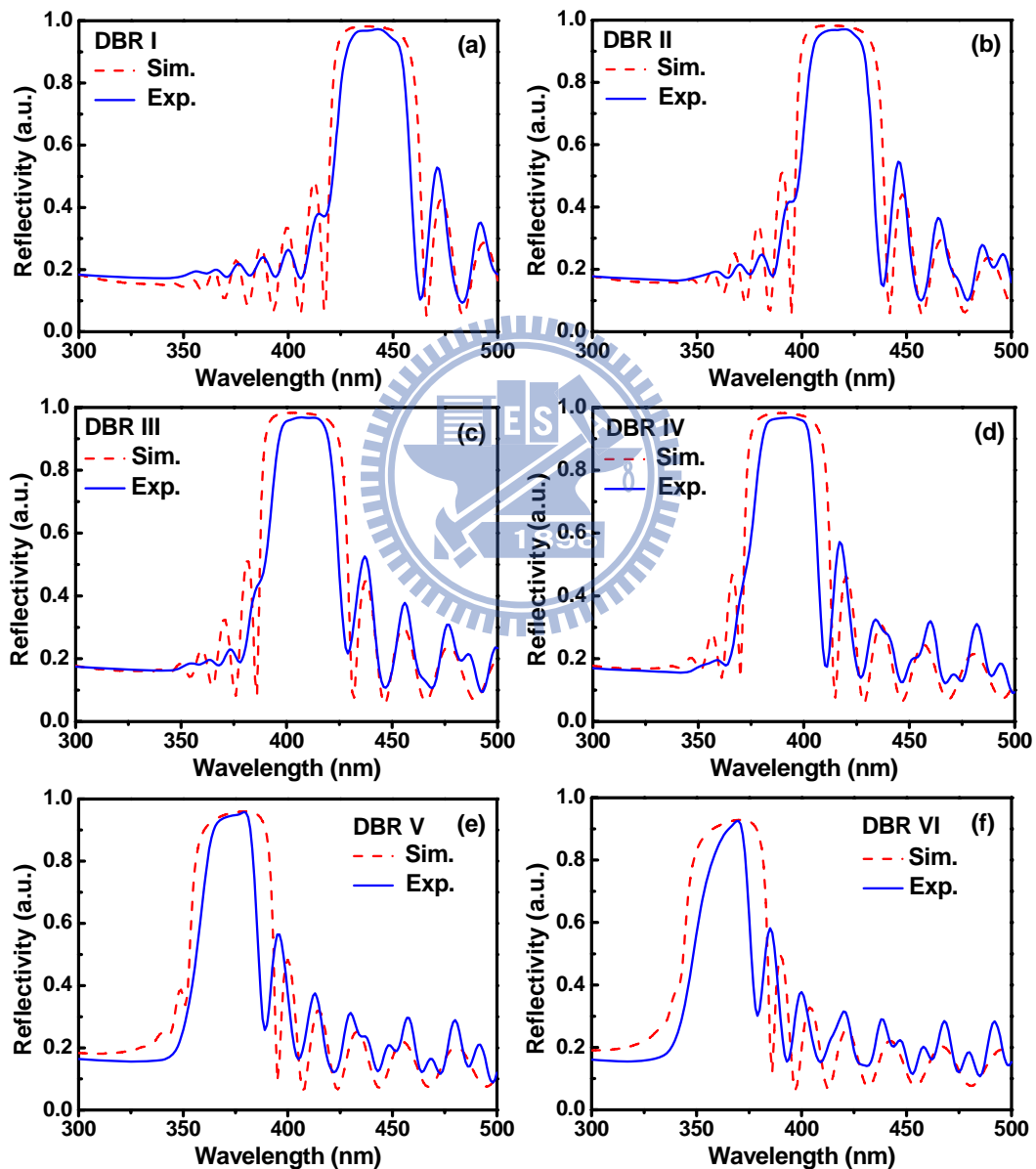
Fig. 3.5 Measured (solid) and simulated (dashed) reflectivity spectra of (a) DBR I, (b) DBR II, (c) DBR III, (d) DBR IV, (e) DBR V, and (f) DBR VI.

Since the stopband of DBR VI is centered at a shorter wavelength than tha GaN bandgap (~363 nm), the absorption from GaN layers will play a more important role in the case of DBR VI. Although the extinction coefficient of a bulk GaN was taken into account in our calculation, the effects of strain and defects in the GaN layers of DBRs will modify the original absorption in a bulk GaN. Similarly, the measured short wavelength interference fringes in Figs. 3.5(c)–(e) are not resolved as compared with the simulation results. Consequently, according to the difference between the measured and calculated reflectivity spectra the effect of GaN absorption in the AlN/GaN DBRs is larger than that in a bulk GaN layer. Furthermore, the measured and calculated maximum reflectivity values and stopband widths of the DBRs I–VI are summarized in Fig. 3.6. The GaN absorption significantly influences the reflectivity and stopband width when the designed DBR wavelength is shorter than about 380 nm.
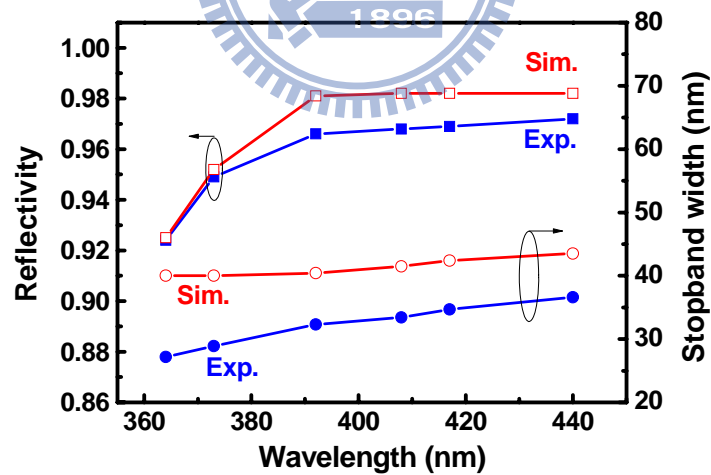
Fig. 3.6 Measured and calculated maximum reflectivity values and stopband widths of the DBRs I–VI.

In order to further observe the difference of crystal quality between tha GaN layers in DBRs and bulk GaN layers, the RT PL spectra of DBR VI and a bulk GaN grown on sapphire were measured and plotted in Fig. 3.7. We deduced that the PL spectrum of

DBR VI mainly originates from the emission of GaN layers in DBR structures. Since the DBR samples were pumped by 325 nm laser from the top surface, the laser light will be fully absorbed by the GaN layers in DBRs before reaching the GaN buffer layer. Therefore, the emission from GaN buffer layer could not be observed in the PL spectra.
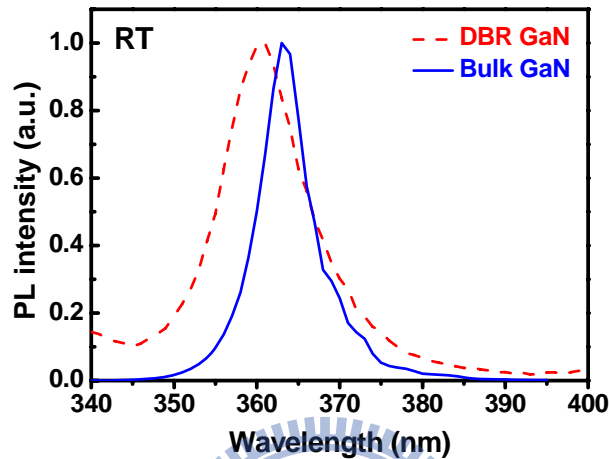
Fig. 3.7 RT PL spectra of DBR VI and a bulk GaN grown on sapphire substrate.

In Fig. 3.7, the emission peak from GaN layers in DBR VI is about 360.7 nm, which is obviously below the emission peak of bulk GaN layer (~363.3 nm). This difference could be induced by the condition of GaN layers grown on partially relaxed AlN layers. Under this circumstance, the GaN layer will suffer compressive strain and have larger bandgap energy than that of bulk GaN layer. Furthermore, by comparing the PL spectra of DBR VI and bulk GaN layer, it is notable that the PL spectrum of DBR VI is obviously broader than that of bulk GaN. The full-width at half-maximum (FWHM) values of the PL spectra measured on DBR VI and bulk GaN are 11.5 and 6.4 nm, respectively. The broader PL spectrum of DBR VI mainly originates from the effects of strain, defects, and dislocations, which will result in inhomogeneous strain distribution in DBR structures and induce different band edge emission energies [69]. As a consequence, the tail of the PL emission spectrum related to the GaN layers in DBR VI would be broader than that in bulk GaN.

3.3 Ultraviolet AlN/AlGaN DBRs

As far as nitride-based microcavities designed for the study of strong coupling phenomena are concerned, the active regions made of GaN bulk or GaN/AlGaN multiple quantum wells are preferred due to the relatively narrow PL linewidth as compared with InGaN/GaN multiple-qautnum wells (MQWs). Therefore, high-quality nitride-based ultraviolet DBRs with a wavelength around 360 nm at the center of the stop band are essential approach to fabricate nitride-based microcavities for the study of strong exciton-photon coupling. In general, ultraviolet nitride-based DBRs consist of AlInN/AlGaN or AlGaN/AlGaN material system. Especially, for devices containing pure GaN as an active medium, the ultraviolet DBRs can not employ GaN as the layer materials because of the strong increase of optical absorption below 360 nm. In this section, we report the growth on 2 inch c-sapphire substrates of high-reflectivity AlN/AlGaN DBRs designed for the ultraviolet spectral region. The structures are grown by MOCVD and consist of $AlN/Al_{0.23}Ga_{0.77}N$ system to increase the difference of refractive index in the DBR structures. The measured peak reflectivity values are 90% and 97% for 20-pair and 34-pair AlN/AlGaN DBRs, respectively. Furthermore, the experimental reflectivity spectra are modeled by transfer matrix theory in order to compare the experimental and theoretical results.

3.3.1 Growth of ultraviolet AlN/AlGaN DBRs

The AlN/AlGaN DBRs were grown in a low-pressure high-speed rotating-disk MOCVD system. Two-inch diameter (0001)-oriented sapphire substrates were used for the growth of DBR samples. During the growth, TMGa and TMAl were used as group III source materials and NH_3 as the group V source material. After thermal cleaning of the substrate in hydrogen ambient for 5 min at 1100 °C, a 30-nm-thick GaN nucleation

layer was grown at 500 °C. The growth temperature was raised up to 1020 °C for the growth of 2.8 μm GaN buffer layer. Then, the AlN/AlGaN DBRs were grown under the fixed chamber pressure of 1.33×10^4 Pa similar to the previous reported growth conditions [52]. Two DBR samples with different numbers of periods were prepared. The sample labeled DBR A consists of 20-pair AlN/$Al_{0.23}Ga_{0.77}N$ quarter-wavelength layers. The other sample labeled DBR B consists of 34-pair AlN/$Al_{0.23}Ga_{0.77}N$ quarter-wavelength layers. By employing *in situ* optical reflectivity system, the growth rate of the AlN and AlGaN layer can be estimated to be about 0.7 and 2.2 Å/s, respectively. The surface morphology of the DBRs was studied by optical microscopy and atomic force microscopy (AFM). The thicknesses of the total DBR structures were investigated by SEM. The reflectivity spectra of the AlN/AlGaN DBRs were measured by the n & k ultraviolet-visible spectrometer with normal incidence at RT [70], [71], [72].
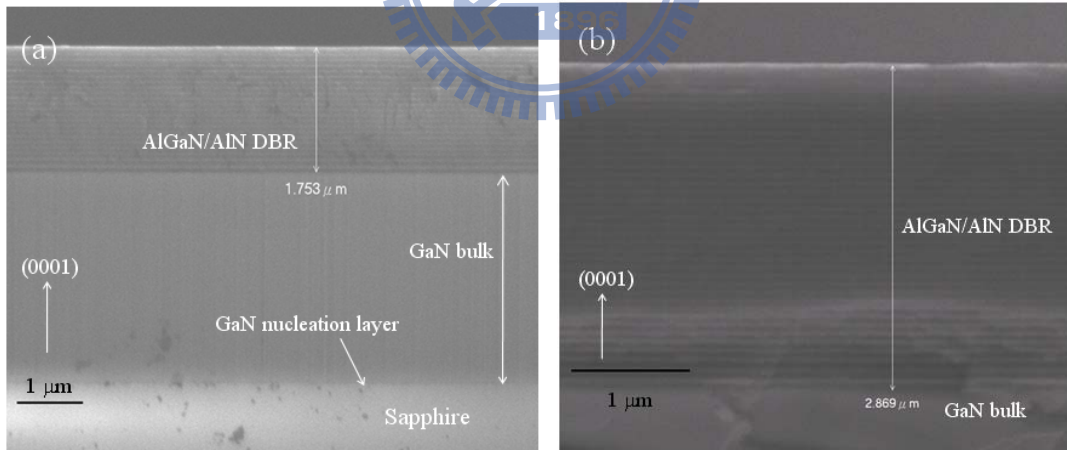
Fig. 3.8 (a) Cross-sectional SEM image of DBR A. The total thickness of 20-pair AlN/$Al_{0.23}Ga_{0.77}N$ DBR is about 1.753 μm. (b) Cross-sectional SEM image of DBR B. The total thickness of 34-pair AlN/$Al_{0.23}Ga_{0.77}N$ DBR is about 2.869 μm.

The PL emission spectra of the DBRs were measured at room temperature in order to study the crystal quality. The excitation source is a 266 nm radiation from a frequency tripled Ti:sapphire laser and the PL emission is dispersed by a 0.55 m

monochromator and detected with a photomultiplier with standard lock-in technique. The laser beam is focused by an optical objective lens and the focused laser spot size is about 50 μm together with the power density about 3×10^3 W/cm^2. The cross-section SEM images of DBRs A and B are shown in Fig. 3.8. The AlN/AlGaN interfaces are well defined and flat. According to the SEM images, the total thicknesses of 20-pair and 34-pair AlN/Al$_{0.23}$Ga$_{0.77}$N DBRs were measured to be about 1.753 and 2.869 μm, respectively. Therefore, the average bilayer thicknesses of 87.6 nm (DBR A) and 84.4 nm (DBR B) were estimated based on the SEM measurements. Since the bilayer thickness is about 80~90 nm, the cross-sectional SEM images can provide sufficient resolution for the estimation of bilayer thicknesses [56], [59], [61], [64]. Furthermore, by a combination of double crystal x-ray diffraction (XRD), growth rate calibrations, and SEM measurements, we can estimate the layer thicknesses of AlN and AlGaN, respectively. For DBR A, we estimate the layer thicknesses of 45.5 nm for AlN layer and 42.1 nm for Al$_{0.23}$Ga$_{0.77}$N layer. In the case of DBR B, the thicknesses of AlN and Al$_{0.23}$Ga$_{0.77}$N layers are about 44.1 and 40.3 nm, respectively. Moreover, the GaN nucleation layer and GaN buffer layer can be clearly observed in Fig. 3.8(a).

3.3.2 Analysis of reflectance spectra

Fig. 3.9 shows the surface images of DBR A and DBR B taken by an optical microscopy in order to compare the macroscopic morphology between DBRs A and B. The surface image of DBR A shows a smooth macroscopic morphology but that of DBR B shows a rough one. Besides, no evidence of cracks was observed in DBR A, as shown in Fig. 3.9(a). As for the DBR B, cracks were observed from the optical microscope image. We further estimated the mean distance between cracks of DBR B at about 300 μm.
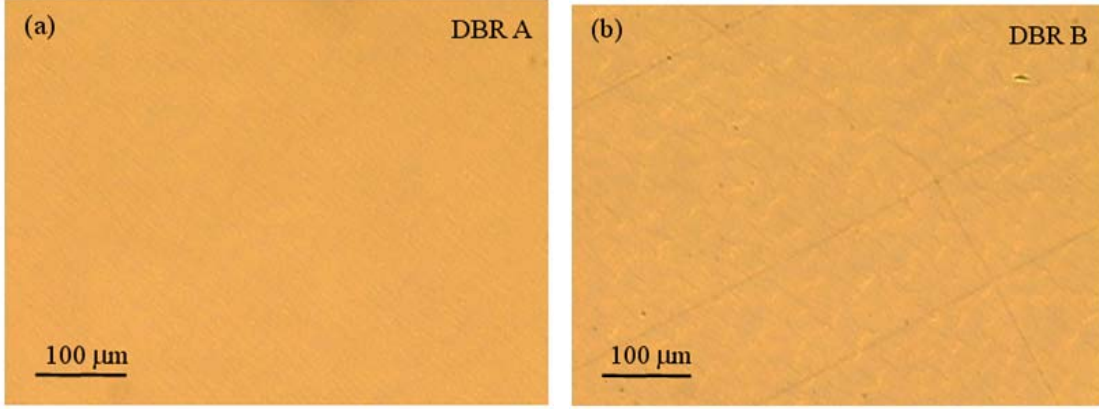
Fig. 3.9 Optical microscope images of (a) DBR A and (b) DBR B.

Fig. 3.10 shows the measured (solid line) and simulated (dashed line) reflectivity spectra of DBR A and DBR B. In Fig. 3.10(a), experimental measurement shows that the peak reflectivity at 367 nm is about 90% and the stop-band width is 24 nm. To compare the experimental and calculated reflectivity spectra, theoretical simulation based on transfer matrix theory was performed using above layer thicknesses. As for the parameter of refractive index, Adachi model is employed to calculate the refractive index values of GaN, AlN, and $Al_{0.23}Ga_{0.77}N$ layers. The Adachi model can be expressed by [73]

$$n(h\nu) = \sqrt{a(x)\left(\frac{h\nu}{E_g}\right)^{-2}\left[2-\sqrt{1+\left(\frac{h\nu}{E_g}\right)}-\sqrt{1-\left(\frac{h\nu}{E_g}\right)}\right]+b(x)} \,, \qquad (3.1)$$

where E_g is the band gap of the material, ν is the frequency of the incident light, h is Planck's constant, and $a(x)$ and $b(x)$ are composition-dependent fitting parameters. This equation showed good agreement with measurements on GaN, AlN, and InN for the transparency region [74]. In our calculation, we employed the fitting parameters for AlN layer from Brunner et al. [67]. As for the $Al_{0.23}Ga_{0.77}N$ layer, the fitting parameters are more reliable from Laws et al. when the aluminum composition is smaller than 0.38 [68]. Fig. 3.10(a) also shows the calculated reflectivity spectrum of DBR A. By

comparing the measured and calculated results, the characteristics of simulated reflectivity spectrum of DBR A including stop-band width and the phase of the long wavelength oscillations are in good agreement with the measured spectrum. Nevertheless, the calculated peak reflectivity is about 94%, which is larger than the measured result. This difference may come from dislocations in the samples and the structural imperfections such as deviations from the designed layer thickness and interface roughness between each epitaxial layer. Moreover, the mismatch between the measured and calculated reflectivity spectra in the short wavelength interference fringes is due to absorption in the $Al_{0.23}Ga_{0.77}N$ layers because the scattering loss and absorption in the bilayers were not taken into account in the simulation. In the case of DBR B, the experimental measurement shows that the peak reflectivity at 358 nm is about 97% and the stop-band width is 16 nm, as shown in Fig. 3.10(b). Theoretical calculation expects that the peak reflectivity and stop-band width of the 34-pair $AlN/Al_{0.23}Ga_{0.77}N$ DBRs should be 99.8% and 20 nm, respectively. Partial cracks were observed in DBR B from optical microscopy, which results from the release of the strain energy due to the large number of DBR pairs. Therefore, this difference between measured and calculated reflectivity spectra of DBR B may come from crack-induced dislocations and the degradation of crystal quality [75], [76]. In addition, the short wavelength interference fringes are not resolved for DBR B. Since the stop band of DBR B is centered at a shorter wavelength than that of DBR A, the absorption effects from AlGaN layers will play a more important role in the case of DBR B as the AlGaN layers have the same aluminum composition in both samples.
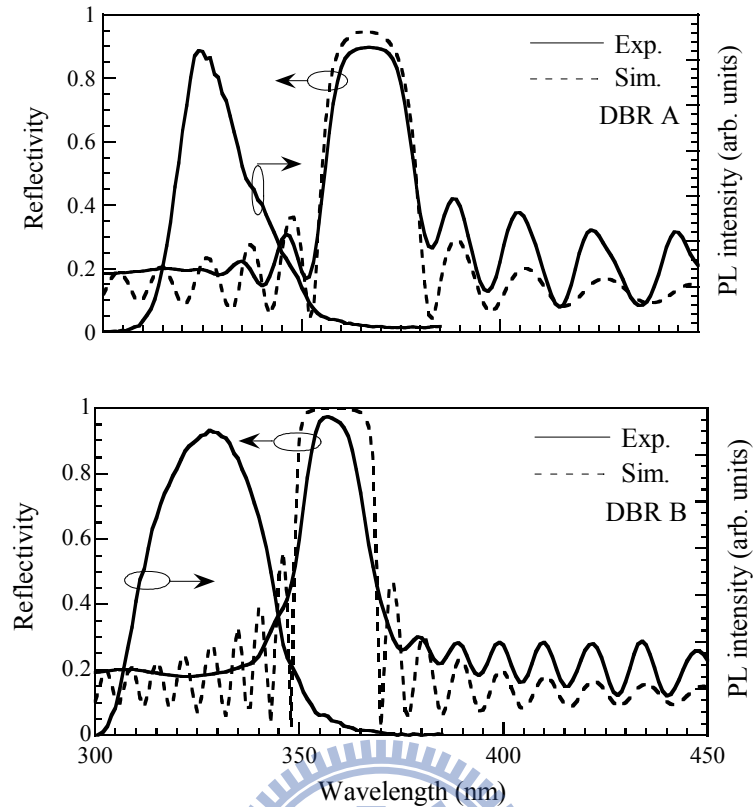
Fig. 3.10 (a) Measured (solid) and simulated (dashed) reflectivity spectra of DBR A at a peak wavelength of 367 nm. The room-temperature PL spectrum shows an emission peak at 323 nm from the $Al_{0.23}Ga_{0.77}N$ layers. (b) Measured (solid) and simulated (dashed) reflectivity spectra of DBR B at a peak wavelength of 358 nm. The room-temperature PL spectrum shows an emission peak at 327 nm.

In order to further observe the crystal quality and estimate the alloy compositions simultaneously, the room-temperature PL spectra of these two DBR samples were measured and also plotted in Fig. 3.10. The PL spectra mainly originate from the emission of AlGaN layer in DBR structures. Since the DBR samples were pumped by 266 nm laser from the top surface, the laser light will be fully absorbed by the AlGaN layers before reaching the GaN buffer layer. Therefore, the emission from GaN buffer layer can not be observed in the PL spectra. In Fig. 3.10(a), the emission peak from $Al_{0.23}Ga_{0.77}N$ layer of DBR A is about 323 nm, which is obviously below the DBR stop-band wavelength range. This condition is important to keep the stop-band width in

order to avoid the absorption of $Al_{0.23}Ga_{0.77}N$ layer [56]. Moreover, the emission peak from $Al_{0.23}Ga_{0.77}N$ layer of DBR B is about 327 nm, as shown in Fig. 3.10(b). By comparing Figs. 3.10(a) and 3.10(b), it is notable that the PL spectrum of DBR B is obviously broader than that of DBR A. The FWHM values of the PL spectra measured on DBRs A and B are 20.4 and 32.8 nm, respectively. Therefore, according to the broader emission spectrum and the observable cracks on sample surface, we deduce that the broader PL spectrum mainly originates from the generation of cracks, which could result in strain inhomogeneity due to the local strain depending on the distance to a crack in a cracked sample. The inhomogeneous strain distribution results in different band edge emission energy [69]. As a consequence, the tail of the emission spectrum related to the AlGaN layers in DBR B would be broader than that in DBR A. The difference of the PL emission peak between the DBRs A and B also arises from this factor since the growth conditions of the $Al_{0.23}Ga_{0.77}N$ layers in DBR A and DBR B are the same.
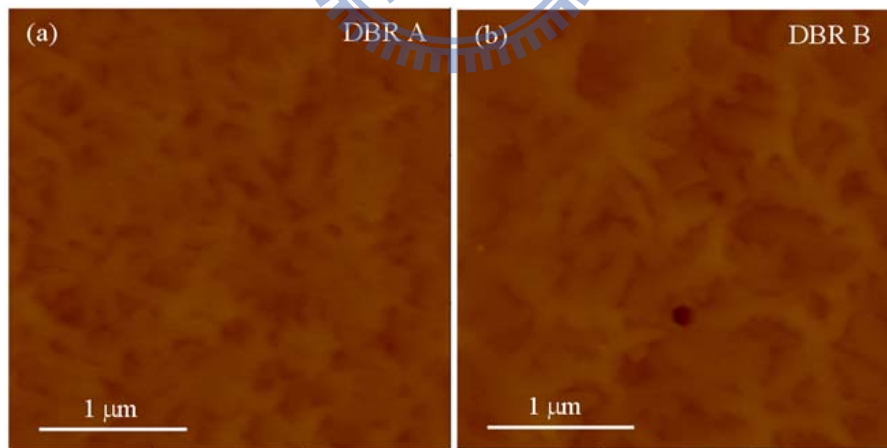
Fig. 3.11 AFM images (3 μm×3 μm) of (a) DBR A and (b) DBR B.

The surface morphology of the DBR samples is investigated by AFM measurement. Figs. 3.11(a) and 3.11(b) are AFM images of DBRs A and B, respectively. The scanning area is 3×3 $μm^2$. It is found that the roughness of 34-pair DBR (rms = 1.7 nm) is larger

than that of 20-pair DBR (rms = 1.3 nm) within the scanning area. This larger surface roughness of DBR B may also result from the degradation of crystal quality. Rough surface morphology will lead to high optical scattering loss, which is also one of the factors leading to the mismatch of the calculated and measured reflectivity spectra.

3.4 Summary

In summary, we have studied the blue-violet DBRs consisting of 20-pair AlN/GaN multilayers grown on sapphires by MOCVD system. The maximum reflectivity and stopband width of 20-pair AlN/GaN DBR at 440 nm are 97.2% and 36.6 nm, respectively. The simulation results show that the calculated reflectivity spectra deviate from the measured results with decreasing designed DBR wavelength due to the significant GaN absorption. RT PL measurement shows that the degradation of GaN crystal quality in DBR structures is more serious than that of bulk GaN, which will significantly affect the reflectivity and stopband width of the AlN/GaN DBRs when the designed DBR wavelength is near GaN bandgap. Furthermore, the ultraviolet DBRs consisting of $AlN/Al_{0.23}Ga_{0.77}N$ multilayers were grown by MOCVD system. The reflectivity and stop-band width of 20-pair $AlN/Al_{0.23}Ga_{0.77}N$ DBR are 90% and 24 nm, respectively. The simulated reflectivity spectrum is in good agreement with measured result. When the number of DBR pairs increases from 20 to 34 pairs, partial cracks are observed from optical microscopy due to the release of the strain energy. Despite the crystal quality problem, the peak reflectivity of 34-pair $AlN/Al_{0.23}Ga_{0.77}N$ DBR can still achieve 97% at a wavelength of 358 nm together with a stop-band width of 16 nm. These results will be useful for the further fabrication of wide-bandgap semiconductor microcavities.

Chapter 4 ZnO-based microcavities in strong coupling regime

As mentioned in section 1.3.3, ZnO-based microcavity is a promising wide-bandgap material because of its large oscillator strength and exciton binding energy (~60 meV in the bulk layer). In order to further study the optical properties of ZnO-based microcavity polaritons, growth of high-quality ZnO films and fabrication of high-Q ZnO microcavities are necessary. Furthermore, the knowledge of the polariton dispersion curves from ZnO-based microcavities at RT is crucial for the advanced design of polariton-based optoelectronic devices operating at high working temperature. In this chapter, we demonstrated the experimental observation of strong coupling regime in bulk ZnO-based hybrid microcavities at RT according to the angle-resolved reflectivity spectra. The investigated structure consists of a $3\lambda/2$ bulk ZnO cavity layer sandwiched between two high-reflectivity DBRs and has a cavity quality factor (Q) about 250. Furthermore, the measured angle-resolved reflectivity spectra are theoretically investigated by employing transfer matrix method and the influence of exciton scattering states is also taken into account in our calculations to compare the experimental and theoretical results.

4.1 Sample preparation

The present hybrid microcavity structure consists of a bulk ZnO $3\lambda/2$ thick cavity sandwiched between a bottom 30-pair AlN/Al$_{0.23}$Ga$_{0.77}$N DBR and a top 9-pair dielectric SiO$_2$/HfO$_2$ DBR. The AlN/AlGaN DBR was grown by MOCVD on a 3 μm thick GaN buffer layer on c-plane sapphire substrate. During the growth, TMGa and TMAl were used as group III source materials and NH$_3$ as the group V source material. After thermal cleaning of the substrate in hydrogen ambient for 5 min at 1100 °C, a 30-nm-thick GaN nucleation layer was grown at 520 °C. The growth temperature was

raised up to 1040 °C for the growth of 3 μm GaN buffer layer. Then, the AlN/AlGaN

DBRs were grown under the fixed chamber pressure of 100 Torr similar to the previous

reported growth conditions. The bulk ZnO 3λ/2 thick cavity was grown on AlN/AlGaN

DBR by pulsed-laser deposition (PLD) system, which is commonly adopted for the

growth of ZnO epi-films [77]. The beam of a KrF excimer laser (λ = 248 nm) was

focused to produce an energy density ~5–7 J·cm^{-2} at a repetition rate 10 Hz on a

commercial hot-pressed stoichiometric ZnO (99.999 % purity) target. The ZnO films

were deposited with a growth rate ~0.5475 Å s^{-1} at a substrate temperature of 600 °C

and a working pressure ~ 9.8× 10^{-8} Torr without oxygen gas flow. Finally, the 9-period

SiO$_2$/HfO$_2$ dielectric DBR was deposited by dual electron-beam gun evaporation system

to complete the microcavity structure.
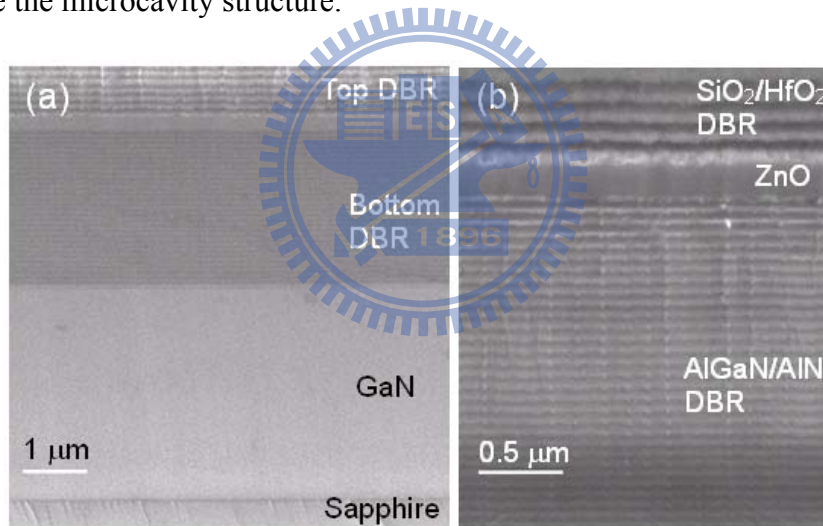
Fig. 4.1 (a) Low-magnification cross-section scanning electron microscopy image
of the 3λ/2 bulk ZnO hybrid microcavity structure. (b) Cross-section scanning
electron microscopy image of the AlGaN/AlN and SiO$_2$/HfO$_2$ DBRs, and the 3λ/2
ZnO bulk layer under high magnification.

The low-magnification SEM image of the ZnO hybrid microcavity structure is

shown in Fig. 4.1(a). Fig. 4.1(b) shows the cross-section SEM image of the AlGaN/AlN

and SiO$_2$/HfO$_2$ DBRs, and ZnO bulk layer under high magnification. The interfaces

between each layer are well defined. To further illustrate the configuration of the hybrid

microcavity structure, the refractive index profile and the optical-field intensity in the growth direction for normal incidence at photon energy of 3.23 eV are displayed in Fig. 4.2.
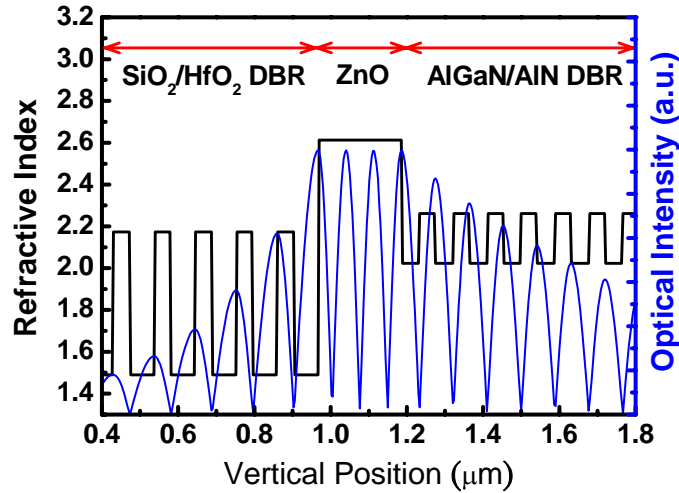
Fig. 4.2 Refractive index profile and the optical-field intensity in the growth direction for normal incidence at photon energy of 3.23 eV.

RT μPL spectra were performed under normal incidence by focusing the laser beam using an UV microscope objective (15×) which makes the laser spot size about 3 μm. The emission light from sample surface was collected along the normal direction by a 600 μm core UV optical fiber. The excitation source of the PL measurements is a 266 nm radiation from a frequency tripled Ti:sapphire laser. RT angle-resolved reflectivity measurements were carried out by using a two arm goniometer and a xenon lamp was employed as a white light source combined with a 100 μm core optical fiber. The reflected light was then collected by a 600 μm core UV optical fiber mounted on a rotating stage with an angular resolution of ~1° and detected by a liquid nitrogen cooled charge-coupled device (CCD) attached to a 320 mm single monochromator with a spectral resolution of about 0.2 nm.

4.2 Basic optical properties

The optical properties of the $3\lambda/2$ ZnO film grown on the 30-pair AlN/AlGaN DBR were investigated by performing RT PL measurements, as shown in Fig. 4.3(a). The half-cavity structure exhibited strong near-band-edge emission around 378 nm (3.28 eV), which has been known to be of free excitonic nature [78], [79], [80]. Additionally, the green PL mainly comes from the deep-level emission which is related to the crystal defects, such as oxygen vacancies and zinc interstitials in the films as reported by Vanheusden *et al* [81]. The good material quality of the ZnO film can be observed from the suppression of the deep level emission band in the RT PL spectrum [32]. Another feature of the PL spectrum is the long tail extending from the near-band-edge emission. This property is usually observed from RT PL spectra of ZnO films [82] and caused by band structure deformation due to the crystal lattice deformation. Moreover, it is noteworthy that the growth of $3\lambda/2$ cavity length, which is relatively thicker than $\lambda/2$ or λ cavity is employed in this study since the ZnO crystal quality and optical properties can be effectively improved by increasing the film thickness [83]. In order to investigate the optical quality of the full ZnO microcavity structure, the RT μ-PL measurements were performed at normal incidence and the corresponding PL spectrum is shown in Fig. 4.3(b). The emission peak energy of the full ZnO microcavity is about 3.232 eV ($\lambda \sim 383.6$ nm), which means that the emission peak is nearly a pure cavity photon mode because of the large negative detuning between cavity photon energy at zero in-plane wave vector and exciton energy ($\Delta = E_{ph} - E_{ex}$). Under this circumstance, we can estimate the intrinsic cavity quality factor with the minimum perturbation of the exciton-photon coupling. From Fig. 4.3(b), the PL linewidth is only 13 meV ($\Delta\lambda \sim 1.53$ nm) due to the microcavity effect. Therefore, the cavity quality factor Q ($= \lambda/\Delta\lambda$) is about 250 based on the μ-PL measurement results.

Such a *Q* value is the state of the art for ZnO-based microcavities and demonstrates the high local quality of our ZnO microcavity structures. Moreover, another relatively week PL emission peak was observed at 413 nm in Fig. 4.3(b). This emission originates from the Bragg leaky modes of the top SiO$_2$/HfO$_2$ DBR structure.
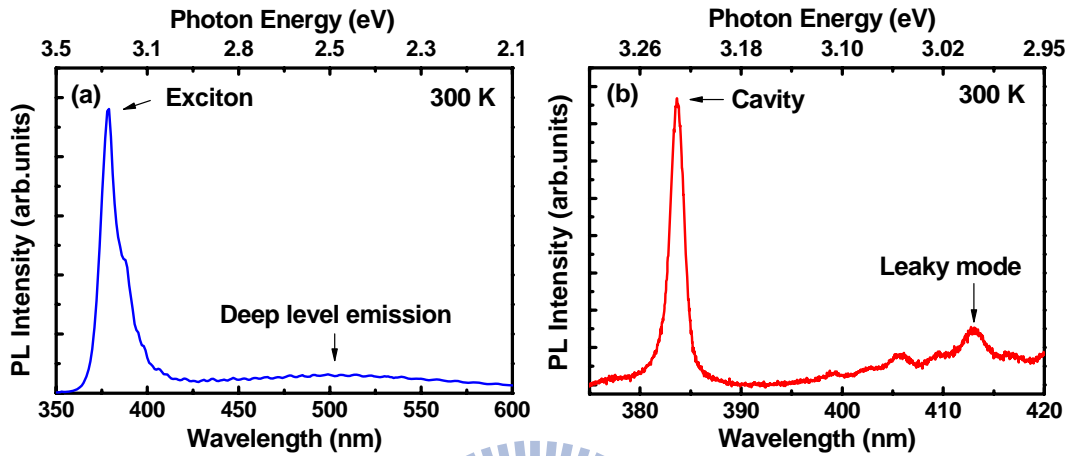
Fig. 4.3 (a) RT PL spectrum of the ZnO film grown on 30-pair AlN/AlGaN DBR. The half-cavity structure exhibited strong near-band-edge emission around 378 nm (3.28 eV). (b) RT normal incidence *μ*PL spectrum of the full ZnO hybrid microcavity structure. The emission peak energy is nearly pure cavity photon mode because of the large negative exciton-photon detuning.
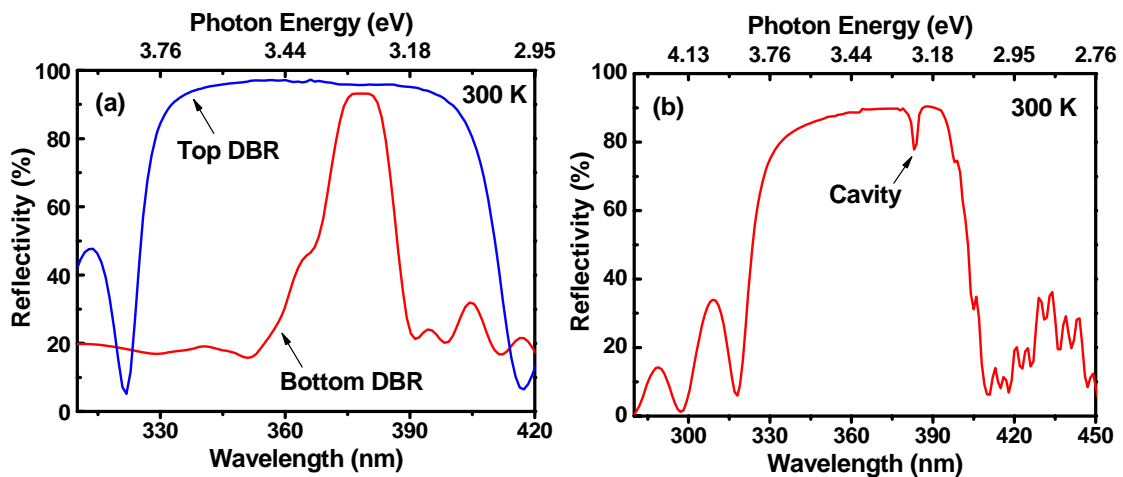
Fig. 4.4 (a) The RT reflectivity spectra of a 30-pair AlN/Al$_{0.23}$Ga$_{0.77}$N DBR and a 9-pair SiO$_2$/HfO$_2$ DBR. (b) RT normal incidence reflectivity spectrum of the full ZnO microcavity structure.

The reflectivity spectra of the 30-pair AlN/Al$_{0.23}$Ga$_{0.77}$N DBR and the 9-pair SiO$_2$/HfO$_2$ DBR were measured at RT at normal incidence, as shown in Fig. 4.4(a). The peak reflectivity of bottom AlN/AlGaN DBR is about 93% and the stop band width is about 145 meV. As for the top SiO$_2$/HfO$_2$ DBR, the peak reflectivity and the stop band width are 97% and 790 meV, respectively. Fig. 4.4(b) shows the RT normal incidence reflectivity spectrum of the full ZnO microcavity structure. The cavity dip can be clearly observed in the reflectivity spectrum, which shows a precise alignment between the DBR stop band and the ZnO cavity thickness. Although the measurement of the reflectivity spectrum was performed by using an optical lens to focus the incident while light beam, which results in a relatively larger spot size, the cavity dip (~ 383.4 nm) is consistent with the μ-PL measurement results. Nevertheless, the microscopic fluctuation in thickness, interface roughness, and crystal imperfection will cause the inhomogeneous broadening of the cavity mode when we use the incident while light beam with a larger spot size (~50 μm in diameter). As a result, a relatively lower Q factor of 196 was extracted from the reflectivity spectrum shown in Fig. 4.4(b) as compared with that from the μ-PL measurement. Furthermore, the irregular long wavelength oscillations of the reflectivity spectrum arise from the modulation of the respective top and bottom DBR spectra. On the contrary, the short wavelength oscillator is relatively regular, which only results from the top dielectric DBR since the short-wavelength light is absorbed by AlGaN layers in the bottom nitride-based DBR structure.

4.3 Observation of strong coupling regime at room temperature

To further probe the characteristics of strong exciton-photon coupling in the ZnO microcavity structure, RT angle-resolved reflectivity measurements were performed for the observation of in-plane polariton dispersion curves. The color map of the angular

dispersion of measured reflectivity spectra from 8° to 38° is shown in Fig. 4.5(a). Furthermore, the color maps of the calculated angle-resolved reflectivity spectra without and with taking the resonant exciton into account are shown in Figs. 4.5(b) and 4.5(c), respectively. The dashed white lines represent the calculated dispersion curves including exciton mode (*X*), cavity mode (*C*), LPB, and UPB. In our simulation, the reflectivity spectra were carried out based on transfer matrix method and the resonant exciton was modeled by a Lorentz oscillator dispersive dielectric function, as described in section 2.3.1. Originally, the pure in-plane cavity dispersion will take a parabolic form with the increase of in-plane wave vector. Nevertheless, the in-plane dispersion of polaritons depends on the dispersion of photons and the degree of the mixing with excitons. By comparing Figs. 4.5(a) and 4.5(b), the pure cavity mode follows the parabolic dispersion, which is consistent with the Bragg mode (BM) from the low energy side of the stop band. Nevertheless, the measured dispersion of the LPB obviously deviates from the parabolic cavity mode and approaches to exciton mode with increasing angle. Furthermore, a good agreement is found between the experimental and theoretical LPBs, as shown in Figs. 4.5(a) and 4.5(c), when we consider the strong exciton-photon coupling in our calculation by assigning the parameter *B* related to the oscillator strength of about 10^5 meV^2. This value is nearly two times more than that of GaN-based materials due to the larger oscillator strength of ZnO materials [25], [39], [40]. In addition, this value is also in good agreement with the recently published value [41]. As can be seen from Fig. 4.5(c), we estimated that the anticrossing occurs near the angle of about 34° and the corresponding vacuum Rabi splitting value is about 72 meV. This large vacuum Rabi splitting may originate from the high cavity quality factor, good ZnO crystal quality, and larger ZnO thickness. On the other hand, although the angular dispersion of the LPB is well visible from experimental results, the signature of the UPB is nearly not observable, as shown in Fig. 4.5(a). This interesting issue regarding

the anticrossing behavior in bulk ZnO microcavities was investigated by Faure *et al.* in 2008. They theoretically expected that the anticrossing behavior can be properly defined in bulk GaAs and GaN microcavities (i.e., the upper and lower polariton branches can be probed by experimental measurements), whereas only the LPB is a well-defined and well-mixed exciton-photon state in bulk ZnO microcavities [84]. They proposed that the UPB in bulk ZnO microcavities is strongly damped due to the absorption by scattering states of excitons.
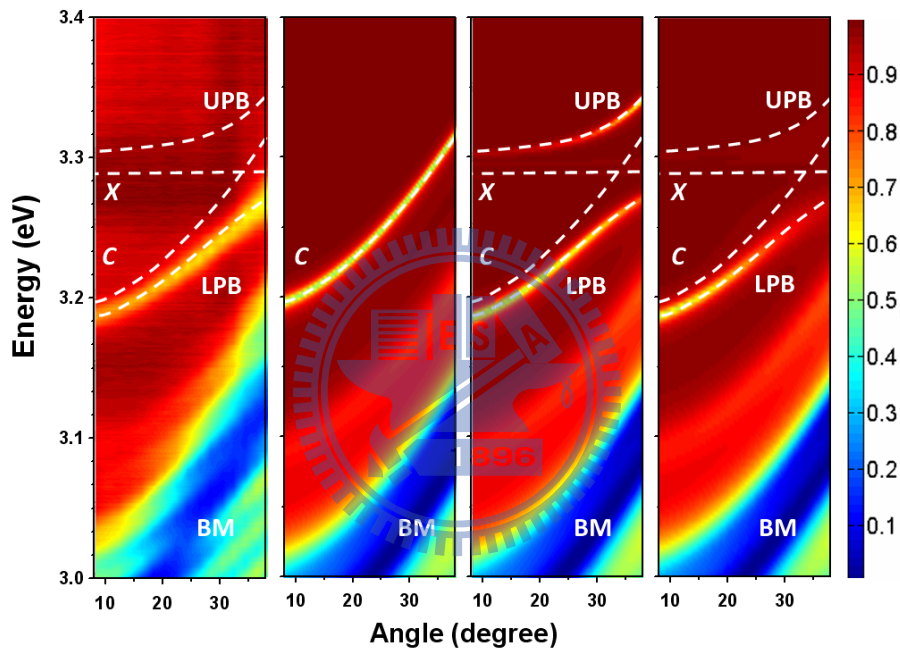
Fig. 4.5 (a) Color map of the angular dispersion of measured reflectivity spectra from 8 to 38° at RT. (b) Color maps of the calculated angle-resolved reflectivity spectra without taking the resonant exciton into account. (c) Color maps of the calculated angle-resolved reflectivity spectra with taking the resonant exciton into account. (d) Simulation of angle-resolved reflectivity spectra for the bulk ZnO microcavities after taking the absorption continuum into account.

In order to understand the origin of invisible UPB in bulk ZnO microcavities, we further take into account the effect of absorption induced by scattering states of excitons in our simulation [84]. The 3D exciton physical model is used in our calculation to involve the absorption of bound states and scattering states, which can be described as

[43]

$$\alpha(\hbar\omega) = \frac{A_0}{2\pi^2 R_y a_0^3} \left[4\sum \frac{\gamma/n^3}{\left(\chi + 1/n^2\right)^2 + \gamma^2} + \int \frac{d\chi'}{\pi} \frac{\gamma S_{3D}(\chi')\sqrt{\chi'}}{\left(\chi - \chi'\right)^2 + \gamma^2} \right], \qquad (4.1)$$

where R_y is the exciton Rydberg energy, a_0 is the exciton Bohr radius, γ is the half-linewidth normalized by Rydberg, χ is a normalized energy $(\hbar\omega - E_g)/R_y$, and S_{3D} is called the Sommerfeld enhancement factor

$$S_{3D}(\chi) = \frac{2\pi/\sqrt{\chi}}{1 - e^{-2\pi/\sqrt{\chi}}}. \qquad (4.2)$$

The corresponding parameters were extracted from the recent literature [84]. The absorption due to scattering states is added into the dielectric function and the amplitude is adjusted to match the experimental absorption spectra [85].

Fig. 4.5(d) presents the simulation of angle-resolved reflectivity spectra for the bulk ZnO microcavities after taking the scattering absorption into account. It is clearly observed that the UPB is significantly broadened due to its crossing with the scattering states of excitons. In wide bandgap semiconductor-based microcavities, the vacuum Rabi splitting energy is nearly the same or larger than the exciton binding energies, especially for ZnO-based microcavities. In this case, it will give rise to the energy overlap between the UPB and the scattering states, which may originate from the exciton excited states, the onset of continuum absorption, and the exciton-phonon complexes [31], [41], [86]. Such a situation is especially important for bulk ZnO microcavities due to the relatively thick cavity layer and the large absorption coefficient ($\sim 2\times10^5$ cm^{-1}) for ZnO materials [84]. These effects induce the damping of the coherence for upper polariton states and lead to the dispersion of UPB to be invisible.
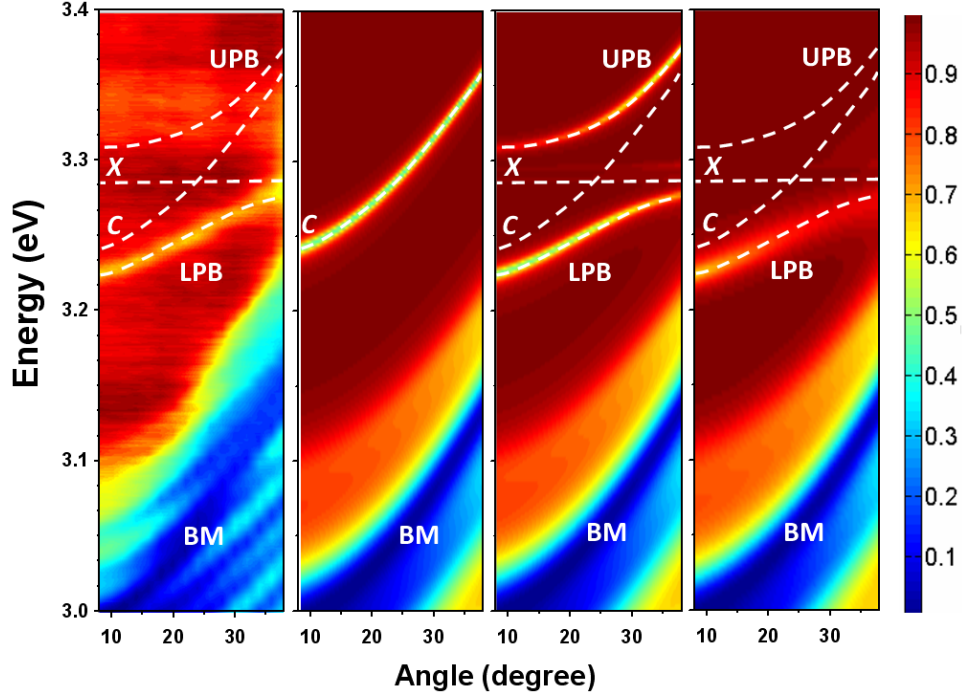
Fig. 4.6 (a) Color map of the measured angle-resolved reflectivity spectra of the ZnO microcavity with smaller exciton-cavity detuning. (b) Simulation of angle-resolved reflectivity spectra for the pure cavity mode of the ZnO microcavity with smaller exciton-cavity detuning. (c) Simulation of angle-resolved reflectivity spectra for the polariton modes of the ZnO microcavity with smaller exciton-cavity detuning. (d) Calculated angle-resolved reflectivity spectra including the continuum absorption for the ZnO microcavity with smaller exciton-cavity detuning.

To further confirm our experimental results and get further insight into the significant influence of the scattering states, we prepared a ZnO microcavity with relatively thinner cavity thickness, i.e., smaller exciton-cavity detuning. Fig. 4.6(a) shows the color map of the measured angle-resolved reflectivity spectra of the ZnO microcavity with smaller detuning. Similar situations including non-parabolic LPB and invisible UPB are observed in Fig. 4.6(a). The simulation of angle-resolved reflectivity spectra for the pure cavity mode and the polariton modes are shown in Figs. 4.6(a) and 4.6(b), respectively. Based on identical simulation parameters, the calculated LPB is also in good agreement with the measured results. An identical vacuum Rabi splitting

value is obtained at the resonant angle of about 24°. Moreover, the calculated angle-resolved reflectivity spectra including the scattering absorption is plotted in Fig. 4.6(d), which is also in good agreement with measured results. By comparing Figs. 4.5(a) and 4.6(a), the different exciton-polariton dispersion curves due to different detuning values can be obviously observed. Consequently, the evidence for exciton-photon strong coupling in bulk ZnO microcavities at RT is confirmed by the observation of the lower polariton dispersion curves from two different detuning values. Although the full anticrossing behavior cannot be experimentally demonstrated because of the strong scattering absorption, it should be noted that clear observation of the LPB is more important for the investigation of Bose-Einstein condensation and polariton lasing. Prospects regarding the experimental observation of the complete anticrossing behavior may be achieved based on a ZnO/ZnMgO quantum-well microcavity due to the decrease in the thickness of ZnO absorption and the enhancement of exciton binding energies, pushing the scattering states of exciton to higher energy values due to the 2D excitonic nature from the quantum confinement effect [87], [88].

4.4 Summary

In summary, we have presented the growth and characterization of bulk ZnO-based hybrid microcavities which consists of 30-pair epitaxially grown AlN/AlGaN DBR on the bottom side of the $3\lambda/2$ thick ZnO cavity and 9-pair SiO_2/HfO_2 DBR as the top mirror. The strong exciton-photon coupling at RT has been demonstrated according to the excellent agreement between experimental and theoretical angle-resolved reflectivity spectra. The large vacuum Rabi splitting of the order of 72 meV is achieved in the ZnO microcavities with two different cavity-exciton detuning values. Furthermore, it is found that the UPB could not be experimentally probed in the thick bulk ZnO microcavities since the Rabi splitting energy is larger than the exciton binding

energy, pushing the UPB into the energies of scattering absorption. Nevertheless, it is noteworthy that the clear observation of the LPB is more significant for the realization of polariton-based optoelectronic devices for ZnO-based semiconductor microcavities.

Chapter 5 Comparison of strong coupling regimes in bulk GaAs, GaN, and ZnO microcavities

The strong coupling regime has been widely studied in the domain of atomic physics [7]. The physical mechanism of strong coupling for an atom in an optical cavity is relatively simpler than that for excitons in a semiconductor microcavity since it does not involve the strong relaxation phenomena observed in a solid state system. Therefore, the two eigenstates of upper polariton and lower polariton are identical in amplitude and linewidth for the case of an atom in a high-finesse cavity. On the contrary, for exciton resonances in a semiconductor microcavity, there can be interactions between polaritons and excited states of excitons. Additionally, the exciton continuum states may have a large impact on the polariton eigenstates when the Rabi splitting is equal to or larger than the exaction binding energy in the strong coupling regime [84]. Specifically, the absorption resulting from the continuum states causes broadening of the upper polariton state and leads to blurred polariton dispersion curves. To well define the existence of the strong coupling regime in semiconductor microcavities, the simultaneous appearance of LPB and UPB is one of the strong evidences from the view point of experimental measurements. For this reason, the possible impacts on the visibility of UPB should be further discussed. In this chapter, we intend to compare the behaviors of UPB and the optical spectra for bulk GaAs-, GaN-, and ZnO-based microcavities. We employ the approaches based on transfer matrix method and improved Lorentz oscillator model, including exciton continuum absorption and exciton inhomogeneous broadening to analyze the specialties of reflectivity spectra for these three materials. The appropriate designs of the active layer thickness and the exciton-photon detuning are investigated in order to suppress the absorption of exciton scattering states for UPB. In addition, we

also point out that the exciton inhomogeneous broadening plays an important role for the visibility of UPB particularly in current wide-bandgap semiconductor microcavities. In the last part of this paper, we investigate whether the coherence of UPB is still damped by exciton continuum states in multiple-quantum-well-based ZnO microcavities. These calculation results shall be valuable for the comparison with experimental results in GaAs-, GaN-, and ZnO-based microcavities.

5.1 Broadening of upper polariton branch

A typical cavity-polariton dispersion curves in the case of negative detuning (i.e., the exciton energy is larger than cavity photon energy at zero in-plane wave vector) is shown in Fig. 5.1. The cavity-polariton dispersion exhibits LPB and UPB. When the energy of UPB is higher than the band edge of bulk active layer (the horizontal green dashed line) with increasing in-plane wave vector, the exciton continuum states would broaden the UPB in the energy range indicated by the blue dashed lines. There are three important parameters determining the relationship between UPB and exciton continuum states: the Rabi splitting (Ω), the effective Rydberg energy of excitons (Ry) or exciton binding energy, and the exciton-photon detuning (δ). When the Rabi splitting value is of the same order or larger than the effective Rydberg energy, the UPB will be pushed up to the energies of the exciton scattering states, and then upper polaritons scatter with exciton scattering states, which leads to the strong damping of the upper polaritons. Furthermore, it is relatively easy to cause the UPB to cross with the exciton continuum states in the condition of large positive exciton-photon detuning. Therefore, these above-mentioned internal physical mechanisms will have different importance depending on the structure design and active layer materials.
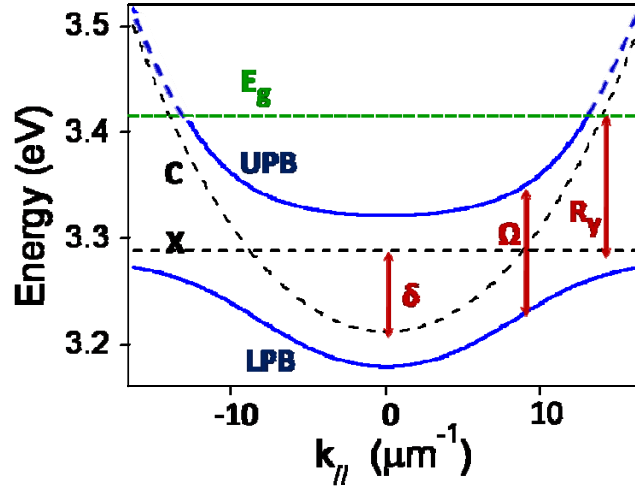
Fig. 5.1 (a) Typical polariton dispersion inclusive of upper polariton branch (UPB) and lower polariton branch (LPB) represented by blue lines. The pure cavity mode *C*, exciton mode *X* (black dashed line) and band edge E_g are shown (green dashed line). These symbols δ, Ω, and R_y represent exciton-photon detuning, Rabi splitting, and Rydberg energy.

For simplicity, the microcavity structures are composed of the same dielectric SiO_2/HfO_2 Bragg mirrors, and the active layer is based on the bulk GaAs, GaN, or ZnO. In addition, it is noteworthy that there are two compensating layers symmetrically on the both sides of the active layer, as shown in Fig. 5.2(a). These two layers are added in the optical cavity to satisfy the cavity thickness of $m\lambda/2$, where *m* is the number of cavity mode. Based on this design structure, we can obtain the mapping of the reflectivity spectra of microcavities with continuous variable active layer thicknesses. We have to emphasize that the two compensating layers are not taken into account in strong light-matter interaction. Fig. 5.2(b) shows the refractive index profile and the optical-field intensity in the vertical direction. Moreover, the number of DBR layers is adjusted to keep the cavity quality factor the same for the pure cavity mode.
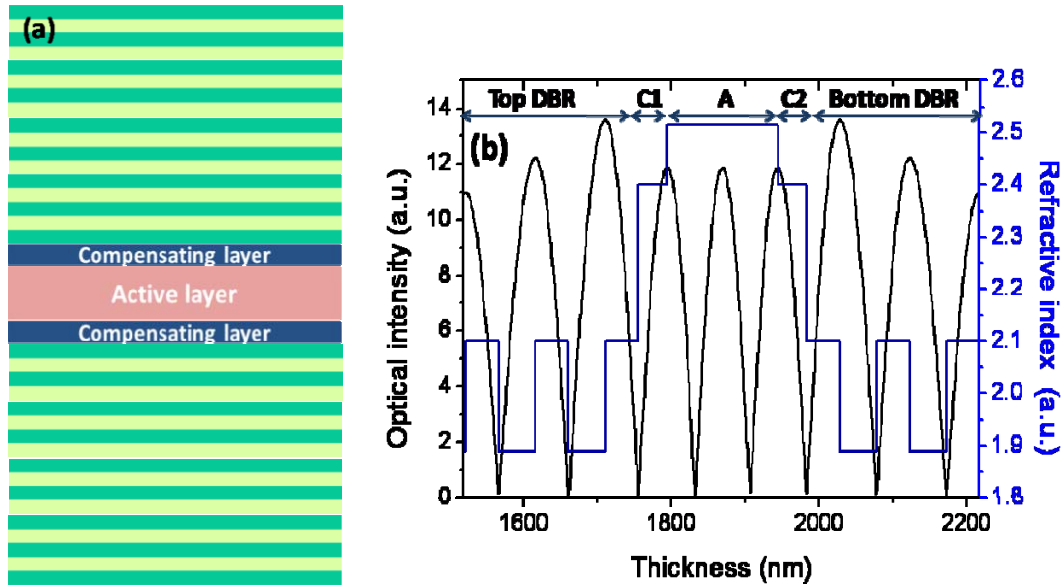
Fig. 5.2 (a) Schematic diagram of the bulk semiconductor microcavity. (b) Refractive index profile and the optical-field intensity in the vertical direction of the microcavity structure. A and C1(C2) represent the active layer and compensating layer, respectively.

In the calculation, we only considered the excitonic transition from fundamental state (1s) based on the assumption of probing the polariton properties of wide-bandgap materials (GaN and ZnO) at RT. In addition, the oscillator strength of ns excited states is inversely proportional to n^3 [89], with n being the principle quantum number. Therefore, the excited states contribute only minor interaction with cavity photon modes. On the other hand, since excitons in GaAs are unstable and hardly exist at RT, we employed the relevant parameters obtained from the experimental measurements at cryogenic temperature for GaAs material [90]. The linewidths of exciton resonances are characterized by the same homogeneous broadening of 1 meV in the three materials in order to clear the specificities and differences. The similar results are obtained for larger homogeneous broadening (~15 meV).

The reflectivity spectra of the microcavities for three materials were calculated based on transfer matrix method and the resonant exciton was modeled by a Lorentz

oscillator dispersive dielectric function. Besides, in order to take the exciton continuum states into account, the 3D exciton physical model is used in our calculation to involve the absorption of bound states and scattering states, which can be found in equations (4.1) and (4.2). The corresponding parameters of the three materials were extracted from the literatures [29], [85], [91], [92], [93], [94] and summarized in Table 5.1. By employing the 3D exciton model, we can define the scattering absorption including continuum states and excitonic absorption. The calculated results for the three materials are consistent with the absorption spectra reported by Refs. [92], [93].

Table 5.1. Relevant parameters of GaAs, GaN, and ZnO microcavities.

	GaAs	GaN	ZnO
Refractive index	3.57	2.73	2.52
Exciton transition energy	1.515 eV	3.477 eV	3.286 eV
Rydberg	4.1 meV	26.6 meV	59 meV
$\alpha(E_g)$	1.0×10^4 cm^{-1}	1.1×10^5 cm^{-1}	2.0×10^5 cm^{-1}
Bohr radius	13 nm	3.1 nm	1.8 nm

5.2 Influence of active layer thickness

In bulk semiconductor microcavities system, the Rabi-splitting is strongly dependent on the thickness of cavity layer since the whole cavity can be referred to as the active material. Therefore, it is expected that the Rabi-splitting will increase with the thickness of the cavity layer due to the increased overlap between matter and confined photons [91]. Generally, the Rabi splitting in a semiconductor microcavity can be described by [95]

$$\Omega = 2\sqrt{\omega_0 \omega_{LT}(d/L_{eff})} \,, \tag{5.1}$$

where ω_0 is the exciton resonance energy, ω_{LT} the effective longitudinal-transverse splitting, d the active layer thickness, and L_{eff} the effective cavity thickness involving the

optical field penetration in DBRs. An increase in Rabi splitting is obtained with increasing the active layer thickness of bulk cavity due to the larger ratio d/L_{eff} [90].
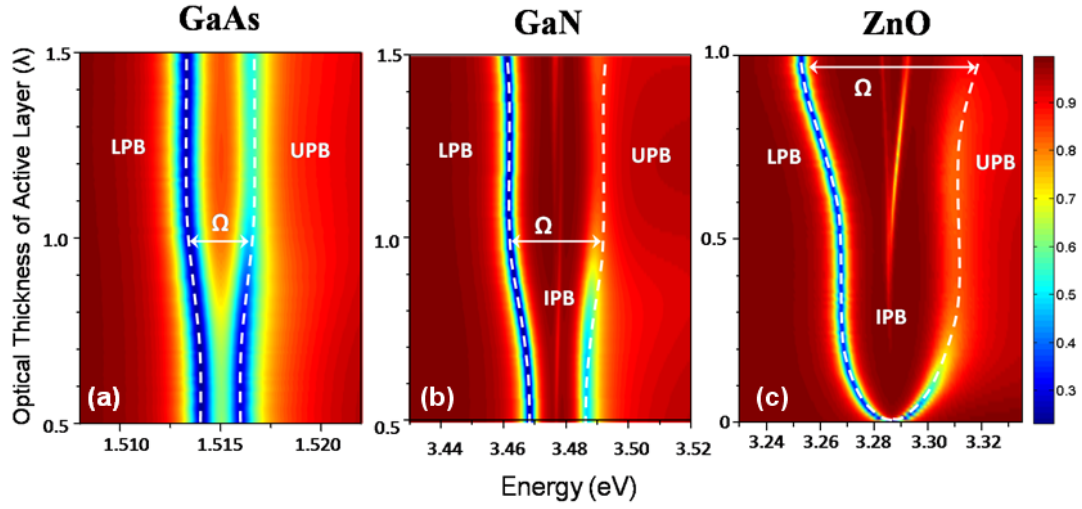
Fig. 5.3 Color maps of calculated reflectivity spectra as a function of active layer thickness for (a) GaAs, (b) GaN, and (c) ZnO microcavities at zero detuning and normal incidences. The whit dashed lines show the UPB and LPB without considering exciton continuum absorption.

Fig. 5.3 presents the color maps of reflectivity spectra as a function of the active layer thickness for GaAs, GaN, and ZnO microcavities. The reflectivity spectra were calculated in the condition of zero detuning and normal incidence ($k_{//}$ = 0). The calculated Rabi splitting values for the three microcavities with optical thickness of 1λ are listed in Table 5.2. In Fig. 5.3, it is apparent that there are two main branches, the UPB and LPB, for these three microcavity structures and the Rabi splitting becomes larger with increasing active layer thickness. It is worthy to mention that the Rabi splitting near the 0.5-λ optical thickness of active layer shows approximately constant (i.e., the UPB and LPB are nearly parallel), which originates from the small increase in the exciton-photon interaction due to the node of the optical field in the microcavity structure. In the GaAs-based microcavities, since the Rabi spitting is comparable to the effective Rydberg energy, as shown in Tables 5.1 and 5.2, the UPB is broader than the

77

LPB with increasing Rabi splitting because of its crossing with the scattering states of excitons. Nevertheless, it is still distinctable even the optical thickness of the active layer is 1.5λ [90]. Furthermore, the UPBs of GaN and ZnO become broader with increasing thickness of active layer and subsequently fade as the optical thickness of about 1 λ and 0.25 λ for GaN and ZnO, respectively. These calculated results are in good agreement with the experimental measurements in recent literatures [31], [32], [94], [96], [97]. It is obvious that the maximum thickness of active layer for the visible UPB is different in the three materials. To clearly probe the UPB in ZnO microcavities, the optical thickness of active layer should be kept thinner than 0.25 λ to suppress the absorption of scattering states, which may mainly originate from the onset of continuum absorption and the exciton-phonon complexes, especially at RT [86]. Moreover, there are observable intermediate polariton branchs (IPBs) in the map of the calculated reflectivity spectra nearby and above the exciton energy for GaN and ZnO microcavities. This issue will be discussed further in Sec. 5.4.

Table 5.2. Calculated Rabi splitting values and corresponding active layer thickness in GaAs, GaN, and ZnO microcavities.

	GaAs	GaN	ZnO
Active layer thickness (1λ)	230 nm	130 nm	150 nm
Rabi splitting (Ω)	4 meV	30 meV	70 meV

In addition, the important factor resulting in the discrepancies among the three materials is the product of the absorption coefficient and the active layer thickness ($\alpha \cdot d$). The absorption coefficients near the band edge of GaN and ZnO are about one order of magnitude larger than that of GaAs, as shown in Table 5.1. Specifically, a bulk GaAs with an optical thickness of 1.5λ will absorb 49% of photons in a single pass when the photon energy is near the onset of the continuum states. As for a bulk ZnO with an optical thickness of 1λ, there is 95% of photons absorbed by the continuum states. To

sum up the influence of the active thickness, when the thickness of bulk active layer increases, there are two mechanisms leading to the invisible UPBs for the wide-bandgap materials. One is the large Rabi splitting with increasing the active layer thickness, which pushes the UPB into the absorption of scattering states. The other is the increased absorption induced by the increase in the thickness of bulk active layer.

5.3 Influence of exciton-photon detuning

The effect of exciton-photon detuning dominates the polariton dispersion curves and therefore influences the characteristics of UPB. It has been observed that the linewidth of upper polariton increases with positive detuning due to the overlap between exciton scattering states and UPB in GaAs-based microcavities [98], [99]. Furthermore, semiclassical approach of linear dispersion theory including the continuum absorption presents the similar trend about detuning-dependent UPB linewidths [100]. Therefore, to further investigate the effect of exciton-photon detuning on the properties of UPB in these three materials, we fixed the optical thickness of active layer to be 0.5 λ for the three microcavities and slightly changed the cavity thickness to increase or decrease the exciton-photon detuning.

Fig. 5.4 shows the color maps of the calculated reflectivity spectra as a function of exciton-photon detuning for the three materials. A clear anticrossing behavior is observed for GaAs- and GaN-based microcavities, respectively. Nevertheless, when the exciton-photon detuning deviates from the zero detuning, the signature of the exciton-like polariton branches disappears rapidly in the GaAs microcavity. On the contrary, in the cases of GaN and ZnO microcavities, the exciton-like polariton branches are still visible for the large negative and positive detuning since their exciton oscillator strength values are one order larger than that of GaAs [39], [42], [91]. Furthermore, although the anticrossing can be observed in the GaN microcavity, the signature of the

UPB nearly disappears when the positive detuning is larger than about 10 meV.
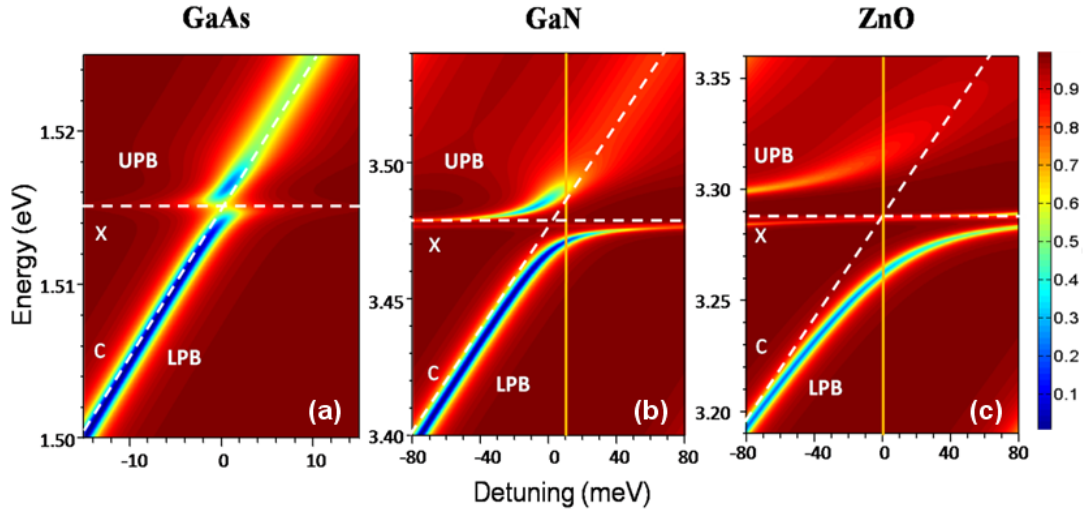
Fig. 5.4 Color maps of calculated reflectivity spectra as a function of exciton-photon detuning for (a) GaAs, (b) GaN, and (c) ZnO microcavities with λ active layer thickness at normal incidences. The pure cavity mode C and uncoupled exciton mode X are shown (white dashed line). The vertical yellow line represents the critical value of detuning for invisible UPB.

Similar situation also can be found in the ZnO microcavity when the detuning goes from negative to zero. For positive detuning, the upper polariton has high photon fractions, leading to the invisible UPB abruptly with increasing positive detuning due to the crossing with exciton scattering states. The UPB in GaAs microcavity is still distinct because the small term of $\alpha \cdot d$, as shown in Fig. 5.4(a). Therefore, in wide-bandgap materials it would be relatively easier to observe the UPB in the case of negative exciton-photon detuning, besides the thinner active layer thickness as discussed in section 5.2.

5.4 Influence of inhomogeneous broadening

Inhomogeneous broadening of excitons plays an important role in the investigation of strong exciton photon coupling as well, especially for wide-bandgap materials due to the difficulty in growth of high reflectivity DBRs and high Q cavities. The effect of

disorder on bulk polaritons results from the interaction between exciton states and imperfect bulk crystals. This mechanism breaks the conservation rule of in-plane wave vector in the exciton-photon interaction. As a result, the set of the disordered potential contributes to inhomogeneous broadening for the exciton-like polariton states in spectra. Currently, the epitaxial growth of wide-bandgap materials suffers from the severe strain accumulation in the DBRs, leading to crystal defects and potential fluctuations. Additionally, the small effective Bohr radius in wide-bandgap materials causes the polaritons more probably to be trapped by defects and perturbed by potential fluctuations, which results in the coherence length of polaritons to be significantly reduced.

As mentioned in the previous section, the calculated reflectivity spectra, as shown in Fig. 5.3, exhibit clear intermediate branches between the LPB and UPB. The IPBs are mainly resulted from the strong changes in the refractive index and the incoherent exciton absorption owing to the outcome of large exciton oscillator strength. However, these IPBs have never been observed experimentally in GaN- or ZnO-based microcavities [32], [97]. Furthermore, although the results shown in Fig. 5.4 present visible UPBs with sharp linewidth in the range of negative detuning for the three materials, most experimental results in reflectivity and photoluminescence spectra exhibit the broad linewidth of UPB [32], [97]. These differences are mainly attributed to the lack of inhomogeneous broadening in the calculation model. Therefore, in order to take the effect of inhomogeneous broadening into account, the simulation model is reconstructed from a convolution of a Lorentzian lineshape and a Gaussian lineshape, which is more appropriate in the case of inhomogeneous broadening. The exciton Gaussian lineshape is symmetrically distributed in our work to avoid the breaking of translational symmetry and to modify the polariton eigenstates [101].
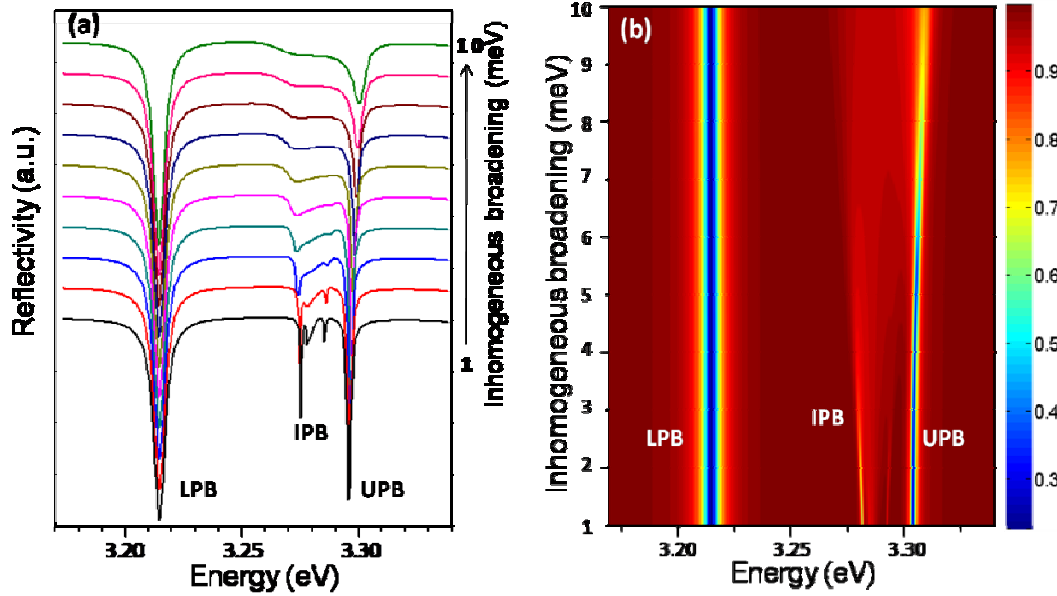
Fig. 5.5 (a) Calculated reflectivity spectra for the λ ZnO cavity at zero detuning and zero in-plane wave vector as varying the inhomogeneous broadening ranging from 1 to 10 meV. (b) Color map of the reflectivity spectra as a function of inhomogeneous broadening.

The calculated results shown in Fig. 5.4 indicate that the UPBs in the range of positive detuning are significantly broadened by the absorption of exciton scattering states. As for the UPBs in the range of negative detuning, the inhomogeneous broadening will be the dominating mechanism leading to the invisible UPBs due to the exciton-like polaritons. Fig. 5.5(a) shows the calculated reflectivity spectra for the λ ZnO cavity in the condition of negative detuning of 50 meV and zero in-plane wave vector as varying the inhomogeneous broadening ranging from 1 to 10 meV. Fig. 5.5(b) presents the color map of the reflectivity spectra as a function of inhomogeneous broadening. The LPB is clearly distinctable even if the inhomogeneous broadening increases to 10 meV. However, the intermediate dips (i.e., IPBs) resulting from the incoherent excitons rapidly vanish with increasing inhomogeneous broadening, and finally the UPB becomes blurred and fades as the inhomogeneous broadening approaches to 10 meV. The disappearance of UPB with increasing inhomogeneous

broadening is mainly induced by the intrinsic exciton-like properties for the condition of negative detuning. On the contrary, the LPB is photon-like and therefore robust in spite of the increase of inhomogeneous broadening. Consequently, the inhomogeneous broadening induced by crystal imperfection would also be an important factor causing the invisible UPB in wide-bandgap semiconductor microcavities.

5.5 Quantum well structure in microcavity

The above-discussed studies of strongly exciton-photon coupling are mainly based on bulk microcavities because of the simpler geometry and the easier fabrication in practice, especially for wide-bandgap materials. However, with the target of realizing an electrically pumped polariton laser, a more realistic structure would employ QWs to achieve lower threshold due to improved carrier confinement and large oscillator strength. Recently, the strong coupling based on a GaN/AlGaN multiple quantum well (MQW) microcavity structure has been experimentally demonstrated [24]. Nevertheless, the ZnO-based MQW microcavities, such as ZnO/ZnMgO, have not been reported. Therefore, we will now focus on the comparison of polariton dispersion curves in bulk ZnO and ZnO/ZnMgO MQW microcavities. The microcavity structures for the bulk ZnO and ZnO/ZnMgO MQW are identical except for the design of cavities. The cavity thickness of these two structures is 0.5λ and the MQW structure consists of three 3-nm ZnO QWs and 5-nm $Zn_{0.73}Mg_{0.27}O$ barriers, which are symmetrically distributed around the anti-node of the optical field. In addition, the variations of exciton transition and binding energies in a ZnO/$Zn_{0.73}Mg_{0.27}O$ QW as a function of well width have been investigated in the work by Coli and Bajaj [102]. The measured transition energy in a QW structure consisting of a 3-nm-thick ZnO well and $Zn_{0.73}Mg_{0.27}O$ barriers is about 3.39 eV [102], [103].
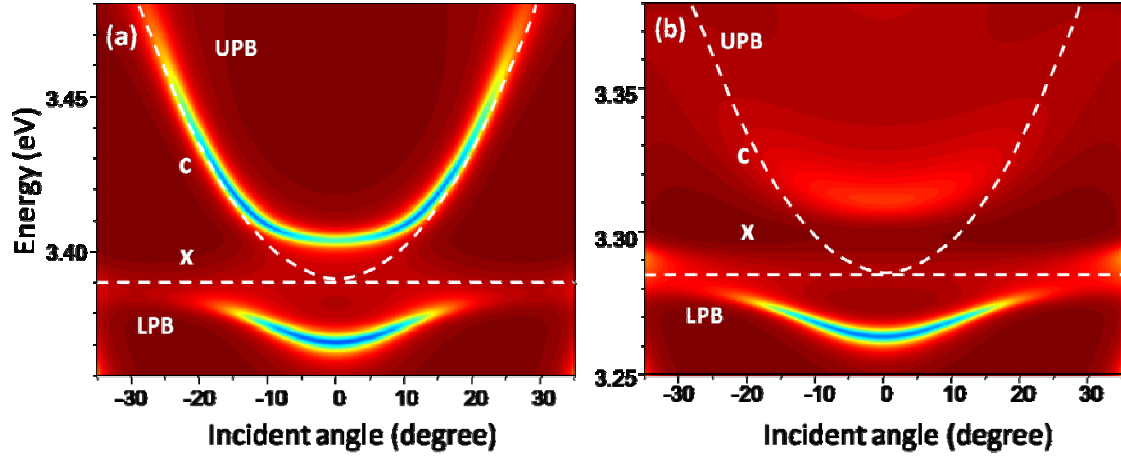
Fig. 5.6 Color maps of the calculated angle-resolved reflectivity spectra of 0.5-λ (a) MQW ZnO-based microcavity, (b) bulk ZnO-based microcavity.

Fig. 5.6 shows the comparison of the angle-resolved reflectivity spectra ranging from -35° to 35° between MQW and bulk ZnO-based microcavities. In Fig. 5.6 (a), it is obvious that the MQW ZnO-based microcavity presents an evident UPB. Therefore, it is easy to estimate the value of Rabi splitting. On the contrary, in the bulk ZnO microcavity the upper polariton is blurred and completely fades as a result of the intense damping by scattering states. The main factors resulting in the difference between MQW microcavity and bulk microcavity are essentially attributed to two factors. One is the product of the absorption coefficient and the cavity thickness ($\alpha \cdot d$). In the QWs-embedded microcavities this value is effectively reduced because of the thinner active layer thickness. To be more specific, the product ($\alpha \cdot d$) in a single pass is about 0.36 in the case of QWs-embedded microcavities, which is about ten times less than that in bulk ZnO microcavities (~3.0). The other is the difference in exciton binding energies. The QW structure is supposed to have larger exciton binding energy than bulk active layer. For ideal 2D QW structure, the exciton binding energy is expected to be 4 times larger than that in bulk active layer [43]. However, the practical QW is a quasi-2D structure since the wave functions of electron and hole are confined in the direction normal to the wafer surface in a finite well width, which implies that the exciton

84

binding energy in a quasi-2D QW is smaller than that in an ideal 2D QW. Additionally, the quantum confined Stark effect in c-axis ZnO QWs can shift the absorption peak and reduce exciton binding energies. Consequently, we assume the exciton binding energy of the ZnO/ZnMgO QW to be 99 meV in our calculation [104]. Under this condition, the exciton continuum states will be much far from the UPB, which is another benefit for the MQW ZnO-based microcavity in order to probe the visible UPB.

5.6 Summary

In summary, we have presented the numerical simulation about the investigation of different physical mechanisms inducing the broadening of UPB in semiconductor microcavities based on three different materials. According to the simulation results, the UPBs of the GaN- and ZnO-based microcavities will become indistinct when the thickness of optical cavity is larger than λ and 0.25λ, respectively. The invisible UPBs are mainly dominated by the product of the absorption coefficient and the active layer thickness. Furthermore, it is preferred to probe a visible UPB in the case of negative exciton-photon detuning since the UPB in positive detuning is photon-like and induces decoherence by exciton scattering states, especially for wide-bandgap microcavities. There is still a clear UPB in GaAs-based microcavity with thick bulk active layer due to the smaller absorption coefficient than that in wide-bandgap materials. In addition to the active layer thickness and exciton-photon detuning impact on the broadening of UPBs, the inhomogeneous broadening induced by crystal imperfection would also be an important factor causing the invisible UPB in wide-bandgap semiconductor microcavities. Finally, we demonstrated the potential for MQW ZnO-based microcavities to improve the visibility of UPB due to the large 2D exciton binding energy and the small product of absorption coefficient and active layer thickness. Therefore, the employment of MQW ZnO-based microcavities and the improvement of

wide-bandgap material quality will be necessary to observe well-defined strong coupling regime and even to achieve low-threshold polariton devices.

Chapter 6 Polariton relaxation bottleneck in bulk ZnO-based microcavities

Microcavity polaritons in strong coupling regime show an unique dispersion curve, leading to the effective mass of lower polariton changes by four order of magnitude from $k_{//}$ ~0 to high $k_{//}$ states in the LPB. This sharp difference in effective mass has directly corresponding changes in density of states of lower polaritons. The first experimental observation of strong coupling regime was reported in a GaAs-based microcavity [11]. Nevertheless, the experimental measurements of strong coupling in GaAs microcavities should be performed at cryogenic temperature due to the low exciton binding energy of 4 meV. Under this circumstance, a polariton relaxation bottleneck was observed due to the lack of phonon-assisted thermalization processes [105]. In this sense, wide-bandgap semiconductor materials have attracted much attention in this research field due to their large exciton binding energies [106]. Strong coupling in GaN-based microcavities has been observed at RT [107]. Furthermore, although the first demonstration of RT polariton lasing in bulk GaN microcavities has been reported [23], the presence of a polariton bottleneck in a similar GaN-based microcavity was observed at RT and the relevant mechanisms have been discussed [97], [108]. An alternative wide-bandgap material is ZnO, whose oscillator strength and exciton binding energy (~60 meV in the bulk layer) is even larger than nitride-based materials [28]. Therefore, the ZnO-based microcavity is promising for the fabrication of polariton-based optoelectronic devices operating at high working temperature. The polariton bottleneck effect has been reported in a ZnO microcavity from the measurement of angle-resolved PL in the Bragg-mode polariton branch [109]. Nevertheless, the clear observation of polariton bottleneck effect from the cavity-mode

polariton branch has not been well documented in ZnO-based microcavities and the corresponding relaxation mechanisms should be investigated in this wide-bandgap material. In this chapter, we evidence the clear observation of polariton bottleneck effect in ZnO hybrid microcavities and systematically investigate this effect over wide range of temperatures and exciton-photon detuning values δ. The relevant mechanisms leading to the possible presence of a polariton bottleneck in ZnO microcavities are discussed.

6.1 Relaxation mechanisms in microcavity polaritons

The relaxation bottleneck for polaritons was first discussed for bulk materials, and then for microcavity polaritons by Tassone *et al.* [110], [111]. Under the nonresonant excitation conditions, the excitons created by incident photons first relax rapidly by LO phonon relaxation (< 1 ps), followed by slower acoustic phonon emission to populate the high density of high-k exciton states (the exciton reservoir), as indicated schematically in Fig. 6.1. The excitons then relax from the reservoir into the region of strongly coupled polariton states. The polariton relaxation bottleneck arises due to the competition between phonon-assisted polariton relaxation (1-ns timescale) from the exciton reservoir and the increasing escape rate from the cavity as the polariton states become increasingly photon-like with decreasing k. Specifically, it can be understood in light of the peculiar dispersion of the lower polaritons, especially for relatively low pumping density. Above the bottleneck region, lower polaritons are mostly exciton-like, lifetime is long, energy density of states is large, and the change of energy with $k_{//}$ is gradual. These features cause the exciton-like lower polaritons to be effectively thermalized by phonon scattering. Below the bottleneck region, the lower polariton energy density of states drops by four orders of magnitude due to the decrease of the

lower polariton effective mass, while their lifetime also shortens by two orders of magnitude to 1~10 ps. Therefore, the rapid photon decay and reduced energy density of states lead to the effect of polariton relaxation bottleneck, especially at low temperature.
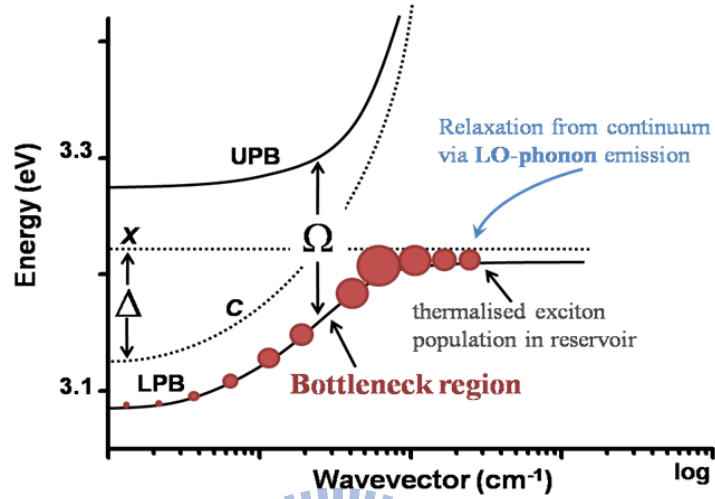
Fig. 6.1 Polariton (solid line) and uncoupled cavity mode (*C*) and exciton (*X*) dispersions. The mechanisms responsible for relaxation following nonresonant excitation are indicated. The polariton population is represented schematically by the solid circle symbols, with the maximum occurring at the edge of the polariton strongly coupled region.

In general, there are mainly three dynamical processes of the lower polariton system. The first one is polariton decay via the out-coupling of its photon component (mainly radiative). The lower polariton decay is characterized by the decay time $\tau_{LP} = \tau_{cav}/|C_{k//}|^2$, where $|C_{k//}|^2$ is the photon fraction of the lower polariton. The cavity lifetime is $\tau_{cav} = 1\sim10$ ps. For a given cavity, τ_{LP} increases with decreasing photon fraction. τ_{LP} is the shortest timescale for most microcavities at low pumping densities, leaving the system in non-equilibrium and sometimes shows a pronounced bottleneck.

The second one is polariton-polariton interactions. This is a nonlinear process with a timescale of a few ps and shortens with increasing polariton density. It is very likely to happen because of the non-parabolic shape of the dispersion relation. Each scattering

event can provide an energy exchange of a few meV. It is the main scattering process allowing population of the polariton trap and overcoming the bottleneck effect. When $\tau_{LP\text{-}LP}$ bceomes shorter than τ_{LP}, lower polaritons overcome the energy relaxation bottleneck and reach quantum degeneracy threshold. Due to the very efficient polariton-polariton scattering among states below the bottleneck, these lower polaritons thermalize among themselves before they decay, and form degenerate Bose-Einstein distribution.

The third one is polariton-phonon interaction, which is the only mechanism to cool the lower polaritons. The linear polariton-phonon scattering is a rather slow energy relaxation process at low densities with a more or less fixed timescale $\tau_{phonon} = 10\sim50$ ps, which is at least ten times longer than the polariton lifetime in the region. Fortunately, the polariton-phonon scattering can be significantly enhanced by the Bose final state stimulation effect. For bosons, transition rates into a given quantum state are enhanced by the presence of other identical bosons in that state. Explicitly, if N bosons occupy a given state, the transition rates into that state are proportional to (N+1). This effect is referred to as Bose stimulation and is most familiar as the gain mechanism in an optical laser [112]. If τ_{phonon} shortens to less than τ_{LP}, lower polaritons may have enough time to reach thermal equilibrium with the phonon bath within their lifetime.

6.2 Temperature- and detuning-dependent polariton relaxations

The present hybrid microcavity structure consists of a bulk ZnO $3\lambda/2$ thick cavity sandwiched between a bottom 30-pair AlN/Al$_{0.23}$Ga$_{0.77}$N DBR and a top 9-pair dielectric SiO$_2$/HfO$_2$ DBR. The AlN/AlGaN DBR was grown by MOCVD on a c-plane sapphire substrate. The bulk ZnO $3\lambda/2$ thick cavity was grown on AlN/AlGaN DBR by PLD system. Finally, the 9-period SiO$_2$/HfO$_2$ dielectric DBR was deposited by electron gun evaporation system to complete the microcavity structure. Nonresonant excitation

of the sample was performed using a 266 nm radiation from a forth harmonics of a Nd:YAG pulse laser with a repetition rate of 50 kHz and a pulse duration of 5 ns. The laser spot size on the sample surface was about 120 μm in diameter and the incident power density was about 50 W/cm^2. The PL emission light from the sample surface was collected using a UV optical fiber with 600 μm core mounted on a rotating stage with an angular resolution of ~1°, and detected by a liquid nitrogen cooled charge-coupled device attached to a 320 mm single monochromator with a spectral resolution of about 0.2 nm.
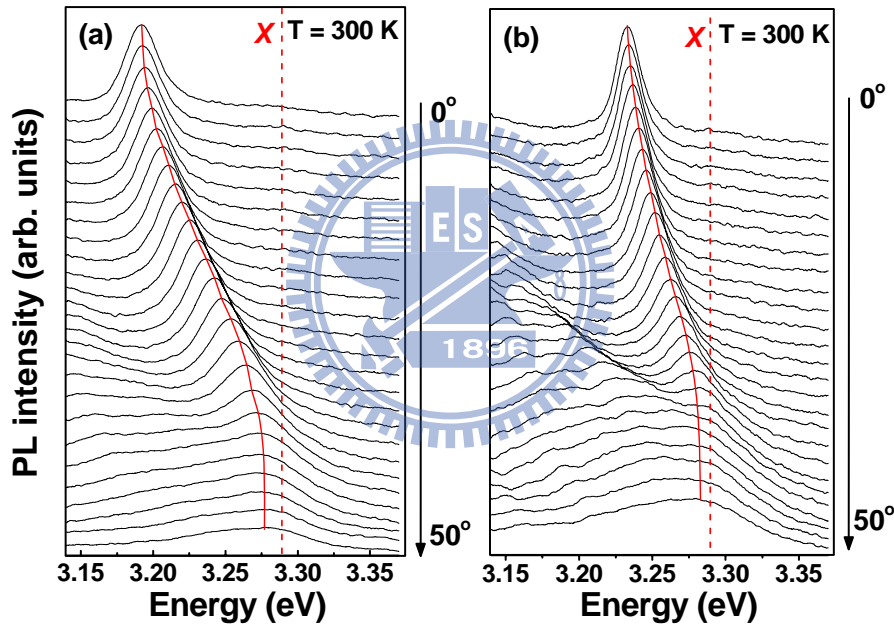
Fig. 6.2 The experimental angle-resolved PL spectra of the ZnO microcavities with approximate exciton-photon detunings of: (a) $\delta = -78$ meV, and (b) $\delta = -26$ meV at RT. The dashed line corresponds to the uncoupled exciton energy. The curve red line is a guide for the eyes, showing the dispersion of lower polariton branch.

The cavity quality factor of the ZnO microcavity is dependent on the pump beam spot size, which is induced by the contribution of different cavities originating from the microscopic fluctuation in thickness, interface roughness, and crystal imperfection. The different emission wavelengths cause the inhomogeneous broadening of the cavity

mode when using a larger laser spot size. This phenomenon is commonly observed in wide-bandgap materials due to the difficulty in growing high-quality DBRs and cavity layers [21]. A cavity quality factor of ~165 was probed from the PL measurements. However, when the laser spot size was focused to be about 10 um, the cavity quality factor of 320 was found, which demonstrates the high local quality of our ZnO microcavity structures. The sample was first studied by angle-resolved PL at RT. Two different detunings between the uncoupled photon and exciton modes at zero in-plane wave vector were considered to confirm the strong coupling phenomenon. Fig. 6.2 presents the experimental angle-resolved PL spectra of the ZnO microcavities with approximate detunings of (a) $\delta = -78$ meV, and (b) $\delta = -26$ meV at RT. The dashed line corresponds to the uncoupled exciton energy. Instead of a pure cavity mode following a parabolic dispersion, the LPB can be observed in these two cases. The photon-like LPB will approach to exciton-like LPB with increasing angle and finally converges to an energy that is close to uncoupled exciton. Furthermore, it is expected that the UPB is not observable as a result of the strong absorption of ZnO in this spectral range, as discussed in chapter 5 [84].

To get better understanding of the polairton occupancy and the corresponding competition between relaxation and emission processes, we further plot the color maps of the angular dispersions of measured PL spectra at different temperatures and detuning values. Figs. 6.3(a)~6.3(c) show the color maps of the angle-resolved PL spectra at the temperatures of (a) 100 K, (b) 200 K, and (c) 300 K for the case of $\delta = -78$ meV at RT. The strong redistribution of the polariton population is found with increasing temperature from 100 to 300 K. At low temperature (100 K), a maximum of the LP intensity can be observed at the angle of about 39° at which the energy difference between the cavity photon mode and the uncoupled exciton mode shows zero detuning. This condition can be considered an experimental demonstration of the presence of a

relaxation bottleneck, induced by the inefficient scattering rate of bottleneck polaritons into the ground state. The similar situation can be found when the temperature is 200 K.

Fig. 6.3 The color maps of the experimental angular dispersions of measured PL spectra at (a) 100 K, (b) 200 K, and (c) 300 K for the case of $\delta = -78$ meV at RT. The curved dashed lines represent the calculated LPBs and the curved dot line and horizontal dot line show the pure cavity and exciton modes, respectively. (d)~(f) show the calculated angle-dependent composition of the cavity photon and exciton modes for the three detunings induced by different temperatures.

Furthermore, the intensity of the LP emission spreads over a wide range of angle from 15° to 30° when the temperature is 300 K, as shown in Fig. 6.3(c). This enhanced polariton relaxation from the bottleneck should be caused through polariton-acoustic phonon interaction. On the other hand, with increasing temperature the decreases in exciton energy and in cavity-photon energy are resulted from a reduction of the bandgap energy and the temperature dependence of the refractive index, respectively. Therefore, the temperature-dependent detuning δ will also influence the distribution of polariton

emission due to the different exciton and photon fractions of the polariton states.

To get access to the exciton and photon contents in the mixed polariton states, we apply the quasiparticle model to obtain the expansion coefficients of the eigenstates on the exciton and photon basis [95]. The curved dashed lines shown in Figs. 6.3(a)~6.3(c) represent the calculated LPBs and the curved dot line and horizontal dot line show the pure cavity and exciton modes, respectively. Because of the temperature-dependent detuning, the angles of exciton-photon resonance are about 39°, 36°, and 31° for the temperatures of 100, 200 and 300 K, respectively. Furthermore, the Rabi splitting values, which increase with decreasing temperature, corresponding to the three temperatures are 67, 79, and 87 meV. This temperature-dependent Rabi splitting is also observed in recent studies [109], and may be induced by a decrease of the exciton oscillator strength with increasing temperature.
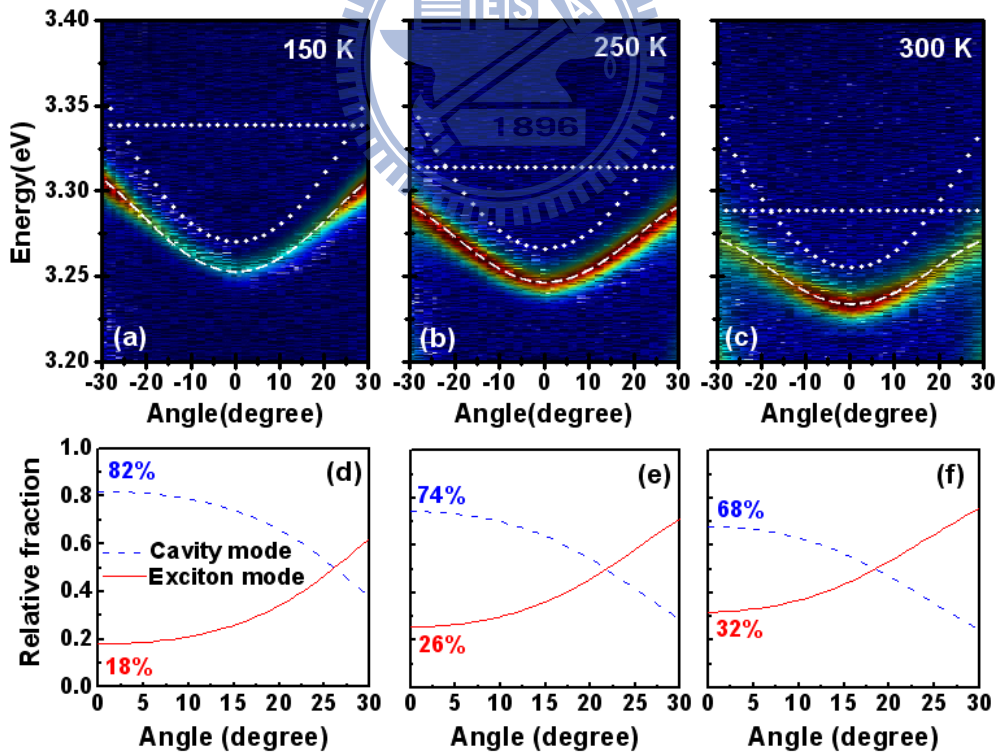
Fig. 6.4 The color maps of the experimental angular dispersions of measured PL spectra at (a) 150 K, (b) 250 K, and (c) 300 K for the case of $\delta = -26$ meV at RT. (d)~(f) show the calculated angle-dependent composition of the cavity photon and exciton modes for the three detunings induced by different temperatures.

Figs. 6.3(d)~6.3(f) show the angle-dependent composition of the cavity photon and exciton modes for the three detunings induced by different temperatures. The photon fractions at zero degree are 93%, 91%, and 85.5% with decreasing exciton-photon detuning. It is obvious that this high fraction of photon leads to the observable bottleneck effect even if the polariton relaxation is assisted by polariton-phonon interaction at 300 K. To further confirm the polariton relaxation mechanisms, we plot the color maps of the angle-resolved PL spectra and calculate the relevant exciton-photon fractions for the case of smaller detuning ($\delta = -26$ meV at RT) at different temperatures in Fig. 6.4. The obvious bottleneck effect can be found at 150 K when the photon fraction is about 82%. Furthermore, an uniform emission intensity ranging over 30° exhibits the dynamic competition between the phonon-assisted polariton relaxation and the escape of cavity photons at 250 K, as shown in Fig. 6.4(b). When the temperature rises to 300 K, the maximum emission intensity is centered at zero degree and a relaxation bottleneck is absent due to the increased polariton-phonon interaction and the lower photon fraction of 68% at zero degree [Fig. 6.4(c) and Fig. 6.4(f)].

Fig. 6.5 presents the color maps of the measured angle-resolved PL spectra at 150, 200, and 250 K for the exciton-photon detuning of −8 meV at 250 K. The corresponding exciton and photon fractions as a function of angle are calculated and shown in Fig. 6.5 as well. By comparing Figs. 6.4(c) and 6.5(a), based on the similar photon fraction of ~69% the polaritons can obtain the efficient scattering from high k states into lower k states by increasing the temperature from 150 to 300 K. On the other hand, at the same temperature of 200 K the obvious polariton bottleneck can be relaxed into the bottom of the LPB when the photon fraction is reduced from 91% to 63% [see Figs. 6.3(b), 6.3(e), 6.5(b), and 6.5(e)], which means the longer polariton lifetime is sufficient for the relaxation process under the condition of relatively fewer phonons at 200 K.

Furthermore, the LP emission intensity is more centered within a smaller range of angle when the temperature increases from 200 to 250 K.
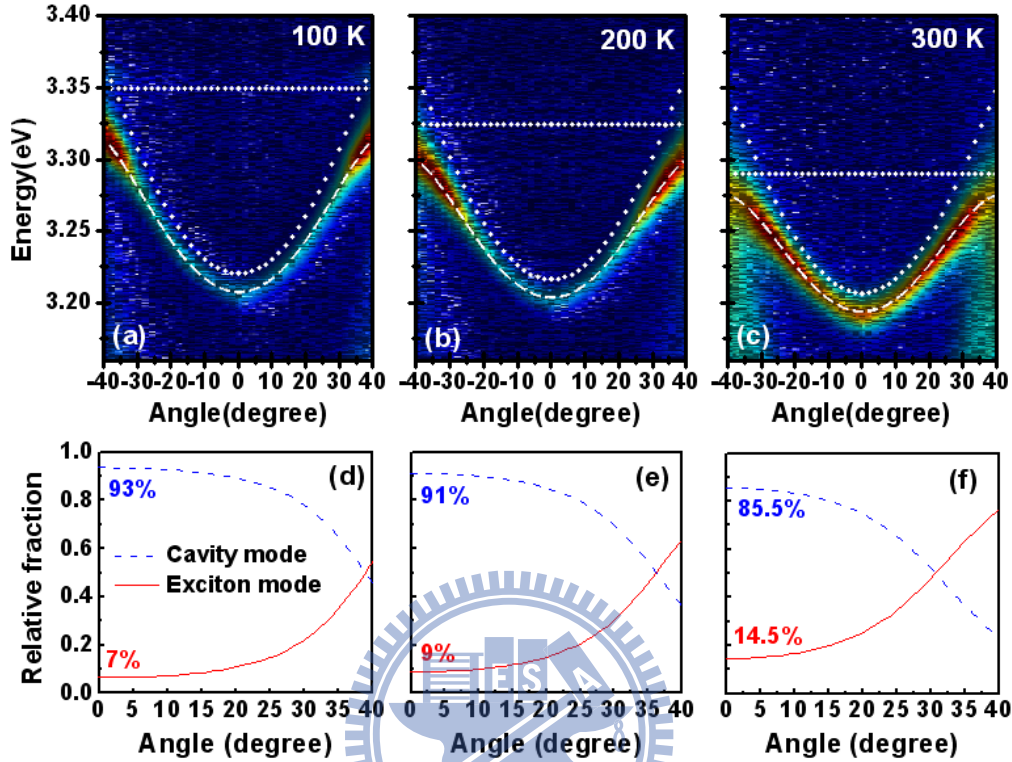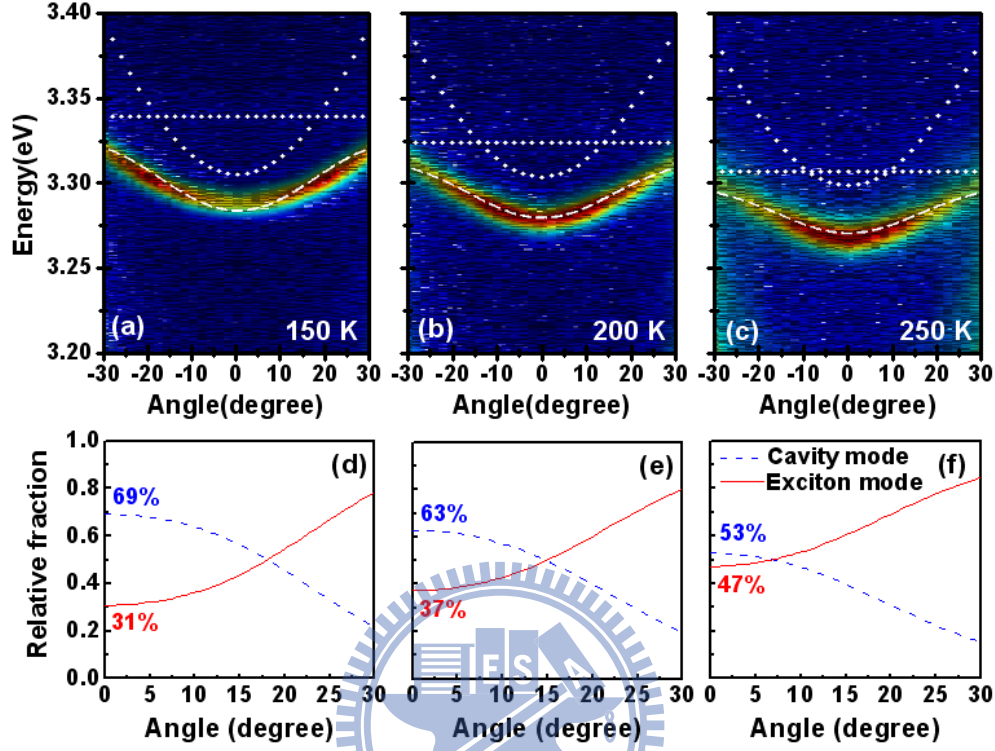

Fig. 6.5 The color maps of the experimental angular dispersions of measured PL spectra at (a) 150 K, (b) 200 K, and (c) 250 K for the case of $\delta = -8$ meV at 250 K. (d)~(f) show the calculated angle-dependent composition of the cavity photon and exciton modes for the three detunings induced by different temperatures.

Contrary to the case of large detuning ($\delta = -78$ meV at RT), the suppression of polariton relaxation bottleneck in the condition of small detuning ($\delta = -8$ meV at 250 K) mainly originates from the low photon fraction and therefore the bottleneck effect is absent at 200 K, which indicates the importance of exciton-photon detuning in the possible presence of polariton relaxation bottleneck. In addition to the effect of polariton-phonon interaction, the role of exciton-polariton or polariton-polariton scattering is discussed by performing the PL intensity dependence with angle at 150 K for the detuning of -26 meV and for incident power densities from 30 to 90 W/cm^2, as shown in Fig. 6.6. The PL intensity at small angles increases with excitation and a

suppression of the relaxation bottleneck can be observed. The polaritons relax from high

k states through their interaction with excitons and other polaritons with increasing

pumping power [29].
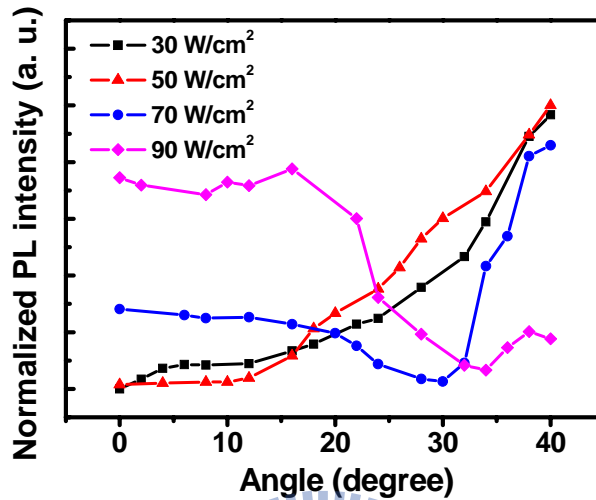
Fig. 6.6 Experimental PL intensities as a function of the detection angle for different excitation power densities at a temperature of 150 K for the detuning of −26 meV.

6.3 Power-dependent polariton relaxation and polariton lasing

In general, a straightforward question to ask is whether increasing pumping power

will lead to polariton lasing or to a collapse of the strong coupling regime and transition

to conventional weak coupling regime. As discussed in section 6.1, if the high-k

polaritons can be relaxed into the bottom of the lower polariton by various scattering

mechanisms together with the assistance of Bose stimulation, the condensation can be

achieved and the polariton lasing will be realized. Although the polariton BEC and

polariton lasing have been demonstrated in GaAs [14], CdTe [13], and GaN [23], the

polariton lasing or condensation has not yet been reported in the promising material of

ZnO. To examine the polariton behavior at high excitation, we measured the

power-dependent emission spectra of the ZnO hybrid microcavity using a

frequency-tripled Nd:YVO$_4$ 355-nm pulse laser with a pulse width of ~0.5 nm at a repetition rate of 1 kHz. The pumping laser beam with a spot size on the sample surface was about 120 μm in diameter.
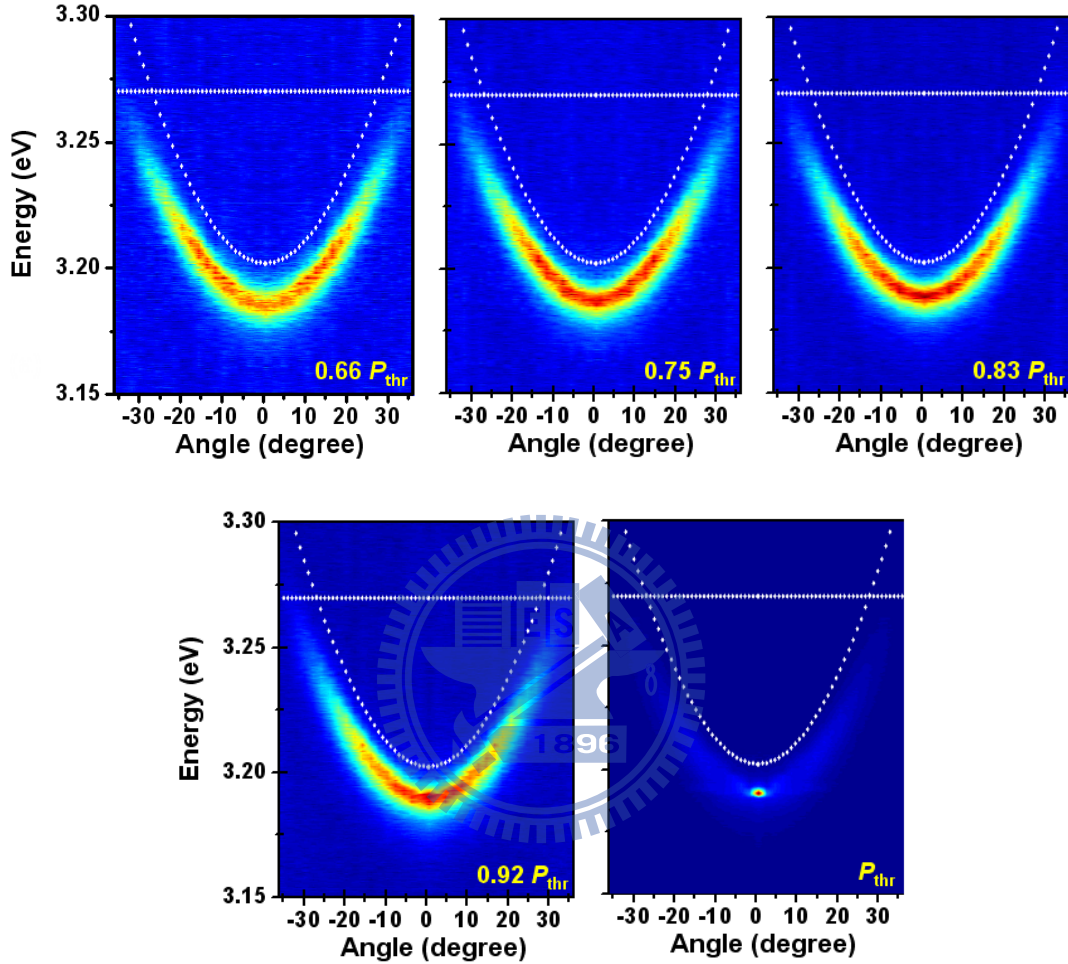
Fig. 6.7 The color maps of the experimental angular dispersions of measured PL spectra from the lower polariton branch at five different values of pumping as the detuning is −78 meV.

Fig. 6.7 shows RT intensity maps of the angle-resolved PL spectra from the lower polariton branch measured at five different values of pumping as the detuning is −78 meV. P_{thr} means threshold pumping power of 12 μW. This value is nearly two orders of magnitude smaller than that from an InGaN VCSEL with a Q value of 760. In addition, at low pumping (0.65 P_{thr}), the distribution of polariton population is uniform in the range of ±20°. Increasing the pumping power speeds up the relaxation kinetics due to

the onset of the polariton-polariton scattering mechanism. In Fig. 6.7, we increased the pumping power by a fixed step of 0.08 P_{thr}. One can see that the distribution of polariton population shifts to lower energies while increasing pumping power. The polariton population exhibits a significant difference between 0.92 P_{thr} and P_{thr}. This sudden polariton redistribution presents the much more effective scattering of polaritons to the ground state due to the bosonic final state stimulation effect, as discussed in section 6.1. Above threshold, the emission mainly comes from the lowest energy state at $k_{//} = 0$, showing a condensation of bosons.
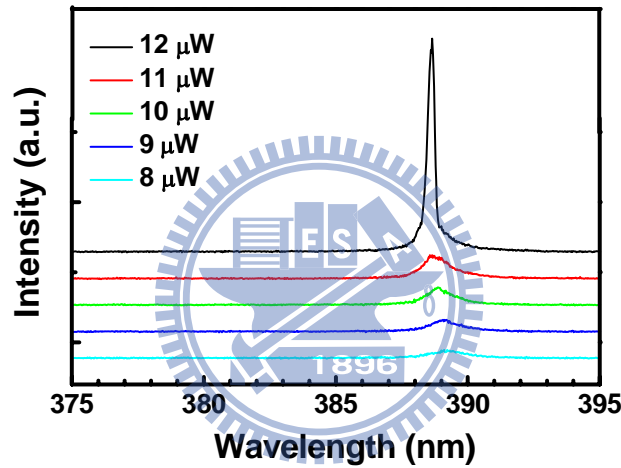
Fig. 6.8 The PL emission spectra from the lower polariton branch collected at zero degree in the conditions of below and above the stimulation threshold.

The emission spectra below and above the stimulation threshold is shown in Fig. 6.8, collected at zero degree. The increase of pumping power is fixed to be 1 μW, and the emission intensity has jumped obviously at threshold pumping power. The spectrum shape is also drastically different from those seen at lower pumping. The emission peak is extremely narrow both in energy and wave vector. This remarkable spectral narrowing indicates that, in the stimulation regime, the coherence time of the polariton population in the ground state is longer than the polariton lifetime.

Fig. 6.9(a) shows the lower polariton emission intensity as a function of the

exciting energy at room temperature conditions for the hybrid ZnO microcavity. A clear nonlinear behavior is found when the pumping power is 12 μW. Analysis of the power dependence yields the probability $\beta \sim 700^{-1}$, as shown in Fig. 6.9(b), that spontaneously emitted polaritons emerge in the mode which undergoes stimulated scattering. In conventional microcavity lasers, the cavity volume is small leading to a large Purcell factor which produces the β exceeding 1%. Planar semiconductor microcavities differ in that the cavity confines photons in only 1D, but the stimulated scattering from the bosonic nature of the polaritons leads to inversionless coherent emission, unrelated to the transparency condition.
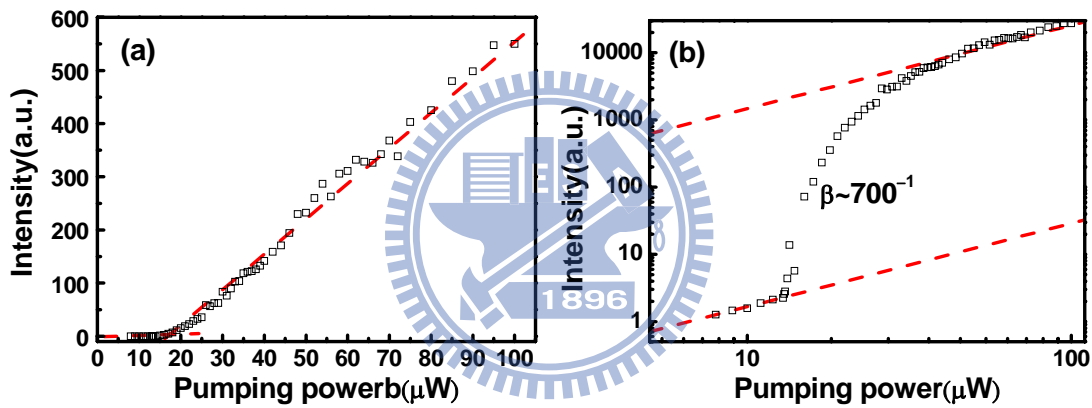
Fig. 6.9 (a) Lower polariton emission intensity as a function of the exciting energy at room temperature conditions for the hybrid ZnO microcavity. (b) Lower polariton emission intensity versus pumping energy in logarithmic scale. The difference between the heights of the emission intensities before and after the threshold corresponds roughly to the value of β. The dash lines are guides for the eye.

6.4 Summary

In summary, the strong polariton relaxation bottleneck has been observed in bulk ZnO-based microcavities at low temperature by performing angle-resolved PL measurements. The polariton relaxation from bottleneck to low k states can be enhanced

with increasing temperature. Nevertheless, in the case of large exciton-photon detuning $\delta = -78$ meV at RT, the relaxation bottleneck cannot be completely suppressed even if the temperature is increased to 300 K due to the high photon fraction of polaritons at low k states. Furthermore, in the case of small exciton-photon detuning $\delta = -8$ meV at 250 K, the lower photon fraction results in longer polariton lifetime sufficient for the relaxation process into the low k states even though the temperature is only 200 K. These results reveal the possible design rule for the consideration of different temperatures and exciton-photon detunings in order to suppress the polariton relaxation bottleneck in ZnO-based microcavities. Furthermore, the polariton lasing in ZnO microcavity has been demonstrated for the first time. The extremely low threshold pumping power and the relaxation of polaritons from high-k states to lowest-states with increasing pumping evidence the bosonic final state stimulation effect and the realization of polariton lasing in ZnO microcavity at RT.
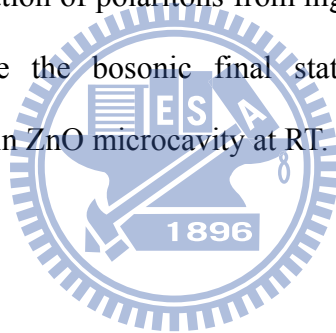
Chapter 7 Electrically pumped InGaN/GaN light-emitting diodes in strong coupling regime

The polariton BEC, amplification, and lasing have been demonstrated in GaAs, CdTe, and GaN. However, these results are only based on optical experiments by either non-resonant pumping or a stimulated polariton scattering to generate polaritons. From the view point of practical applications, polariton devices based on electrical injection would be more essential for the development of new-generation devices. An electrically pumped microcavity light-emitting diode (LED) has firstly been demonstrated by using organic semiconductors in 2005 [113]. Furthermore, a mid-infrared polariton cascade LED based on a GaAs/AlGaAs quantum cascade structure was reported in 2008 [114]. Subsequently, an electrically pumped GaAs semiconductor polariton LED was demonstrated in 2008 [16]. These results show an important breakthrough in the development of polariton devices under electrical injection. On the other hand, it is well known that the excitons in GaN-based semiconductors have larger exciton binding energy [20], [21], faster relaxation rate [115], and larger oscillator strength. In this sense, nitride-based material systems have attracted much attention in this research field due to their large exciton binding energy of about 26 meV for GaN bulk layers and about 40–50 meV for GaN-based quantum-well (QW) structures due to the quantum confinement effect. Although the observation of strong coupling from GaN-based microcavities has been reported in recent years [23], [116], these results are still probed in optical experiments. In contrast, an electrically pumped GaN-based polariton LED has not yet been reported because of the difficulty in growth of high-reflectivity nitride-based distributed Bragg reflectors (DBRs) and high-Q cavities with high-quality GaN-based QWs [22]. In this chapter, we report on the experimental realization of an

electrically pumped polariton LEDs in a high-quality InGaN microcavity at RT. Two approaches including temperature-dependent and angle-resolved electroluminescence spectra were employed to probe the exciton-cavity mode anticrossing. Furthermore, the measured electroluminescence spectra were theoretically investigated by using transfer matrix method that accurately reproduces our experimental results.

7.1 Sample preparation and device structure

The InGaN-based hybrid microcavity was firstly grown by MOCVD. The epitaxial structure mainly consists of a 29-pair AlN/GaN DBR and a 5λ (our target wavelength λ = 410 nm) optical thickness microcavity composed of a 790 nm-thick Si-doped n-type GaN, 10 pairs $In_{0.15}Ga_{0.85}N$ (2.5 nm) / GaN (7.5 nm) multiple-QWs MQWs, and a 120 nm-thick Mg-doped p-type GaN layer. The MQWs were located at the antinode of light field in the microcavity for enhancing the coupling of photons and the cavity mode. To obtain a crack-free and high reflectivity AlN/GaN DBR, we insert the AlN/ GaN superlattices into the AlN/GaN DBR structure during the epitaxial growth to reduce the biaxial tensile strain in AlN/GaN DBR [22]. The grown 29-pair AlN/GaN DBR showed a high peak reflectivity of R = 99.4% with a spectral band width of ~ 25 nm. The epitaxially grown structure was then processed to form the intra-cavity co-planar p- and n-contacts for current injection. A 0.2-µm thick SiN_x layer was used to form a current injection and a light emitting aperture of 10 µm in diameter. An ITO was deposited on top of the aperture to serve as the transparent contact layer. Finally an 8-pair Ta_2O_5/SiO_2 dielectric DBR (measured reflectivity of about 99% at λ = 410 nm) was deposited as the top DBR mirror to complete the full hybrid microcavity structure. Fig. 7.1 shows a schematic diagram of the fabricated InGaN-based microcavity.
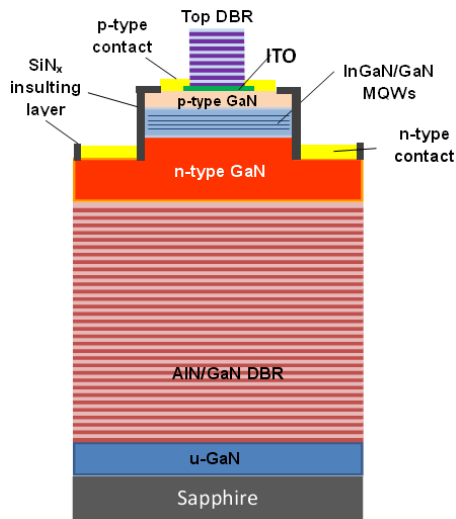
Fig. 7.1 The schematic diagram of the fabricated InGaN-based microcavity.

7.2 Temperature-dependent and angle-resolved electroluminescence spectra

Fig. 7.2(a) shows the electroluminescence spectrum from the polariton LED at 180 K, collected at zero angle when the input current is 2 mA. The measurement was performed in a temperature-controlled, closed-cycle, liquid nitrogen cryostat. A cavity quality factor of 300 was probed in this structure. The electroluminescence spectrum was further enlarged and focused in a range near emission peak, as shown in Fig. 7.2(b). It was found that there are two distinguishable emission peaks near the energy of 3.025 eV. This observation is very similar to the previous results reported by Tawara *et al.* [116]. To further confirm the origin of the two emission peaks, the electroluminescence spectra from the LED structure for different temperatures between 180 and 300 K were performed and collected at zero angle.

Fig. 7.3(a) shows the measured temperature-dependent electroluminescence spectra. It was observed that the high-energy emission intensity is increased with increasing temperature, and finally exceeded the low-energy peak in emission intensity. To shed more light on the temperature-dependent electroluminescence spectra, we

employed the transfer matrix method to calculate the transmission spectra of the microcavity structure. The shift of the cavity mode energy with increasing temperature is estimated to be about 0.1 meV/K [117], and the temperature-dependent emission energy of the quantum-well excitons follows the modified Varshni formula including the localization effect [118]

$$E(T) = E_m(0) - \frac{\alpha T^2}{T + \beta} - \frac{\sigma^2}{k_B T} , \tag{7.1}$$

where $E(T)$ is the emission energy at T, $E_m(0)$ is the energy gap at 0 K, α and β are Varshni's fitting parameters, k_B is the Boltzmann constant, and σ is related with localization effect. In this study, α is 0.635 meV/K, β is 1000 K, and σ is 17.5 meV. These values are estimated from the measured results of our bare InGaN/GaN MQWs, and are close to the values reported by relevant literatures [118], [119]. Furthermore, the resonant exciton was modeled by a Lorentz oscillator dispersive dielectric function.
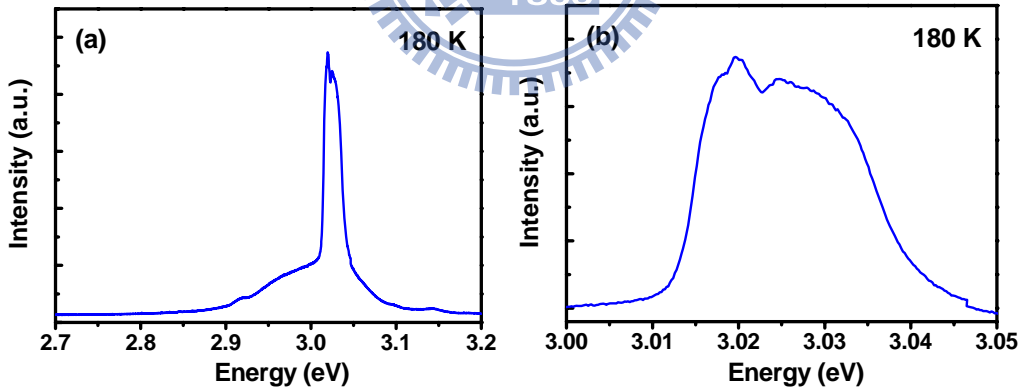
Fig. 7.2 (a) The electroluminescence spectrum from the polariton LED at 180 K, collected at zero angle when the input current is 2 mA. (b) The electroluminescence spectrum was enlarged and focused in a range near emission peak.

The simulation results of temperature-dependent spectra are shown in Fig. 7.3(b) from 180 to 300 K. It is noteworthy that the same evolution of the polariton branches as

in the experimental spectra is obtained when using the homogeneous linewidth of 15 meV in the InGaN excitons [116]. Moreover, the oscillator strength of the InGaN/GaN quantum well is 0.0289 eV^2 per quantum well. This value is of same order of magnitude as that of GaN QW exctions [39]. Fig. 7.3(b) presents an excellent fit of the temperature-dependent spectra. The minor deviations from experiment could be caused by the lack of temperature-dependent exciton oscillator in our calculation. The simulation results reveal that the condition of zero exciton-photon detuning at zero angle is reached at a temperature of 280 K and the normal mode Rabi splitting is about 6.5 meV.
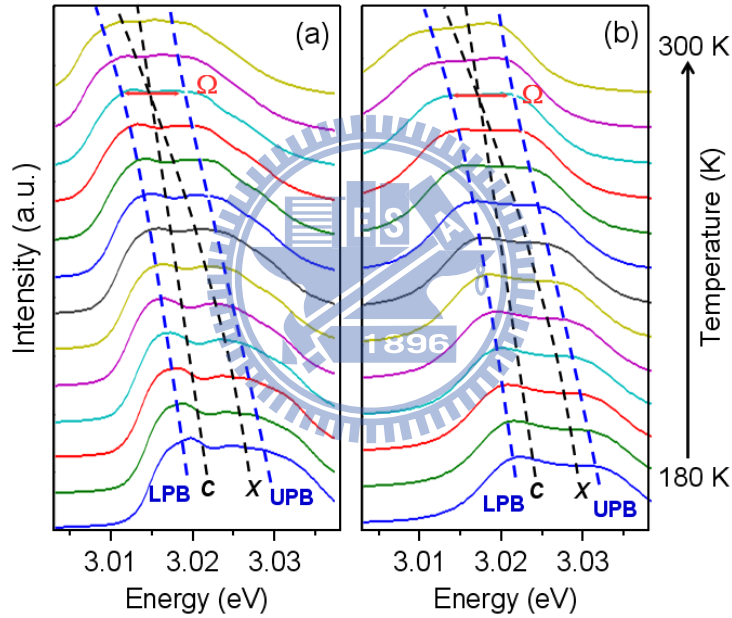
Fig. 7.3 (a) The measured temperature-dependent electroluminescence spectra from the emission of the lower polariton branch of the InGaN microcavity. (b) The calculated temperature-dependent spectra by using transfer matrix method with the consideration of temperature-dependent refractive index and exciton energy.

To further confirm the strong coupling regime in InGaN/GaN microcavity, we employ another approach to demonstrate the anticrossing dispersion curves in electroluminescence spectra. Angle-resolved electroluminescence measurements were performed at 180 K when the input current is 2 mA. Fig. 7.4(a) shows the measured

angle-resolved electroluminescence spectra, which reveals the well-resolved exciton and cavity modes, and exhibits the characteristic anticrossing behavior of the strong coupling regime. The calculated angle-resolved spectra are in good agreement with the measured results, as shown in Fig. 7.4(b). This angle-resolved technique is an important approach to tuning the cavity mode crossing the exciton mode for the negative detuning.
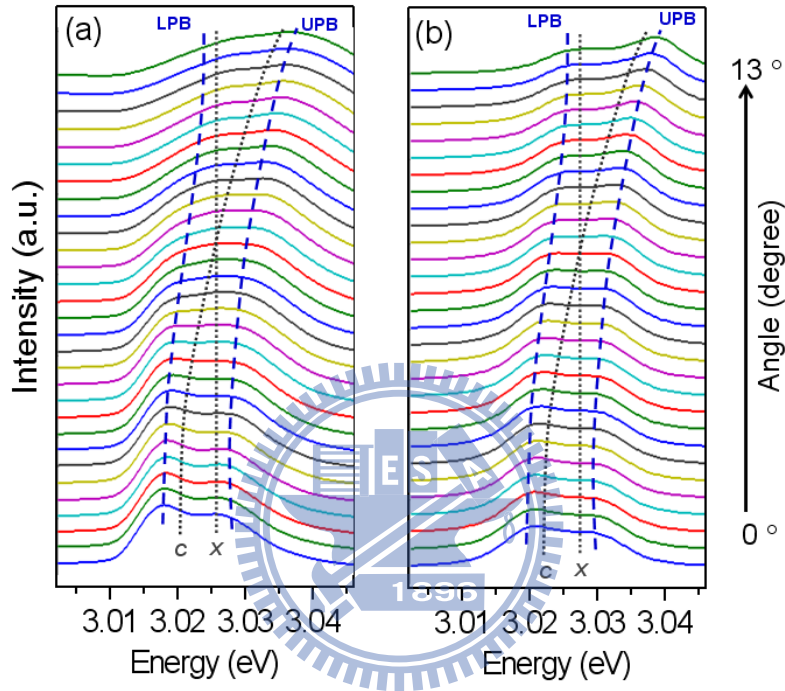
Fig. 7.4 (a) The measured angle-resolved electroluminescence spectra from the emission of the lower polariton branch of the InGaN microcavity. (b) The calculated angle-resolved spectra by using transfer matrix method.

To get better understanding of the dispersive features of the two polariton branches, the color maps of the angular dispersion of measured and calculated spectra from 0 to 13° are shown in Figs. 7.5(a) and 7.5(b), respectively. As can be seen from Fig. 7.5, we estimated that the anticrossing occurs near the angle of about 7.4° and the corresponding vacuum Rabi splitting value is about 7 meV, which is very close to that obtained from temperature-dependent experiment at 280 K.
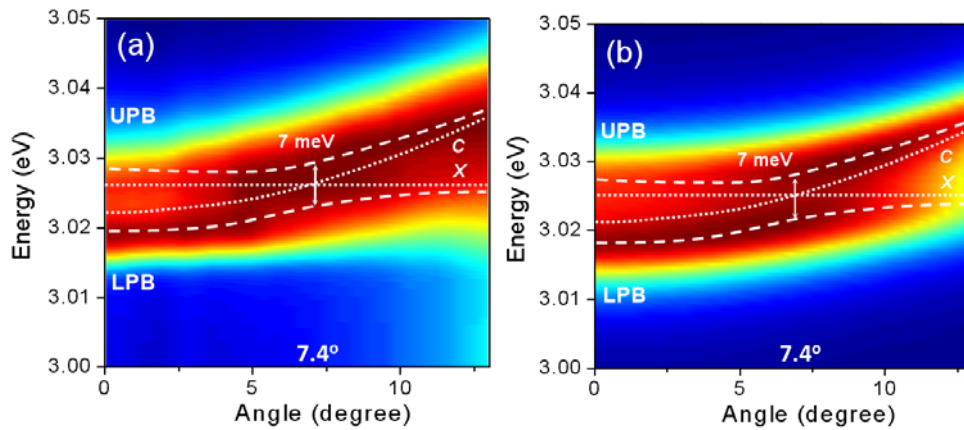
Fig. 7.5 The color maps of the angular dispersion of (a) measured and (b) calculated spectra from 0 to 13°.

7.3 Current-dependent polariton electroluminescence

It is well-known that the emission spectrum from an InGaN/GaN QW is commonly broadened due mainly to the indium composition fluctuation in the QW plane. The broadening of the light emission spectrum originates from the localized exciton states in the indium-rich regions. This intrinsic material property leads to inhomogeneous spectral broadening in the indium-containing nitride alloys [120], [121]. When the localized excitons in an InGaN-based QW have discrete energy states such as quantum dots, only those excitons whose energy matches the cavity resonant energy are picked out by the cavity filter effect. Of these localized excitons, only those whose energies are resonant with the cavity mode contribute Rabi splitting. The amount of Rabi splitting is determined by the homogeneous linewidth at the exciton energy [122]. This is generally disadvantageous in regards to strong coupling compared with the situation in a homogeneous QW where all excitons can couple to the cavity mode. In the InGaN-based QW microcavities, the localized excitons with large oscillator strengths at certain discrete energy levels enabled us to observe the Rabi splitting.
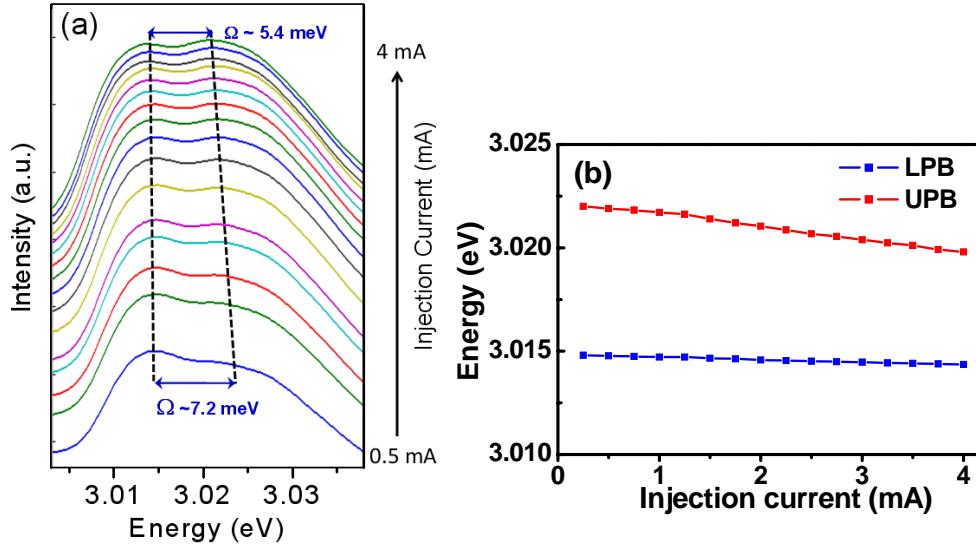
Fig. 7.6 (a) The electroluminescence spectra of the InGaN polariton LED as a function of injection current from 0.5 to 4 mA. (b) The decrease of Rabi splitting with increasing injection current.

Generally, it is excepted that the increase of injection current may achieve a polariton lasing or a collapse of the strong coupling regime due to the screening of the Coulomb interaction. To further probe the polariton properties of the InGaN microcavity at higher injection current, we resort to the current-dependent electroluminescence collected at zero degree under the condition of zeor-detuning at 240 K. Fig. 7.6(a) shows the electroluminescence spectra as a function of injection current from 0.5 to 4 mA. At low injection currents, two clearly resolved polariton peaks are evident. With increasing injection current, the two polariton peaks are progressively close to each other, leading to the decrease in Rabi splitting from 7.2 to 5.4 meV. We estimated that the density of 1.47×10^{19} polaritons cm^{-3} are injected per quantum well. Although this density is near exciton Mott density ($\sim 2.89 \times 10^{19} cm^{-3}$) [123], the Rabi-splitting is still observable. Fig. 7.6(b) presents the decrease of Rabi splitting with increasing injection current, which could originate from the increase of homogeneous broadening due to the enhaced exciton-exciton scattering.

7.4 Summary

In conclusion, we present an electrically pumped InGaN-based polariton LED in strong coupling regime. The results of temperature-dependent electroluminescence show the Rabi-splitting of 6 meV at 280K at 2-mA current injection. Furthermore, the angle-resolved electroluminescence spectra show the anti-crossing characteristic at 7.4° together with a Rabi splitting of 7 meV at 180 K. Theoretical calculations based on transfer matrix method are in good agreement with the experimental results. Furthermore, Rabi-splitting value decreases from 7.2 meV to 5.4 meV with the increase of carrier density, which results from the increase of homogeneous broadening owing to the mechanism of exciton-exciton scatterings.
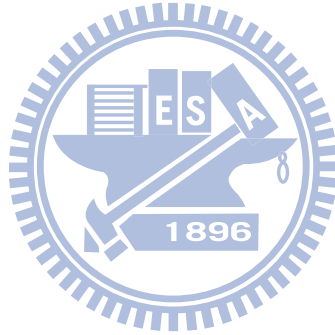
Chapter 8 Conclusion

Research on wide-bandgap semiconductor microcavity polaritons has been performed in this thesis. We firstly focused on the growth of high-reflectivity nitride-based ultraviolet DBRs for the purpose of fabricating the high-Q cavity. The ultraviolet DBRs successfully provide a reflectivity of larger than 90%. Based on this high-reflectivity ultraviolet DBR, we fabricated a ZnO-based hybrid microcavity with a cavity Q value of 320. By performing the angle-resolved reflectivity and PL spectra, the lower polariton branch can be evidently defined by combining the assistance of transfer matrix method, which demonstrated the strong coupling regime at RT and the vacuum Rabi splitting of 72 meV. In addition, the possible physical mechanisms leading to the invisible upper polariton branch are theoretically investigated as well. The invisible UPBs are mainly dominated by the product of the absorption coefficient and the active layer thickness. We further demonstrated the potential for MQW ZnO-based microcavities to improve the visibility of UPB due to the large 2D exciton binding energy and the small product of absorption coefficient and active layer thickness. Therefore, the employment of MQW ZnO-based microcavities and the improvement of wide-bandgap material quality will be necessary to observe well-defined strong coupling regime

To further understand the polariton relaxation mechanisms, we further performed the angle-resolved PL intensity mapping at different temperatures. The strong polariton relaxation bottleneck has been observed in bulk ZnO-based microcavities at low temperature. The polariton relaxation from bottleneck to low k states can be enhanced with increasing temperature. Nevertheless, in the case of large exciton-photon detuning $\delta = -78$ meV at RT, the relaxation bottleneck cannot be completely suppressed even if the temperature is increased to 300 K due to the high photon fraction of polaritons at

low k states. Furthermore, in the case of small exciton-photon detuning $\delta = -8$ meV at 250 K, the lower photon fraction results in longer polariton lifetime sufficient for the relaxation process into the low k states even though the temperature is only 200 K. These results reveal the possible design rule for the consideration of different temperatures and exciton-photon detunings in order to suppress the polariton relaxation bottleneck in ZnO-based microcavities.

The polariton lasing in this ZnO-based hybrid microcavity has been demonstrated for the first time. The extremely low threshold pumping power and the relaxation of polaritons from high-k states to lowest-states with increasing pumping evidence the bosonic final state stimulation effect and the realization of polariton lasing in ZnO microcavity at RT.

Finally, we present an electrically pumped InGaN-based polariton LED in strong coupling regime. Two different approaches including the temperature-dependent and angle-resolved electroluminescence spectra demonstrate an obvious polariton characteristic of anticrossing. Furthermore, the measured electroluminescence spectra were theoretically investigated by using transfer matrix method that accurately reproduces our experimental results.

References

[1]   K. J. Vahala, "Optical microcavities," *Nature*, vol. 424, pp. 839, 2003.

[2]   K. Iga, "Surface-emitting laser-its birth and generation of new optoelectronics field," *IEEE J. Select. Topics Quantum Electron.*, vol. 6, pp. 1201, 2000.

[3]   J. C. Knight, N. Dubreuil, V. Sandoghdar, J. Hare, V. Lefèvre-Seguin, J. M. Raimond, and S. Haroche, "Mapping whispering-gallery modes in microspheres with a near-field probe," *Opt. Lett.*, vol. 20, pp. 1515, 1995.

[4]   O. Painter, R. K. Lee, A. Scherer, A. Yariv, J. D. O'Brien, P. D. Dapkus, I. Kim, "Two-dimensional photonic band-gap defect mode laser," *Science*, vol. 284, pp. 1819, 1999.

[5]   E. Yablonovitch, "Inhibited spontaneous emission in solid-state physics and electronics," *Phys. Rev. Lett.*, vol. 58, pp. 2059, 1987.

[6]   J.-T. Chu, T.-C. Lu, H.-H. Yao, C.-C. Kao, W.-D. Liang, J.-Y. Tsai, H.-C. Kuo, and S.-C. Wang, "Room-temperature operation of optically pumped blue-violet GaN-based vertical-cavity surface-emitting lasers fabricated by laser lift-off," *Jpn. J. Appl. Phys.*, vol. 45, pp. 2556, 2006.

[7]   R. J. Thompson, G. Rempe, and H. J. Kimble, "Observation of normal-mode splitting for an atom in an optical cavity," *Phys. Rev. Lett.*, vol. 68, pp. 1132, 1992.

[8]   E. P. O'Reilly and A. R. Adams, "Band-structure engineering in strained semiconductor lasers," *IEEE J. Quantum Electron.*, vol. 30, pp. 366, 1994.

[9]   D. M. Whittaker, P. Kinsler, T. A. Fisher, M. S. Skolnick, A. Armitage, A. M. Afshar, M. D. Sturge, and J. S. Roberts, "Motional narrowing in semiconductor microcavities," *Phys. Rev. Lett.*, vol. 77, pp. 4792, 1996.

[10] J. J. Hopfield, "Theory of the contribution of excitons to the complex dielectric constant of crystals," *Phys. Rev.*, vol. 112, pp. 1555, 1958.

[11] C. Weisbuch, M. Nishioka, A. Ishikawa, and Y. Arakawa, "Observation of the coupled exciton-photon mode splitting in a semiconductor quatnum microcavity," *Phys. Rev. Lett.*, vol. 69, pp. 3314, 1992.

[12] M. H. Anderson, J. R. Ensher, M. R. Matthews, C. E. Wieman, and E. A. Cornell, "Observation of Bose-Einstein condensation in a dilute atomic vapor," *Science*, vol. 269, pp. 198, 1995.

[13] J. Kasprzak, M. Richard, S. Kundermann, A. Baas, P. Jeambrun, J. M. J. Keeling, F. M. Marchetti, M. H. Szymańska, R. André, J. L. Staehli, V. Savona, P. B. Littlewood, B. Deveaud, and L. S. Dang, "Bose-Einstein condensation of exciton polaritons," *Nature*, vol. 443, pp. 409, 2006.

[14] H. Deng, G. Weihs, C. Santori, J. Bloch, and Y. Yamamoto, "Condensation of

semiconductor microcavity exciton polaritons," *Science*, vol. 298, pp. 199, 2002.

[15] H. Deng, G. Weihs, D. Snoke, J. Bloch, and Y. Yamamoto, "Polariton lasing vs. photon lasing in a semiconductor microcavity," *Proc. Natl. Acad. Sci.*, vol. 100, pp. 15318, 2003.

[16] S. I. Tsintzos, N. T. Pelekanos, G. Konstantinidis, Z. Hatzopoulos, and P. G. Savvidis, "A GaAs polariton light-emitting diode operating near room temperature," *Nature*, vol. 453, pp. 372, 2008.

[17] S. I. Tsintzos, P. G. Savvidis, G. Deligeorgis, Z. Hatzopoulos, and N. T. Pelekanos, "Room temperature GaAs exciton-polariton light emitting diode," *Appl. Phys. Lett.*, vol. 94, pp. 071109, 2009.

[18] D. G. Lidzey, D. D. C. Bradley, M. S. Skolnick, T. Virgili, S. Walker, and D. M. Whittaker, "Strong exciton-photon coupling in an organic semiconductor microcavity," *Nature*, vol. 395, pp. 53, 1998.

[19] D. G. Lidzey, D. D. C. Bradley, A. Armitage, S. Walker, and M. S. Skolnick, "Photon-mediated hybridization of Frenkel excitons in organic semiconductor microcavities," *Science*, vol. 288, pp. 1620, 2000.

[20] K. Kornitzer, T. Ebner, K. Thonke, R. Sauer, C. Kirchner, V. Schwegler, M. Kamp, M. Leszczynski, I. Grzegory, and S. Porowski, "Photoluminescence and reflectance spectroscopy of excitonic transitions in high-qualtiy homoepitaxial GaN films," *Phys. Rev. B*, vol. 60, pp. 1471, 1999.

[21] G. Christmann, R. Butté, E. Feltin, A. Mouti, P. A. Stadelmann, A. Castiglia, J.-F. Carlin, and N. Grandjean, "Large vacuum Rabi splitting in a multiple quantum well GaN-based microcavity in the strong-coupling regime," *Phys. Rev. B*, vol. 77, pp. 085310, 2008.

[22] T.-C. Lu, J.-R. Chen, S.-W. Chen, H.-C. Kuo, C.-C. Kuo, C.-C. Lee, and S.-C. Wang, "Development of GaN-based vertical-cavity surface-emitting lasers", *IEEE J. Sel. Topics Quantum Electron.*, vol. 15, pp. 850, 2009.

[23] S. Christopoulos, G. B. H. Von Högersthal, A. J. D. Grundy, P. G. Lagoudakis, A. V. Kavokin, J. J. Baumberg, G. Christmann, R. Butté, E. Feltin, J.-F. Carlin, and N. Grandjean, "Room-temperature polariton lasing in semiconductor microcavities," *Phys. Rev. Lett.*, vol. 98, pp. 126405, 2007.

[24] G. Christmann, R. Butté, E. Feltin, J.-F. Carlin, and N. Grandjean, "Room temperature polariton lasing in a GaN/AlGaN multiple quantum well microcavity," *Appl. Phys. Lett.*, vol. 93, pp. 051102, 2008.

[25] S. F. Chichibu, T. Sota, G. Cantwell, D. B. Eason, and C. W. Litton, "Polarized photoreflectance spectra of excitonic polaritons in a ZnO single crystal," *J. Appl. Phys.*, vol. 93, pp. 756, 2003.

[26] D. C. Reynolds, D. C. Look, B. Jogai, C. W. Litton, G. Cantwell, and W. C. Harsch,

"Valence-band ordering in ZnO," *Phys. Rev. B*, vol. 60, pp. 2340, 1999.

[27] A. Teke, Ü. Özgür, S. Doğan, X. Gu, H. Morkoç, B. Nemeth, J. Nause, and H. O. Everitt, "Excitonic fine structure and recombination dynamics in single-crystalline ZnO," *Phys. Rev. B*, vol. 70, pp. 195207, 2004.

[28] M. Zamfirescu, A. Kavokin, B. Gil, G. Malpuech, and M. Kaliteevski, "ZnO as a material mostly adapted for the realization of room-temperature polariton lasers," *Phys. Rev. B*, vol. 65, pp. 161205(R), 2002.

[29] R. Johne, D. D. Solnyshkov, and G. Malpuech, "Theory of exciton-polariton lasing at room temperature in ZnO microcavities," *Appl. Phys. Lett.*, vol. 93, pp. 211105, 2008.

[30] R. Schmidt-Grund, B. Rheinländer, C. Czekalla, G. Benndorf, H. Hochmuth, M. Lorenz, and M. Grundmann, "Exciton-polariton formation at room temperature in a planar ZnO resonator structure," *Appl. Phys. B: Laser Opt.*, vol. 93, pp. 331, 2008.

[31] F. Médard, J. Zúñiga-Perez, P. Disseix, M. Mihailovic, J. Leymarie, A. Vasson, F. Semond, E. Frayssinet, J. C. Moreno, M. Leroux, S. Faure, and T. Guillet, "Experimental observation of strong light-matter coupling in ZnO microcavities: influence of large excitonic absorption," *Phys. Rev. B*, vol. 79, pp. 125302, 2009.

[32] R. Shimada, J. Xie, V. Avrutin, Ü. Özgür, and H. Morkoč, "Cavity polaritons in ZnO-based hybrid microcavities," *Appl. Phys. Lett.*, vol. 92, pp. 011127, 2008.

[33] H. M. Manasevit, "Single-crystal gallium arsenide on insulating substrates," *Appl. Phys. Lett.*, vol. 12, pp. 156, 1968.

[34] http://www.veeco.com/

[35] http://www.aixtron.com/index.php?id=1&L=1

[36] O. Ambacher, J. Smart, J. R. Shealy, N. G. Weimann, K. Chu, M. Murphy, W. J. Schaff, L. F. Eastman, R., Dimitrov, L. Wittmer, M. Stutzmann, W. Rieger, and J. Hilsenbeck, "Two-dimensional electron gases induced by spontaneous and piezoelectric polarization charges in N- and Ga-face AlGaN/GaN heterostructures," *J. Appl. Phys.*, vol. 85, pp. 3222, 1999.

[37] S. Chichibu, T. Azuhata, T. Sota, and S. Nakamura, "Spontaneous emission of localized excitons in InGaN single and multiquantum well structures," *Appl. Phys. Lett.*, vol. 69, pp. 4188, 1996.

[38] R. Houdré, C. Weisbuch, R. P. Stanley, U. Oesterle, P. Pellandini, and M. Ilegems, "Measurement of cavity-polariton dispersion curve from angle-resolved photoluminescence experiments," *Phys. Rev. Lett.*, vol. 73, pp. 2043, 1994.

[39] N. Ollier, F. Natali, D. Byrne, P. Disseix, M. Mihailovic, A. Vasson, J. Leymarie, F. Semond, and J. Massies, "Spectroscopy of a bulk GaN microcavity grown on Si(111)," *Jpn. J. Appl. Phys.*, vol. 44, pp. 4902, 2005.

[40] N. Antoine-Vincent, F. Natali, D. Byrne, A. Vasson, P. Disseix, J. Leymarie, M. Leroux, F. Semond, and J. Massies, "Observation of Rabi splitting in a bulk GaN microcavity grown on silicon," *Phys. Rev. B*, vol. 68, pp. 153313, 2003.

[41] M. Mihailovic, A. L. Henneghien, S. Faure, P. Disseix, J. Leymarie, A. Vasson, D. A. Buell, F. Semond, C. Morhain, and J. Zúñiga Pérez, "Optical and excitonic properties of ZnO films," *Opt. Mater.*, vol. 31, pp. 532, 2009.

[42] F. Médard, J. Zúñiga-Perez, E. Frayssinet, J. C. Moreno, F. Semond, S. Faure, P. Disseix, J. Leymarie, M. Mihailovic, A. Vasson, T. Guillet, and M. Leroux, "Optical study of bulk ZnO for strong coupling observation in ZnO-based microcavities," *Photonics Nanostruct. Fundam. Appl.*, vol. 7, pp. 26, 2009.

[43] S. L. Chuang, "*Physics of Optoelectronic Devices*," Wiley, New York, 1995.

[44] M. Diagne, Y. He, H. Zhou, E. Makarona, A.V. Nurmikko, J. Han, K.E. Waldrip, J.J. Figiel, T. Takeuchi, and M. Krames, "Vertical cavity violet light emitting diode incorporating an aluminum gallium nitride distributed Bragg mirror and a tunnel junction," *Appl. Phys. Lett.*, vol. 79, pp. 3720, 2001.

[45] T.-C. Lu, C.-C. Kao, H.-C. Kuo, G.-S. Huang, and S.-C. Wang, "CW lasing of current injection blue GaN-based vertical cavity surface emitting laser," *Appl. Phys. Lett.*, vol. 92, pp. 141102, 2008.

[46] S. Kako, C. Santori, K. Hoshino, S. Götzinger, Y. Yamamoto, and Y. Arakawa, "A gallium nitride single-photon source operating at 200 K," *Nature Mater.*, vol. 5, pp. 887, 2006.

[47] F. A. Ponce and D. P. Bour, "Nitride-based semiconductors for blue and green light-emitting devices," *Nature*, vol. 386, pp. 351, 1997.

[48] J. Li, T. N. Oder, M. L. Nakarmi, J. Y. Lin, and H. X. Jiang, "Optical and electrical properties of Mg-doped p-type $Al_xGa_{1-x}N$," *Appl. Phys. Lett.*, vol. 80, pp. 1210, 2002.

[49] E. F. Schubert, "*Light-Emitting Diodes*," Cambridge, New York, 2006.

[50] J.-F. Carlin and M. Ilegems, "High-quality AlInN for high index contrast Bragg mirrors lattice matched to GaN," *Appl. Phys. Lett.*, vol. 83, pp. 668, 2003.

[51] T. Fujimori, H. Imai, A. Wakahara, H. Okada, A. Yoshida, T. Shibata, M. Tanaka, "Growth and characterization of AlInN on AlN template," *J. Cryst. Growth*, vol. 272, pp. 381, 2004.

[52] G. S. Huang, T. C. Lu, H. H. Yao, H. C. Kuo, S. C. Wang, C.-W. Lin, and L. Chang, "Crack-free GaN/AlN distributed Bragg reflectors incorporated with GaN/AlN superlattices grown by metalorganic chemical vapor deposition," *Appl. Phys. Lett.*, vol. 88, pp. 061904, 2006.

[53] K. E. Waldrip, J. Han, J. J. Figiel, H. Zhou, E. Makarona, and A. V. Nurmikko, "Stress engineering during metalorganic chemical vapor deposition of AlGaN/GaN

distributed Bragg reflectors," *Appl. Phys. Lett.*, vol. 78, pp. 3205, 2001.

[54] H. P. D. Schenk, P. de Mierry, P. Vennéguès, O. Tottereau, M. Laügt, M. Vaille, E. Feltin, B. Beaumont, P. Gibart, S. Fernández, and F. Calle, "*In situ* growth monitoring of distributed GaN–AlGaN Bragg reflectors by metalorganic vapor phase epitaxy," *Appl. Phys. Lett.*, vol. 80, pp. 174, 2002.

[55] F. Natali, D. Byrne, A. Dussaigne, N. Grandjean, J. Massies, and B. Damilano, "High-Al-content crack-free AlGaN/GaN Bragg mirrors grown by molecular-beam epitaxy," *Appl. Phys. Lett.*, vol. 82, pp. 499, 2003.

[56] T. Wang, R. J. Lynch, P. J. Parbrook, R. Butté, A. Alyamani, D. Sanvitto, D. M. Whittaker, and M. S. Skolnick, "High-reflectivity $Al_xGa_{1-x}NAl_yGa_{1-y}N$ distributed Bragg reflectors with peak wavelength around 350 nm," *Appl. Phys. Lett.*, vol. 85, pp. 43, 2004.

[57] M. A. Mastro, R. T. Holm, N. D. Bassim, C. R. Eddy, Jr., D. K. Gaskill, R. L. Henry, and M. E. Twigg, "High-reflectance III-nitride distributed Bragg reflectors grown on Si substrates," *Appl. Phys. Lett.*, vol. 87, pp. 241103, 2005.

[58] O. Mitrofanov, S. Schmult, M. J. Manfra, T. Siegrist, N. G. Weimann, A. M. Sergent, and R. J. Molnar, " High-reflectivity ultraviolet AlGaN/AlGaN distributed Bragg reflectors," *Appl. Phys. Lett.*, vol. 88, pp. 171101, 2006.

[59] A. Bhattacharyya, S. Iyer, E. Iliopoulos, A. V. Sampath, J. Cabalu, T. D. Moustakas, and I. Friel, "High reflectivity and crack-free AlGaN/AlN ultraviolet distributed Bragg reflectors," *J. Vac. Sci. Technol. B*, vol. 20, pp. 1229, 2002.

[60] J.-R. Chen, S.-C. Ling, C.-T. Hung, T.-S. Ko, T.-C. Lu, H.-C. Kuo, and S.-C. Wang, "High-reflectivity ultraviolet AlN/AlGaN distributed Bragg reflectors grown by metalorganic chemical vapor deposition," *J. Cryst. Growth*, vol. 310, pp. 4871, 2008.

[61] J.-F. Carlin, J. Dorsaz, E. Feltin, R. Butté, N. Grandjean, M. Ilegems, and M. Laügt, "Crack-free fully epitaxial nitride microcavity using highly reflective AlInN / GaN Bragg mirrors," *Appl. Phys. Lett.*, vol. 86, pp. 031107, 2005.

[62] E. Feltin, J.-F. Carlin, J. Dorsaz, G. Christmann, R. Butté, M.Laügt, M. llegems, and N. Grandjean, "Crack-free highly reflective AlInN/AlGaN Bragg mirrors for UV applications," *Appl. Phys. Lett.*, vol. 88, pp. 051108, 2006.

[63] H. M. Ng, D. Doppalapudi, E. lliopoulos, and T. D. Moustakas, "Distributed Bragg reflectors based on AlN/GaN multilayers," *Appl. Phys. Lett.*, vol. 74, pp. 1036, 1999.

[64] H. M. Ng, T. D. Moustakas, and S. N. G. Chu, "High reflectivity and broad bandwidth AlN/GaN distributed Bragg reflectors grown by molecular-beam epitaxy," *Appl. Phys. Lett.*, vol. 76, pp. 2818, 2000.

[65] M. A. Mastro, R. T. Holm, N. D. Bassim, D. K. Gaskill, J. C. Culbertson, M.

Fatemi, C. R. Eddy, Jr., R. L. Henry, and M. E. Twigg, "Metal-organic chemical-vapor deposition of high-reflectance III-nitride distributed Bragg reflectors on Si substrates," *J. Vac. Sci. Technol. A*, vol. 24, pp. 1631, 2006.

[66] R. Butté, E. Feltin, J. Dorsaz, G. Christmann, J.-F. Carlin, N. Grandjean, and M. Ilegems, "Recent progress in the growth of highly reflective intride-based distributed Bragg reflectors and their use in microcavities," *Jpn. J. Appl. Phys.*, vol. 44, pp. 7207, 2005.

[67] D. Brunner, H. Angerer, E. Bustarret, F. Freudenberg, R. Höpler, R. Dimitrov, O. Ambacher, and M. Stutzmann, " Optical constants of epitaxial AlGaN films and their temperature dependence," *J. Appl. Phys.*, vol. 82, pp. 5090, 1997.

[68] G. M. Laws, E. C. Larkins, I. Harrison, C. Molloy, and D. Somerford, "Improved refractive index formulas for the $Al_xGa_{1-x}N$ and $In_yGa_{1-y}N$ alloys," *J. Appl. Phys.*, vol. 89, pp. 1108, 2001.

[69] B. Gil, O. Briot, and R.-L. Aulombard, "Valence-band physics and the optical properties of GaN epilayers grown onto sapphire with wurtzite symmetry," *Phys. Rev. B*, vol. 52, pp. R17028, 1995.

[70] N. Nakada, M. Nakaji, H. Ishikawa, T. Egawa, M. Umeno, and T. Jimbo, "Improved characteristics of InGaN multiple-quantum-well light-emitting diode by GaN/AlGaN distributed Bragg reflector grown on sapphire," *Appl. Phys. Lett.*, vol. 76, pp. 1804, 2000.

[71] N. Nakada, H. Ishikawa, T. Egawa, and T. Jimbo, "Suppression of Crack Generation in GaN/AlGaN Distributed Bragg Reflector on Sapphire by the Insertion of GaN/AlGaN Superlattice Grown by Metal-Organic Chemical Vapor Deposition," *Jpn. J. Appl. Phys.*, vol. 42, pp. L144, 2003.

[72] S.-Y. Huang, R.-H. Horng, W.-K. Wang, and D.-S. Wuu, "Fabrication and characterization of InGaN resonant-cavity light-emitting diodes on silicon substrates," *Phys. Stat. Sol. (c)*, vol. 3, pp. 2137, 2006.

[73] S. Adachi, *Physical Properties of III-V Semiconductor Compounds*, Wiley, New York, 1992.

[74] T. Peng and J. Piprek, "Refractive index of AlGaInN alloys," *Electron. Lett.*, vol. 32, pp. 2285, 1996.

[75] S. J. Hearne, J. Han, S. R. Lee, J. A. Floro, D. M. Follstaedt, E. Chason, and I. S. T. Tsong, "Brittle-ductile relaxation kinetics of strained AlGaN/GaN heterostructures," *Appl. Phys. Lett.*, vol. 76, pp. 1534, 2000.

[76] J. A. Floro, D. M. Follstaedt, P. Provencio, S. J. Hearne, and S. R. Lee, "Misfit dislocation formation in the AlGaN/GaN heterointerface," *J. Appl. Phys.*, vol. 96, pp. 7087, 2004.

[77] A. Tsukazaki, A. Ohtomo, T. Onuma, M. Ohtani, T. Makino, M. Sumiya, K. Ohtani,

S. F. Chichibu, S. Fuke, Y. Segawa, H. Ohno, H. Koinuma, and M. Kawasaki, "Repeated temperature modulation epitaxy for p-type doping and light-emitting diode based on ZnO," *Nat. Mater.*, vol. 4, pp. 42, 2005.

[78] Z. K. Tang, G. K. L. Wong, P. Zu, M. Kawasaki, A. Ohtomo, H. Koinuma, and Y. Segawa, "Room-temperature ultraviolet laser emission from self-assembled ZnO microcrystallite thin films," *Appl. Phys. Lett.*, vol. 72, pp. 3270, 1998.

[79] R. E. Sherriff, D. C. Reynolds, D. C. Look, B. Jogai, J. E. Hoelscher, T. C. Collins, G. Cantwell, and W. C. Harsch, "Photoluminescence measurements from the two polar faces of ZnO," *J. Appl. Phys.*, vol. 88, pp. 3454, 2000.

[80] S. W. Jung, W. I. Park, H. D. Cheong, G. C. Yi, H. M. Jang, S. Hong, and T. Joo, "Time-resolved and time-integrated photoluminescence in ZnO epilayers grown on Al$_2$O$_3$(0001) by metalorganic vapor phase epitaxy," *Appl. Phys. Lett.*, vol. 80, pp. 1924, 2002.

[81] K. Vanheusden, C. H. Seager, W. L. Warren, D. R. Tallant, and J. A. Voigt, "Correlation between photoluminescence and oxygen vacancies in ZnO phosphors," *Appl. Phys. Lett.*, vol. 68, pp. 403, 1996.

[82] Y. Chen, D. M. Bagnall, H. Koh, K. Park, K. Hiraga, Z. Zhu, and T. Yao, "Plasma assisted molecular beam epitaxy of ZnO on c-plane sapphire: Growth and characterization," *J. Appl. Phys.*, vol. 84, pp. 3912, 1998.

[83] E. S. Shim, H. S. Kang, J. S. Kang, J. H. Kim, and S. Y. Lee, "Effect of the variation of film thickness on the structural and optical properties of ZnO thin films deposited on sapphire substrate using PLD," *Appl. Surf. Sci.*, vol. 186, pp. 474, 2002.

[84] S. Faure, T. Guillet, P. Lefebvre, T. Bretagnon, and B. Gil, "Comparison of strong coupling regimes in bulk GaAs, GaN, and ZnO semiconductor microcavities," *Phys. Rev. B*, vol. 78, pp. 235323, 2008.

[85] G. E. Jellison and L. A. Boatner, "Optical functions of uniaxial ZnO determined by generalized ellipsometry," *Phys. Rev. B*, vol. 58, pp. 3586, 1998.

[86] W. Y. Liang and A. D. Yoffe, "Transmission Spectra of ZnO Single Crystals," *Phys. Rev. Lett.*, vol. 20, pp. 59, 1968.

[87] H. D. Sun, T. Makino, Y. Segawa, M. Kawasaki, A. Ohtomo, K. Tamura, and H. Koinuma, "Enhancement of exciton binding energies in ZnO/ZnMgO multiquantum wells," *J. Appl. Phys.*, vol. 91, pp. 1993, 2002.

[88] H. D. Sun, T. Makino, N. T. Tuan, Y. Segawa, Z. K. Tang, G. K. L. Wong, M. Kawasaki, A. Ohtomo, K. Tamura, and H. Koinuma, "Stimulated emission induced by exciton–exciton scattering in ZnO/ZnMgO multiquantum wells up to room temperature," *Appl. Phys. Lett.*, vol. 77, pp. 4250, 2000.

[89] R. J. Elliott, "Intensity of Optical Absorption by Excitons," *Phys. Rev.*, vol. 108, pp.

1384, 1957.

[90] A. Tredicucci, Y. Chen, V. Pellegrini, M. Böger, L. Sorba, and F. Beltram, "Controlled Exciton-Photon Interaction in Semiconductor Bulk Microcavities," *Phys. Rev. Lett.*, vol. 75, pp. 3906, 1995.

[91] Y. Chen, A. Tredicucci, and F, Bassani, "Bulk exciton polaritons in GaAs microcavities," *Phys. Rev. B*, vol. 52, pp. 1800, 1995.

[92] M. D. Sturge, "Optical Absorption of Gallium Arsenide between 0.6 and 2.75 eV," *Phys. Rev.*, vol. 127, pp. 768, 1962.

[93] J. F. Muth, J. H. Lee, I. K. Shmagin, R. M. Kolbas, H. C. Casey, B. P. Keller, U. K. Mishra, and S. P. DenBaars, "Absorption coefficient, energy gap, exciton binding energy, and recombination lifetime of GaN obtained from transmission measurements," *Appl. Phys. Lett.*, vol. 71, pp. 2572, 1997.

[94] J.-R. Chen, T.-C. Lu, Y.-C. Wu, S.-C. Lin, W.-R. Liu, W.-F. Hsieh, C.-C. Kuo, and C.-C. Lee, " Large vacuum Rabi splitting in ZnO-based hybrid microcavities observed at room temperature," *Appl. Phys. Lett.*, vol. 94, pp. 061103, 2009.

[95] V. Savona, L. C. Andreani, P. Schewndimann, and A. Quattropani, "Quantum well excitons in semiconductor microcavities: Unified treatment of weak and strong coupling regimes," *Solid State Commun.*, vol. 93, pp. 733, 1995.

[96] F. Réveret, F. Médard, P. Disseix, J. Leymarie, M. Mihailovic, A. Vasson, I. R. Sellers, F. Semond, M. Leroux, and J. Massies, "Optical investigations of bulk and multi-quantum well nitride-based microcavities," *Opt. Mater.*, vol. 31, pp. 505, 2009.

[97] R. Butté, G. Christmann, E. Feltin, J.-F. Carlin, M. Mosca, M. Ilegems, and N. Grandjean, "Room-temperature polariton luminescence from a bulk GaN microcavity," *Phys. Rev. B*, vol. 73, pp. 033315, 2006.

[98] R. Rapaport, A. Qarry, G, Ramon, E. Cohen, A. Ron, and L. N. Pfeiffer, "Free electron effects on the cavity polariton linewidth in an AlAs/AlGaAs microcavity containing a two-dimensional electron gas," *Solid State Commun.*, vol. 120, pp. 387, 2001.

[99] J. R. Jensen, P. Borri, W. Langbein, and J. M. Hvam, " Ultranarrow polaritons in a semiconductor microcavity," *Appl. Phys. Lett.*, vol. 76, pp. 3262, 2000.

[100] M. M. Mellitia, R. Chtouroua, J. Blockb, and V. Thierry-Miegb, "Influence of disorder on microcavity polariton linewidths," *Physica E*, vol. 30, pp. 17, 2005.

[101] V. Savona and C. Piermarocchi, "Microcavity Polaritons: Homogeneous and Inhomogeneous Broadening in the Strong Coupling Regime," *Phys. Stat. Sol (a)*, vol. 164, pp. 45, 1997.

[102] G. Coli and K. K. Bajaj, "Excitonic transitions in ZnO/MgZnO quantum well heterostructures," *Appl. Phys. Lett.*, vol. 78, pp. 2861, 2001.

[103] K. Koike, G.-Y. Takada, K. Fujimoto, S. Sasa, M. Inoue, and M. Yano, "Characterization of [ZnO]$_m$[ZnMgO]$_n$ multiple quantum wells grown by molecular beam epitaxy," *Physica E*, vol. 32, pp. 191, 2006.

[104] R. T. Senger and K. K. Bajaj, "Binding energies of excitons in polar quantum well heterostructures," *Phys. Rev. B*, vol. 68, pp. 205314, 2003.

[105] A. I. Tartakovskii, M. Emam-Ismail, R. M. Stevenson, M. S. Skolnick, V. N. Astratov, D. M. Whittaker, J. J. Baumberg, and J. S. Roberts, "Study of wide-bandgap semiconductor microcavRelaxation bottleneck and its suppression in semiconductor microcavitiesties," *Phys. Rev. B*, vol. 62, pp. R2283, 2000.

[106] I. R. Sellers, F. Semond, M. Leroux, J. Massies, M. Zamfirescu, F. Stokker-Cheregi, M. Gurioli, A. Vinattieri, M. Colocci, A. Tahraoui, and A. A. Khalifa, "Polariton emission and reflectivity in GaN microcavities as a function of angle and temperature," *Phys. Rev. B*, vol. 74, pp. 193308, 2006.

[107] A. Alyamani, D. Sanvitto, A. A. Khalifa, M. S. Skolnick, T. Wang, F. Ranalli, P. J. Parbrook, A. Tahraoui, and R. Airey, "GaN hybrid microcavities in the strong coupling regime grown by metal-organic chemical vapor deposition on sapphire substrates," *J. Appl. Phys.*, vol. 101, pp. 093110, 2007.

[108] F. Stokker-Cheregi, A. Vinattieri, F. Semond, M. Leroux, I. R. Sellers, J. Massies, D. Solnyshkov, G. Malpuech, M. Colocci, and M. Gurioli, "Polariton relaxation bottleneck and its thermal suppression in bulk GaN microcavities," *Appl. Phys. Lett.*, vol. 92, pp. 042119, 2008.

[109] S. Faure, C. Brimont, T. Guillet, T. Bretagnon, B. Gil, F. Médard, D. Lagarde, P. Disseix, J. Leymarie, J. Zúñiga-Pérez, M. Leroux, E. Frayssinet, J. C. Moreno, F. Semond, and S. Bouchoule, "Relaxation and emission of Bragg-mode and cavity-mode polaritons in a ZnO microcavity at room temperature," *Appl. Phys. Lett.*, vol. 95, pp. 121102, 2009.

[110] F. Tassone, C. Piermarocchi, V. Savona, A. Quattropani, and P. Schwendimann, "Bottleneck effects in the relaxation and photoluminescence of microcavity polaritons," *Phys. Rev. B*, vol. 56, pp. 7554, 1997.

[111] F. Tassone and Y. Yamamoto, "Exciton-exciton scattering dynamics in a semiconductor microcavity and stimulated scattering into polaritons," *Phys. Rev. B*, vol. 59, pp. 10830, 1999.

[112] H.-J. Miesner, D. M. Stamper-Kurn, M. R. Andrews, D. S. Durfee, S. Inouye, and W. Ketterle, "Bosonic stimulation in the formation of a Bose-Einstein condensate," *Science*, vol. 279, pp. 1005, 1998.

[113] J. R. Tischler, M. S. Bradley, V. Bulović, J. H. Song, and A. Nurmikko, "Strong coupling in a microcavity LED," *Phys. Rev. Lett.*, vol. 95, pp. 036401, 2005.

[114] L. Sapienza, A. Vasanelli, R. Colombelli, C. Ciuti, Y. Chassagneux, C. Manquest,

U. Gennser, and C. Sirtori, "Electrically injected cavity polaritons," *Phys. Rev. Lett.*, vol. 100, pp. 136806, 2008.

[115] U. Ozgur, M. J. Bergmann, H. C. Casey, H. O. Everitt, A. C. Abare, S. Keller, and S. P. DenBaars, "Ultrafast optical characterization of carrier capture times in $In_xGa_{1-x}N$ multiple quantum wells," *Appl. Phys. Lett.*, vol. 77, pp. 109, 2000.

[116] T. Tawara, H. Gotoh, T. Akasaka, N. Kobayashi, and T. Saitoh, "Cavity polariton in InGaN microcavities at room temperature," *Phys. Rev. Lett.*, vol. 92, pp. 256402, 2004.

[117] K.-G. Gan and J. E. Bowers, "Measurement of gain, group index, group velocity dispersion, and linewidth enhancement factor of an InGaN multiple quantum-well laser diode," *IEEE Photon. Technol. Lett.*, vol. 16, pp. 1256, 2004.

[118] P. G. Eliseev, P. Perlin, J. Lee, and M. Osiński, " "Blue" temperature-induced shift and band-tail emission in InGaN-based light sources," *Appl. Phys. Lett.*, vol. 71, pp. 569, 1997.

[119] J.-C. Lee, Y.-F. Wu, Y.-P. Wang, and T.-E. Nee, "Temperature and current dependences of electroluminescence from InGaN/GaN multiple quantum wells," *J. Cryst. Growth*, vol. 310, pp. 5143, 2008.

[120] S. F. Chichibu, T. Azuhata, T. Sota, T. Mukai, and S. Nakamura, "Localized quantum well excitons in InGaN single-quantum-well amber light-emitting diodes," *J. Appl. Phys.*, vol. 88, pp. 5153, 2000.

[121] Y. Narukawa, Y. Kawakami, S. Fujita, and S. Nakamura, "Dimensionality of excitons in laser-diode structures composed of $In_xGa_{1-x}N$ multiple quantum wells," *Phys. Rev. B*, vol. 59, pp. 10283, 1999.

[122] R. Houdré, R. P. Stanley, and M. Ilegems, "Vacuum-field Rabi splitting in the presence of inhomogeneous broadening: Resolution of a homogeneous linewidth in an inhomogeneously broadened system," *Phys. Rev. A*, vol. 53, pp. 2711, 1996.

[123] M. Pophristic, F. H. Long, C. Tran, I. T. Ferguson, and R. F. Karlicek, "Time-resolved photoluminescence measurements of quantum dots in InGaN multiple quantum wells and light-emitting diodes," *J. Appl. Phys.*, vol. 86, pp. 1114, 1999.

Publication List

Journal Papers

1. Shih-Chun Ling, Tien-Chang Lu, Shih-Pang Chang, **Jun-Rong Chen**, Hao-Chung Kuo, and Shing-Chung Wang, "Low efficiency droop in blue-green m-plane InGaN/GaN light emitting diodes", Applied Physics Letter, Vol. 96, pp. 231101 (2010). (SCI)(EI)

2. **J. R. Chen**, T. C. Lu, H. C. Kuo, K. L. Fang, K. F. Huang, C. W. Kuo, C. J. Chang, C. T. Kuo, and S. C. Wang, "Study of InGaN/GaN light-emitting diodes with different last barrier thicknesses", IEEE Photonics Technology Letters, Vol. 22, pp. 860-862 (2010). (SCI)(EI)

3. H.-M. Huang, S.-C. Ling, **J.-R. Chen**, T.-S. Ko, J.-C. Li, T.-C. Lu, H.-C. Kuo, and S.-C. Wang, "Growth and characterization of a-plane $Al_xGa_{1-x}N$ alloys by metalorganic chemical vapor deposition", Journal of Crystal Growth, Vol. 312, pp. 869-873 (2010). (SCI)(EI)

4. **Jun-Rong Chen**, Yung-Chi Wu, Shih-Chun Ling, Tsung-Shine Ko, Tien-Chang Lu, Hao-Chung Kuo, Yen-Kuang Kuo, and Shing-Chung Wang, "Investigation of wavelength-dependent efficiency droop in InGaN light-emitting diodes", Applied Physics B: Lasers and Optics, Vol. 98, pp. 779-789 (2010). (SCI)(EI)

5. C. H. Wang, **J. R. Chen**, C. H. Chiu, H. C. Kuo, Y.-L. Li, T. C. Lu, and S. C. Wang, "Temperature-dependent electroluminescence efficiency in blue InGaN/GaN light-emitting diodes with different well widths", IEEE Photonics Technology Letters, Vol. 22, pp. 236-238 (2010). (SCI)(EI)

6. Shih-Chun Ling, Chu-Li Chao, **Jun-Rong Chen**, Po-Chun Liu, Tsung-Shine Ko, Tien-Chang Lu, Hao-Chung Kuo, and Shing-Chung Wang, "Crystal quality improvement of a-plane GaN using epitaxial lateral overgrowth on nanorods", Journal of Crystal Growth, Vol. 312, pp. 1316-1320 (2010). (SCI)(EI)

7. Shih-Chun Ling, Chu-Li Chao, **Jun-Rong Chen**, Po-Chun Liu, Tsung-Shine Ko, Tien-Chang Lu, Hao-Chung Kuo, Shing-Chung Wang, Shun-Jen Cheng, and Jenq-Dar Tsay, "Nano-rod epitaxial lateral overgrowth of a-plane GaN with low dislocation density", Applied Physics Letter, Vol. 94, pp. 251912 (2009). (SCI)(EI)

8. Shih-Chun Ling, Te-Chung Wang, **Jun-Rong Chen**, Po-Chun Liu, Tsung-Shine Ko, Bao-Yao Chang, Tien-Chang Lu, Hao-Chung Kuo, Shing-Chung Wang, and

Jenq-Dar Tsay, "Characteristics of a-plane green light emitting diode grown on r-plane sapphire", IEEE Photonics Technology Letters, Vol. 21, pp. 1130-1132 (2009). (SCI)(EI)

9. **Jun-Rong Chen**, Yung-Chi Wu, Tien-Chang Lu, Hao-Chung Kuo, Yen-Kuang Kuo, and Shing-Chung Wang, "Numerical study on lateral mode behavior of 660-nm InGaP/AlGaInP multiple-quantum-well laser diodes", Optical Review, Vol. 16, pp. 375-382 (2009). (SCI)(EI)

10. Min-An Tsai, Peichen Yu, **Jun-Rong Chen**, J. K. Huang, C. H. Chiu, H. C. Kuo, T. C. Lu, S. H. Lin, and S. C. Wang, "Improving light output power of the GaN-based vertical-injection light emitting diodes by Mg^+ implanted current blocking layer", IEEE Photonics Technology Letters, Vol. 21, pp. 688-690 (2009). (SCI)(EI)

11. **Jun-Rong Chen**, Tien-Chang Lu, Yung-Chi Wu, Shiang-Chi Lin, Wei-Rein Liu, Wen-Feng Hsieh, Chien-Cheng Kuo, and Cheng-Chung Lee, "Large vacuum Rabi splitting in ZnO-based hybrid microcavities observed at room temperature", Applied Physics Letters, Vol. 94, pp. 061130 (2009). (SCI)(EI)

12. Tien-Chang Lu, **Jun-Rong Chen**, Shih-Wei Chen, Hao-Chung Kuo, Chien-Cheng Kuo, Cheng-Chung Lee, and Shing-Chung Wang, "Development of GaN-based vertical-cavity surface-emitting lasers", IEEE Journal of Selected Topics in Quantum Electronics, Vol. 15, pp. 850 (2009). (SCI)(EI)

13. Shih-Chun Ling, Te-Chung Wang, **Jun-Rong Chen**, Tsung-Shine Ko, Tien-Chang Lu, Hao-Chung Kuo, Shing-Chung Wang, Po-Chun Liu, and Jenq-Dar Tsay, "Performance enhancement of a-plane light-emitting diodes using InGaN/GaN superlattices", Japanese Journal of Applied Physics, Vol. 48, pp. 04C136 (2009). (SCI)(EI)

14. **Jun-Rong Chen**, Shih-Chun Ling, Huei-Min Huang, Po-Yuan Su, Tsung-Shine Ko, Tien-Chang Lu, Hao-Chung Kuo, Yen-Kuang Kuo, and Shing-Chung Wang, "Numerical study on optical properties of InGaN multi-quantum-well laser diodes with polarization-matched AlInGaN barrier layers", Applied Physics B: Lasers and Optics, Vol. 95, pp. 145-153 (2009). (SCI)(EI)

15. T. S. Ko, T. C. Lu, T. C. Wang, **J. R. Chen**, R. C. Gao, M. H. Lo, H. C. Kuo, S. C. Wang, and J. L. Shen, "Optical study of a-plane InGaN/GaN multiple quantum wells with different well widths grown by metal-organic chemical vapor deposition", Journal of Applied Physics, Vol. 104, pp. 093106 (2008). (SCI)(EI)

16. **Jun-Rong Chen**, Shih-Chun Ling, Chin-Tsang Hung, Tsung-Shine Ko, Tien-Chang

Lu, Hao-Chung Kuo, and Shing-Chung Wang, "High-reflectivity ultraviolet AlN/AlGaN distributed Bragg reflectors grown by metalorganic chemical vapor deposition", Journal of Crystal Growth, Vol. 310, pp. 4871-4875 (2008). (SCI)(EI)

17. T. S. Ko, T. C. Wang, H. M. Huang, **J. R. Chen**, H. G. Chen, C. P. Chu, T. C. Lu, H. C. Kuo, and S. C. Wang, "Characteristics of a-plane GaN with the SiN_x insertion layer grown by metalorganic chemical vapor deposition", Journal of Crystal Growth, Vol. 310, pp. 4972-4975 (2008). (SCI)(EI)

18. **Jun-Rong Chen**, Tsung-Shine Ko, Po-Yuan Su, Tien-Chang Lu, Hao-Chung Kuo, Yen-Kuang Kuo, and Shing-Chung Wang, "Numerical study on optimization of active layer structures for GaN/AlGaN multiple-quantum-well laser diodes", IEEE Journal of Lightwave Technology, Vol. 26, pp. 3155-3165 (2008). (SCI)(EI)

19. **Jun-Rong Chen**, Tsung-Shine Ko, Tien-Chang Lu, Yi-An Chang, Hao-Chung Kuo, Yen-Kuang Kuo, Jui-Yen Tsai, Li-Wen Laih, and Shing-Chung Wang, "Fabrication and characterization of temperature insensitive 660-nm resonant-cavity LEDs", IEEE Journal of Lightwave Technology, Vol. 26, pp. 1891-1900 (2008). (SCI)(EI)

20. Peichen Yu, C. H. Chiu, Yuh-Renn Wu, H. H. Yen, **J. R. Chen**, C. C. Kao, Han-Wei Yang, H. C. Kuo, T. C. Lu, W. Y. Yeh, and S. C. Wang, "Strain relaxation induced microphotoluminescence characteristics of a single InGaN-based nanopillar fabricated by focused ion beam milling", Applied Physics Letter, Vol. 93, pp. 081110 (2008). (SCI)(EI)

21. **Jun-Rong Chen**, Chung-Hsien Lee, Tsung-Shine Ko, Yi-An Chang, Tien-Chang Lu, Hao-Chung Kuo, Yen-Kuang Kuo, and Shing-Chung Wang, "Effects of built-in polarization and carrier overflow on InGaN quantum-well lasers with electronic blocking layers", IEEE Journal of Lightwave Technology, Vol. 26, pp. 329-337 (2008). (SCI)(EI)

22. Tsung-Shine Ko, Chia-Pu Chu, **Jun-Rong Chen**, Tien-Chang Lu, Hao-Chung Kuo, and Shing-Chung Wang, "Tunable light emissions from thermally evaporated In_2O_3 nanostructures grown at different growth temperatures", Journal of Crystal Growth, Vol. 310, pp. 2264-2267 (2008). (SCI)(EI)

23. T. S. Ko, C. P. Chu, **J. R. Chen**, Y. A. Chang, T. C. Lu, H. C. Kuo, and S. C. Wang, "Synthesis of In_2O_3 nanocrystal chains and annealing effect on their optical properties", Journal of Vacuum Science & Technology A, Vol. 25, pp. 1038-1041 (2007). (SCI)(EI)

24. Shing-Chung Wang, Tien-Chang Lu, Chih-Chiang Kao, Jong-Tang Chu, Gen-Sheng

Huang, Hao-Chung Kuo, Shih-Wei Chen, Tsung-Ting Kao, **Jun-Rong Chen**, and Li-Fan Lin, "Optically pumped GaN-based vertical cavity surface emitting lasers: technology and characteristics", Japanese Journal of Applied Physics, Vol. 46, pp. 5397-5407 (2007). (SCI)(EI)

25. T. S. Ko, T. C. Lu, T. C. Wang, M. H. Lo, **J. R. Chen**, R. C. Gao, H. C. Kuo, and S. C. Wang, "Optical characteristics of *a*-plane InGaN/GaN multiple quantum wells with different well widths", Applied Physics Letter, Vol. 90, pp. 181122 (2007). (SCI)(EI)

26. G. S. Huang, H.-G. Chen, **J.-R. Chen**, T. C. Lu, H. C. Kuo, and S. C. Wang, "Hybrid nitride microcavity using crack-free highly reflective AlN/GaN and Ta2O5/SiO2 distributed Bragg mirrors", Physica Status Solidi (a), Vol. 204, Issue 6, pp. 1977-1981 (2007). (SCI) (EI)

27. Yen-Kuang Kuo, **Jun-Rong Chen**, Mei-Ling Chen, and Bo-Ting Liou, February 2007, "Numerical study on strained InGaAsP/InGaP quantum wells for 850-nm vertical-cavity surface-emitting lasers", Applied Physics B: Lasers and Optics, Vol. 86, Issue 4, pp. 623-631 (2007). (SCI) (EI)

28. Yi-An Chang, Tsung-Shine Ko, **Jun-Rong Chen**, Fang-I Lai, Chun-Lung Yu, I-Tsung Wu, Hao-Chung Kuo, Yen-Kuang Kuo, Li-Wen Laih, Li-Horng Laih, Tin-Chang Lu, and Shing-Chung Wang, "The carrier blocking effect on 850 nm InAlGaAs/AlGaAs vertical-cavity surface-emitting lasers", Semiconductor Science and Technology, Vol. 21, pp. 1488-1494 (2006). (SCI) (EI)

29. **Jun-Rong Chen** and Yen-Kuang Kuo, "Optical gain and threshold properties of strained InGaAlAs/AlGaAs quantum wells for 850-nm vertical-cavity surface-emitting lasers", Optics Communications, Vol. 264, pp. 213-218 (2006). (SCI) (EI)

30. Yi-An Chang, **Jun-Rong Chen**, Hao-Chung Kuo, Yen-Kuang Kuo, and Shing-Chung Wang, January 2006, "Theoretical and experimental analysis on InAlGaAs/AlGaAs active region of 850-nm vertical-cavity surface-emitting lasers", Journal of Lightwave Technology, Vol. 24, No. 1, pp. 536-543. (SCI) (EI)

Domestic Journal Papers

1. **陳俊榮**、張誌原、郭艷光、盧廷昌、郭浩中、王興宗，"高亮度氮化鎵發光二極體：高驅動電流下的屏障"，電子月刊，第 16 卷，第 6 期，第 118 至 129 頁，2010 年 6 月.

2. 柯宗憲、王德忠、**陳俊榮**、郭浩中、盧廷昌，2007 年 3 月，"三五族氮化物半導

體有機金屬氣相沉積磊晶技術(MOCVD)之發展與未來, 第 160 至 172 頁.

3. 陳秀芬、蔡孟倫、屠嫚琳、**陳俊榮**、郭艷光、劉柏挺, 2003 年 8 月, "短程光纖通信用紅光面射型雷射的設計與分析", 台灣光通訊產業聯盟 2003 年光通訊特刊, 第 66 至 76 頁.

International Conference

1. **<u>Jun-Rong Chen</u>**, Shih-Chun Ling, Huei-Min Huang, Shiang-Chi Lin, Tsung-Shine Ko, Tien-Chang Lu, Hao-Chung Kuo, and Shing-Chung Wang, Auguest 2009, "High-reflectivity blue-violet AlN/GaN distributed Bragg reflectors grown by metalorganic chemical vapor deposition", The 17th American Conference on Crystal Growth and Epitaxy (ACCGE 2009) in Lake Geneva, Wisconsin USA.

2. **<u>Jun-Rong Chen</u>,** Tien-Chang Lu, Yung-Chi Wu, Shiang-Chi Lin, Wei-Rein Liu, Wen-Feng Hsieh, Chien-Cheng Kuo, Cheng-Chung Lee, Hao-Chung Kuo, and Shing-Chung Wang, June 2009, "Large vacuum Rabi splitting in ZnO-based microcavities", Conference on Lasers and Electro-Optics 2009 (CLEO/QELS 2009) in Maltimore, Maryland USA.

3. **<u>Jun-Rong Chen</u>**, Tien-Chang Lu, Hao-Chung Kuo, and Shing-Chung Wang, April 2009, "Investigation of composition-dependent optical phonon modes in AlxGa1-xN epitaxial layers grown on sapphire substrates", Materials Research Society 2009 (MRS 2009) in San Francisco, CA, USA.

4. **<u>Jun-Rong Chen</u>**, Tsung-Shine Ko, Po-Yuan Su, Tien-Chang Lu, Hao-Chung Kuo, Yen-Kuang Kuo and Shing-Chung Wang, January 2009, "Numerical study on optimization of InGaN multi-quantum-well laser diodes with polarization-matched AlInGaN barrier layers", Proceedings of SPIE, be held in San Francisco, CA, USA. (EI)

5. **<u>Jun-Rong Chen</u>**, Shih-Chun Ling, Huei-Min huang, Tsung-Shine Ko, Tien-Chang Lu, Hao-Chung Kuo, and Shing-Chung Wang, July 2008, "Ultraviolet distributed Bragg reflectors based on AlGaN/AlN multilayers grown by metalorganic chemical vapor deposition," 2008 International Conference on Solid State Devices and Materials (SSDM 2008), be held in Ibaraki, Japan on September 23-26, 2008.

6. **<u>Jun-Rong Chen</u>**, Chia-Ming Chang, Wei-Rein Liu, Chien-Cheng Kuo, Tien-Chang Lu, Tsung-Shine Ko, Wen-Feng Hsieh, Hao-Chung Kuo, Cheng-Chung Lee, and Shing-Chung Wang, July 2008, "Strong exciton-photon coupling at room temperature in ZnO-based hybrid microcavities," 14th Microoptics Conference (MOC'08), be held in Brussels, Belgium on September 25 - 27, 2008.

7. **Jun-Rong Chen**, Yung-Chi Wu, Tsung-Shine Ko, Tien-Chang Lu, Yen-Kuang Kuo, Hao-Chung Kuo, and Shing-Chung Wang, June 2008, "Theoretical analysis on lateral mode behavior of high-power 660-nm InGaP-AlGaInP laser diodes," 6th International Conference on Optics Design and Fabrication (ODF'08).

8. **Jun-Rong Chen**, Shih-Chun Ling, Tsung-Shine Ko, Tien-Chang Lu, Hao-Chung Kuo, and Shing-Chung Wang, February 2008, "High-reflectivity ultraviolet AlN/AlGaN distributed Bragg reflectors grown by metalorganic chemical vapor deposition," 14th International Conference on Metal Organic Vapor Phase Epitaxy (ICMOVPE-XIV).

9. **Jun-Rong Chen**, Tien-Chang Lu, Hao-Chung Kuo, and Shing-Chung Wang, February 2008, "Composition dependence of infrared optical phonon modes in AlGaN epilayers grown on sapphire substrates", Conference on Lasers and Electro-Optics 2008 (CLEO/QELS 2008) in San Jose, California.

10. **Jun-Rong Chen**, Tien-Chang Lu, Gen-Sheng Huang, Tsung-Shine Ko, Hao-Chung Kuo, and Shing-Chung Wang, August 2007, "Infrared reflectance of optical phonon modes in AlGaN epitaxial layers grown on sapphire substrates", Proceedings of SPIE, Vol. 6894 (Gallium Nitride Materials and Devices III), pp. 68941U-1 - 68941U-9. (EI)

11. **Jun-Rong Chen**, Yi-An Chang, Hao-Chung Kuo, Tien-Chang Lu, Yen-Kuang Kuo, and Shing-Chung Wang, May 2007, "Theoretical and experimental analysis of temperature-insensitive 655-nm resonant-cavity LEDs", Conference on Lasers and Electro-Optics/ Pacific Rim 2007 (CLEO/PR 2007)

12. **J. R. Chen**, G. S. Huang, M. H. Lo, T. S. Ko, T. C. Lu, H. C. Kuo, and S. C. Wang, "High-reflectivity ultraviolet AlN/AlGaN distributed Bragg reflectors grown by metalorganic chemical vapor deposition", The 4th International Conference on Materials for Advanced Technologies, be held at the Singapore International Convention & Exhibition Centre July 1 – 6, Singapore, 2007.

13. T. S. Ko, T. C. Wang, **J. R. Chen**, M. H. Lo, C. P. Chu, G. S. Huang, T. C. Lu, H. C. Kuo, S. C. Wang, "Defects reduction and luminescence improvement of a-plane GaN by inserting SiNx nanomasks", The 15th International Conference on Crystal Growth, be held August 12 - 17, Salt Lake City, 2007.

14. T. S. Ko, T. C. Wang, **J. R. Chen**, M. H. Lo, G. S. Huang, T. C. Lu, H. C. Kuo, S. C. Wang, "The effects of H2/NH3 gas flow during growth process on the morphology and hole concentration of a-plane p-type GaN", The 15th International Conference on Crystal Growth, be held August 12 - 17, Salt Lake City, 2007.

15. Shu-Hsuan Chang, **Jun-Rong Chen**, Chung-Hsien Lee, and Cheng-Hong Yang, October 2006, "Effects of built-in polarization and carrier overflow on InGaN quantum-well lasers with AlGaN or InAlGaN electronic blocking layers", Proceedings of SPIE, Vol. 6368 (Optoelectronic Devices: Physics, Fabrication, and Application III), pp. 636813-1 - 636813-10. (EI)

16. Yen-Kuang Kuo, Sheng-Horng Yen, and **Jun-Rong Chen**, October 2006, "Numerical simulation of InAlGaN ultraviolet light-emitting diodes", Proceedings of SPIE, Vol. 6368 (Optoelectronic Devices: Physics, Fabrication, and Application III), pp. 636812-1 - 636812-10. (EI)

17. Yen-Kuang Kuo, **Jun-Rong Chen**, Ming-Yung Jow, Cheng-Zu Wu, Bao-Jen Pong, and Chii-Chang Chen, February 2006, "Optimization of oxide-confinement and active layers for high-speed 850-nm VCSELs", Proceedings of SPIE, Vol. 6132 (Vertical-Cavity Surface-Emitting Lasers X), pp. 175-185. (EI)

18. Shu-Hsuan Chang, Yung-Cheng Chang, Cheng-Hong Yang, **Jun-Rong Chen**, and Yen-Kuang Kuo, February 2006, "Numerical simulation of optical and electronic properties for multilayer organic light-emitting diodes and its application in engineering education", Proceedings of SPIE, Vol. 6134 (Light-Emitting Diodes: Research, Manufacturing, and Applications X), pp. 187-196. (EI)

19. Yi-An Chang, C.-C. Kao, Hao-Chung Kuo, J.-T. Chu, **Jun-Rong Chen**, Sheng-Horng Yen, C.-L. Yu, I. T. Wu, F. I. Lai, Tin-Chang Lu, Yen-Kuang Kuo, and Shing-Chung Wang, May 2006, "Growth and fabrication of p-side-down InGaAs:Sb/GaAs vertical-cavity surface-emitting lasers," 13th International Conference on Metal Organic Vapor Phase Epitaxy (ICMOVPE-XIII).

Domestic Conference

1. **Jun-Rong Chen,** Tien-Chang Lu, Yung-Chi Wu, Shiang-Chi Lin, Wei-Rein Liu, Wen-Feng Hsieh, Chien-Cheng Kuo, Cheng-Chung Lee, Hao-Chung Kuo, and Shing-Chung Wang, 2009, "Large vacuum Rabi-splitting in ZnO-based hybrid microcavities observed at room temperature", 2009 年中華民國物理年會.

2. **Jun-Rong Chen**, Tien-Chang Lu, Hao-Chung Kuo, and Shing-Chung Wang, 2008, "High-reflectivity ultraviolet AlN/AlGaN distributed Bragg reflectors grown by metalorganic chemical vapor deposition", 2008 年台灣光電科技研討會, OPT' 2008 Proceedings.

3. **Jun-Rong Chen**, Yung-Chi Wu, Tien-Chang Lu, Yen-Kuang Kuo, Hao-Chung Kuo, and Shing-Chung Wang, 2007, "Numerical study on lateral mode behavior of

660-nm AlGaInP laser diodes", 2007 年台灣光電科技研討會, paper AP-085, OPT'2007 Proceedings.

4. P. Y. Su, **J. R. Chen**, T. C. Lu, H. C. Kuo, and S. C. Wang, 2007, "Numerical study on optimization of active layer structures for GaN/AlGaN multiple-quantum-well laser diodes", 2007 年台灣光電科技研討會, paper AO-058, OPT'2007 Proceedings.

5. Y. T. Lee, T. S. Ko, T. C. Wang, R. C. Gao, **J. R. Chen**, T. C. Lu, H. C. Kuo, S. C. Wang, 2007, "Optical characteristics of a-plane InGaN/GaN multiple quantum wells with different well widths", 2007 年台灣光電科技研討會, paper AO-013, OPT'2007 Proceedings.

6. G. S. Huang, H. G. Chen, **J. R. Chen**, T. C. Lu, H. C. Kuo, and S. C. Wang, 2006, "Hybrid nitride microcavity using crack-free highly reflective AlN/GaN and Ta_2O_5/SiO_2 distributed Bragg mirrors", 2006 年台灣光電科技研討會, paper AP-032, OPT'2006 Proceedings.

7. R. C. Gao, T. S. Ko, T. C. Wang, M. H. Lo, **J. R. Chen**, T. C. Lu, H. C. Kuo, and S. C. Wang, 2006, "The optical characteristics of different well width from nonpolar $In_xGa_{1-x}N$ multiple quantum wells", 2006 年台灣光電科技研討會, paper AO-36, OPT'2006 Proceedings.

8. **J. R. Chen**, H. H. Yao, H. G. Chen, G. S. Huang, T. C. Lu, H.C. Kuo, and S. C. Wang, 2006, "Suppression of crack generation in asymmetric AlN/GaN distributed bragg reflectors grown by metal organic chemical vapor deposition", 2006 年台灣光電科技研討會, paper AO-26, OPT'2006 Proceedings.

9. Chung-Hsien Lee, **Jun-Rong Chen**, Yen-Kuang Kuo, Shu-Hsuan Chang, and Bo-Ting Liou, 2006, "Influence of built-in polarization on electronic blocking layers for InGaN quantum-well lasers", 2006 年台灣光電科技研討會, paper 129, OPT'2006 Proceedings.

10. **Jun-Rong Chen**, Chung-Hsien Lee, Chien-Fang Chiu, Yen-Kuang Kuo, Bo-Ting Liou, 2005, "Starined InGaAlAs/AlGaAs active layers for 850-nm VCSELs", 2005 年台灣光電科技研討會, paper PA-FR1-073, OPT'2005 Proceedings.

11. **Jun-Rong Chen**, Jyh-Lih Wu, and Yen-Kuang Kuo, 2005, "Effect of doped GaN barrier layer on the optical and transport properties of InGaN/GaN multiple quantum-well light-emitting diodes", 2005 年中華民國物理年會, paper PD-15.

12. 張永政、楊政鴻、**陳俊榮**、郭艷光、劉柏挺、王禹文, 2004, "ITO/TPD/Alq₃/Al 有機發光二極體之模擬與特性探討", 2004 年台灣光電科技研討會, paper

A-SU-II 8-4, OPT'04 Proceedings.

13. 吳志力、<u>陳俊榮</u>、郭艷光、劉柏挺, 2004, "自動脈衝式 780-nm 砷化鋁鎵雷射特性之模擬與分析", 2004 年台灣光電科技研討會, paper A-SA-II 2-5, OPT'04 Proceedings.

14. <u>陳俊榮</u>、屠嫚琳、朱漢義、郭艷光、劉柏挺, 2003, "應力與氧化層結構對磷化鋁鎵銦 650 nm 面射型雷射的影響", 2003 年台灣光電科技研討會, paper PA2-17, OPT'03 Proceedings III, pp. 110-112.

15. 楊勝州、張詒安、顏勝宏、黃詩瑋、蔡孟倫、劉冠良、<u>陳俊榮</u>、林漢威、何依萍、郭艷光, 2002, "紫光氮化銦鎵面射型半導體雷射之設計與分析", 2002 年台灣光電科技研討會, paper PA-33, OPT'02 Proceedings III, pp. 97-99.